Retrospective Theses and Dissertations

Iowa State University Capstones, Theses and Dissertations

2000

Growth and characterization of crystalline Ge[subscript 1-x] C[subscript x] thin films and devices

Jason Thomas Herrold
Iowa State University

Follow this and additional works at: https://lib.dr.iastate.edu/rtd

Part of the Electrical and Electronics Commons, and the Materials Science and Engineering Commons

INFORMATION TO USERS

This manuscript has been reproduced from the microfilm master. UMI films the text directly from the original or copy submitted. Thus, some thesis and dissertation copies are in typewriter face, while others may be from any type of computer printer.

The quality of this reproduction is dependent upon the quality of the copy submitted. Broken or indistinct print, colored or poor quality illustrations and photographs, print bleedthrough, substandard margins, and improper alignment can adversely affect reproduction.

In the unlikely event that the author did not send UMI a complete manuscript and there are missing pages, these will be noted. Also, if unauthorized copyright material had to be removed, a note will indicate the deletion.

Oversize materials (e.g., maps, drawings, charts) are reproduced by sectioning the original, beginning at the upper left-hand corner and continuing from left to right in equal sections with small overlaps.

Photographs included in the original manuscript have been reproduced xerographically in this copy. Higher quality 6" x 9" black and white photographic prints are available for any photographs or illustrations appearing in this copy for an additional charge. Contact UMI directly to order.

UMI®

Growth and characterization of crystalline Ge$_{1-x}$C$_x$

thin films and devices

by

Jason Thomas Herrold

A dissertation submitted to the graduate faculty

in partial fulfillment of the requirements for the degree of

DOCTOR OF PHILOSOPHY

Major: Electrical Engineering (Microelectronics)

Major Professor: Vikram L. Dalal

Iowa State University

Ames, Iowa

2000

UMI Number: 9977326

UMI®

Graduate College

Iowa State University

This is to certify that the Doctoral dissertation of

Jason Thomas Herrold

has met the dissertation requirements of Iowa State University

Signature was redacted for privacy.

Major Professor

Signature was redacted for privacy.

For the Major Program

Signature was redacted for privacy.

For the Graduate College

For my son. Zachary.
Don't worry son. daddy's going
to get a grown up's job now.

TABLE OF CONTENTS

ACKNOWLEDGMENTS

I would like to first acknowledge the many people who have assisted me in completing this dissertation. First, I would like to thank my major professor, Dr. Vik Dalal, for providing the resources and guidance to complete this project. Secondly, I would like to thank the members of my committee, Dr. Gary Tuttle, Dr. David Lynch, Dr. Howard Shanks, and Dr. William Black, for editing my thesis and for making suggestions about it's content.

There are also several faculty and staff who are not directly associated with the Microelectronics Research Center that provided data, equipment and many interesting discussions relating to the topics in this thesis. Dr. James Anderegg of Ames Lab provided the XPS data and guidance on the analysis of the data. Dr. Scott Schlorholtz of the Materials Analysis Research Laboratory made the XRD equipment available and aided in the analysis of the data. Warren Strazheim, also of the Materials Analysis Research Laboratory, made the SEM equipment available and provided training for using it. Dr. Steve Martin and his graduate student Jeremy Shroten of the Materials Science and Engineering Department provided the Raman equipment and training.

I would also like to thank fellow electrical engineering graduate student Matt deFreese and undergraduate chemical engineering student Julie Falter, for collecting most of the OES data used in this dissertation and for making the OES system available for use.

My research assistantship and the costs of this research were supported by the Electrical Engineering Department, the Institute for Physical Research and Technology and by the Electric Power Reasearch Center / Power Affiliate Research Program.

Finally I would like to thank my wife, Kelly and son, Zachary for providing the motivation to complete this dissertation, graduate, and obtain a real job.

ABSTRACT

Alloys of Group IV elements have been routinely studied because new materials can be developed for microelectronic applications in extreme environments, high frequency applications, high efficiency optoelectronic devices or high power density circuits. One of the greatest practical benefits of these materials is that they can be made to work with established Si fabrication technologies, thus greatly reducing the difficulty in manufacturing devices made from these materials. However, there is a Group IV alloy that has remained virtually unexplored, the crystalline Ge:C system, as Ge and C are insoluble in one another at all temperatures and pressures. However, it has been demonstrated that metastable crystalline $Ge_{1-x}C_x$ thin films can be produced with limited success. These materials are of great interest because they can potentially offer the superior mobility and optical characteristics of Ge as compared to those of Si, while the addition of C can raise the bandgap and reduce the lattice constant of the material to be comparable to those of Si. The work presented here uses ECRPECVD processing to grow crystalline $Ge_{1-x}C_x$ films on Si wafers. The first stage of the work is designed to study the characteristics of the plasma source and how the plasma processing parameters affect the material properties of the resulting films. The basic material, optical and electrical properties of the films were studied to build a knowledge resource on this new material. For comparison and to deepen the understanding of the nature of the alloy, pure Ge films were grown with similar parameters to the $Ge_{1-x}C_x$ alloy films. The films are characterized by UV/VIS/NIR Spectroscopy, Raman spectroscopy, x-ray diffraction, x-ray photoelectron spectroscopy, scanning electron microscopy, four point probe conductivity and Hall mobility measurements. The second stage of the research was to dope the material n and p type and to determine the affect on the electrical properties. The final stage was to use the knowledge obtained from the above work to develop novel multi-layer structures that optimize the desirable material properties and to develop a 'proof of concept' diode in the crystalline $Ge_{1-x}C_x$ material, which was the first microelectronic device fabricated in this material.

CHAPTER 1: INTRODUCTION

1.1 Purpose of Research

1.1.1 Carbon alloy materials

Many research groups have pursued the development of Group IV materials in recent research efforts[1]. The driving forces behind this research are the limitations of pure silicon microelectronics in certain extreme uses, such as in high temperature environments, high radiation exposure environments, high frequency or high switch speed applications, high efficiency photovoltaic devices and high power density applications. Group IV alloys have been shown to be an effective means of developing microelectronics to meet the demands of these applications.[2] In particular, the addition of carbon to Si or Si:Ge alloys has been shown to increase the bandgap, increase the power density capability and reduce the lattice parameter of the resulting material. However, the c-Ge:C system has not yet been studied to great detail. This is owed to the problematic nature of the fabrication of Ge:C alloys, as Ge and C are not soluble under thermal equilibrium at all temperatures and pressures. This is quite unlike the counterpart to the Ge:C system, the Si:C system, which has been used extensively in microelectronic applications.[3] However, several research groups have recently reported success in the fabrication of metastable crystalline germanium carbide thin films.

1.1.2 Germanium carbide materials

Crystalline Ge:C does not form a stable stoichiometric alloy under thermal equilibrium, and hence typical thermal mixing does not produce alloy materials in this system. However, it has recently been shown that metastable thin films of $Ge_{1-x}C_x$ with a crystalline phase can be produced with small concentrations of carbon. This processing is done at relatively low process temperatures, thus trapping the Ge and C atoms in a metastable bond. At low temperatures the Ge and C do not have sufficient diffusional energy to phase separate. The problem with this approach to the problem of preparing Ge:C is that materials deposited at low temperatures usually have an amorphous phase. Producing films with a crystalline phase at low temperatures is difficult, but limited success has been obtained by several research groups. Despite the difficulties in producing crystalline germanium carbide, it is desirable to do so because of the attractive properties of this material.

1.1.3 Microelectronic applications

Developing the Ge:C system for use in microelectronics is desirable for several reasons. The first is that Ge:C is a relatively new material. and hence the system presents the opportunity to do research in a new area. This work is important to both the continued development of Ge:C devices and also to the better understanding of the Si:Ge:C system. which has already found applications in heterojunction devices. Secondly. Ge has a much larger electron mobility than Si and it has one of the largest hole mobility known. This makes microelectronics based in Ge attractive for high switch speed applications. Ge also has attractive optical properties in that the main indirect bandgap is only slightly below a higher direct gap by a few meV. Thus. the absorption properties of Ge are superior to that of Si making Ge desirable for photovoltaic and optoelectronic applications. It is well known. however. that Ge is not well suited to microelectronic fabrication and hence devices based in Ge have not been developed. The addition of C. though. may reduce the larger lattice constant of Ge to a value that is comparable to that of Si. This may make possible the integration of Ge based electronics that are grown and processed with existing Si processing technology. thus circumventing the difficulties of processing Ge. Another problem with pure Ge is that the bandgap is so small that any microelectronics made from this material are highly susceptible to thermal noise. However. adding C may raise the bandgap to a value that is comparable to Si. which again circumvents this problem. The final reason for pursuing Ge in microelectronics is that it has been demonstrated that the addition of C dramatically alters the index of refraction of the resulting material in amorphous films. This suggests that stacked layers of crystalline films with varying C content will also have varying indices of refraction. These types of structures have been proposed for use as multi-layered optoelectronic devices. such as anti-reflection IR windows.

1.2 Germanium Carbide Literature Review

Several research groups have worked on the problem of preparing crystalline germanium carbide thin films on silicon wafers. This section will very briefly outline the methods other research groups have used and the results of those methods. The following literature summaries account for the papers published in the major journals to date.

Published papers that discuss only amorphous germanium carbide are not reviewed here.

1.2.1 Ge:C growth by MBE techniques

Kolodzey[4] and co-workers have used molecular beam epitaxy (MBE) techniques to produce germanium carbide thin films at low growth temperatures on (100) oriented Si wafers. The substrate temperature was 600°C. The growth rates were approximately 0.07 μm/h. These films were grown on a 6 nm thick Ge buffer layer. The authors acknowledged that pure Ge growth on Si would result in islands in the buffer layer and hence in the Ge_xC_{1-x} film. Auger and Rutherford back scattering (RBS) analyzed the carbon content in the film. The Auger measurements showed tetrahedral sp^3 bonds. and the atomic percentages were found from the RBS measurements. A maximum of 3 atomic percent was reported although no mention was made as to whether interstitial C or hydrocarbons were accounted for.

The bandgaps were measured by transmission Fourier transform infrared (FTIR) measurements. The value of the bandgap was defined to be the energy at which the absorption coefficient equaled 30 cm^{-1}. The bandgap value increased with increased C beam intensity up to a maximum of 0.87 eV. suggesting the presence of substitutional C. By modeling the increase in bandgap by C content as will be explained below. C concentrations roughly equal to the RBS measurements were calculated. X-ray diffraction (XRD) measurements indicated the films were oriented to the Si wafer and had a crystalline phase. In addition to Ge peaks. a peak near 31.7° 2$\varnothing$ was observed and attributed to the (002) plane in the Ge:C alloy as only a diamond alloy peak can exist in this region. The lattice constant was determined from this peak and the Ge peak. The lattice constant decreased as the amount of C in the films increased. although it did not decrease as much as would be expected from Vegard's Law calculations. The maximum contraction of the lattice was approximately .0002 Å. This discrepancy was attributed to local distortion of the Ge lattice.

Krishnamurthy[5] and coworkers produced Ge:C films at room temperature. The growth rates were between 0.5 and 2 ML per minute. where 1 monolayer is equal to 14 nm. Film thicknesses were 3 to 20 ML. In situ reflection high energy electron diffraction (RHEED) measurements were done to assess the film crystallinity and these indicated the films had amorphous structure. Depositions were also done at higher temperatures but the growth resulted in islanding. Hence the amorphous films were post annealed between 350°

and 600° C to achieve the crystalline phase. Auger measurements were performed to determine the C content, but the accuracy of the measurements was estimated at only ±10%. For films with C concentrations of 20%, the annealing lead to crystalline Ge islands surrounded by amorphous C, as determined by cross-sectional transmission electron microscopy (XTEM). At high C concentrations, up to 80%, the anneals resulted in an amorphous C layer on top of which grows a polycrystalline Ge film. The formation of islands in the intermediate C concentration films was attributed to C pinning of steps or dislocations, which leads to twinned islands.

The Krishnamurthy group published a second paper[6] where a 20 nm Ge buffer layer was grown on (100) Ge substrates. Germanium carbide films were then grown at 200°C. XTEM and atomic force microscopy (AFM) measurements of the film showed the presence of islands approximately 50 nm in diameter. It was also found that the islands were decorated with C clusters. The onset of islands was made sooner with the increase of C, which was up to 5 atomic percent. XRD measurements showed no peaks from the film, only peaks from the substrate. Raman measurements of these films were made and published in a second paper by Weber[7] et al. A Ge:C vibrational mode was identified at 530 cm^{-1} with a full width at half maximum (FWHM) value of 8 cm^{-1}. It was found that this peak could only be seen with Ge substrates, as Si substrates obscured it with the strong c-Si peak at 520 cm^{-1}. It was also found that some of the C in films formed a-C, which resulted in a broad peak at 1400 cm^{-1}. The authors also used RBS measurements to offer a model that predicts the ratio of the Ge:C peak intensity to the c-Ge peak to be approximately 2.6y, where y is the atomic percent of C in the film.

Osten[8] and coworkers produced Ge$_{1-x}$C$_x$ thin films on (001) Si wafers. For their work they employed Sb mediated growth, as it has been previously shown[9] that the addition of Sb inhibits the formation of islands by lowering the surface diffusion of adatoms. They present a standard model for the growth of Ge and Ge$_{1-x}$C$_x$ films that begins with 2-D layer by layer growth up to a critical thickness of about 11 ML, after which plastic relaxation of the layers or islanding occurs. The cause of this relaxation is to minimize the built-in strain energy.

RHEED measurements were done in situ to determine the onset of relaxation as a function of temperature. In all of the films it was found that islanding was completely

suppressed but plastic relaxation still occurred. For Ge films at 450° C relaxation occurred at 11 ML and at 300° C relaxation occurred at 18 ML. For $Ge_{1-x}C_x$ films. with x ≈ .01 by Vegard's Law estimations of XRD data. the films relaxed at 20 ML at 450° C and at 18 ML for 500° C growth. Thus, the addition of C substantially delayed the onset of relaxation and it was again found that lower temperatures raised the critical thickness. The group also found that the Ge:C films could not be modeled as a Ge film with artificially reduced strain. but it can only be modeled as a new type of material with its own activation energy (Ea) for relaxation. They estimate Ea to be 0.13 eV for these films. The films were also post annealed at 450° C in vacuum. and it was observed that this increased the degree of relaxation in all the films.

1.2.2 Ge:C Growth by CVD

First. several papers that were written in regard to the chemical vapor deposition (CVD) of Ge films will be reviewed here. The first paper. by Hall[10]. discusses the thermal decomposition of GeH_4 which is the source gas used by the plasma reactor in this work. Hall deposited thermal CVD films grown on (111) oriented Si wafers. some of which had 1000 Å of oxide on them. The thickness of the films was found by etching steps in the films with a 35% solution of hydrogen peroxide at 50° C. At 300° C and flow rates of 3 to 30 sccm of pure GeH_4 the growth rate was found to be 70 Å/min on oxidized wafers and 50 Å/min on nonoxidized wafers. At 500° C the growth rate increased to 2600 Å/min on the nonoxidized wafers. Hall also found an increase in surface roughness as the temperature was increased. as was indicated by SEM analysis of the surface of the films.

Palange[11] and co-workers studied the CVD of Ge films on (100) Si wafers by AFM and ellipsometry. The films were deposited from GeH_4 at 600° C. The films were only 4 nm thick. They found that the Ge initially grows with the formation of a large number of small. square based pyramid islands on the order of 0.1 μm^2 in area. As growth proceeds. the islands cluster together forming islands up to 0.5 μm^2 in area. The films would eventually develop a poor morphology with dislocated large islands.

LeGeoues[12] and coworkers did similar work to Palange. but used transmission electron microscopy (TEM) to study the films. These films were studied at a lower temperature of 350° C. They found that at lower temperatures the films were composed of

small islands that entirely covered the surface. Subsequent growth produces a new layer that begins with a few small islands of similar dimensions to the first layer, but these islands were approximately 90% relaxed from the onset of growth, unlike the first layer that was strained. The relaxation is due to internal dislocations in the island. These islands act as nucleation centers for continued growth. The group also studied films grown at higher temperatures and found that islands at these temperatures were more strained, being only 25% relaxed.

The next set of papers discussed the growth of Ge:C films by CVD. Smith and coworkers have used ultra high vacuum CVD in a hot wall reactor using germylmethane precursor gasses[13] to produce germanium carbide films on (100) Si. The first set of samples was produced using CH_3GeH_3 and GeH_4 source gasses and substrate temperatures of 470° C. Growth rates ranged from 4.5 to 7 Å/min depending on the amount of C in the films. The amount of C in the films was quantified to within ±0.5% by RBS measurements, and the distribution of C was characterized by Auger and SIMS measurements. The C content was found to be between 1.5% and 3%. TEM revealed stacking faults and twins at the Si interface, but these defects did not continue through the films. Electron diffraction revealed the films had cubic-diamond structure and a lattice constant that was 0.15 Å smaller than Ge, suggesting the C was substitutional.

The second set of films was produced by the reaction of germane and $HC(GeH_3)_3$. The growth rates of these films were approximately 2 Å/min. These films were found to have stacking faults, but the films were still smooth and crystalline. These films contained 5 atomic percent C, but no measurement of lattice constant was reported.

A second paper[14] was published by this group where germane and several other precursor gasses with the general formula $CH_{4-x}(GeH_3)_x$ where x = 2 - 4. These films were prepared at 520° C. Growth rates were 2 nm/min and the films were only 150 nm thick. RBS measurements revealed 15% C. SEM revealed a novel film structure. Within 40 nm of the interface a layer grew with a lattice constant of Si, although the method of measuring these is not reported, along with the inclusion of twins and stacking faults. The film then formed disconnected rods of nanometer diameter and length of approximately 200 – 250 nm. The growth of these rods is believed to begin at twin defects. Electron energy-loss spectroscopy (EELS) showed that the C concentration in the rods was much higher. The lattice constant of the rods was also much smaller than that of the layer. The authors suggest

that the film grows up to a certain critical thickness and then 3-D high growth rate islanding results in the rod formation. The higher C content is attributed to the preferential growth along the rod axis and the inability of the C to precipitate out of the rod. The small lattice constant was attributed to substitutional C. although the authors noted the fact that the material is not constrained to in plane crystal spacing. Use of different precursors and different temperatures ranging from 450° to 550° C suppressed the rod growth. but produced 60 nm diameter islands. which again grew from defect sites. The C content was found to increase up to 15%. although only C concentrations below 5% resulted in smooth 2-D films.

Gazicki[15] and coworkers produced Ge:C films by rf plasma CVD of tetraethylgermanium. $Ge(C_2H_5)_4$. and Ar. The main focus of the study was to determine how varying the rf power changed the plasma. and how these changes affected the deposited films. The plasma was characterized by optical emission spectroscopy (OES) and mass spectroscopy techniques. At powers lower than 10 W it was found that the source gas was not completely dissociated and entire molecules were deposited in the film growth. Thus. the bonding structure of the film was dominated by the bonding structure of the source gas. FTIR and nuclear magnetic resonance (NMR) determined the bonding structure of the films. A relatively low density. and a conductivity below 10^{-10} S/m characterized the low power films. The films had an amorphous structure. The films displayed a large amount of Ge-O. virtually no Ge-H bonds and virtually no sp^2 C bonds.

In contrast. at rf powers of 80 W. atomic germanium. both atomic and molecular hydrogen. and hydrocarbons characterized the plasma to a greater extent than as was found in the lower power plasmas. In comparison to the low power films. the high power films have a much higher density, and a conductivity of 10^{-4} S/m. The films have a microcrystalline structure. and there is evidence of Ge-H bonds and sp^2 carbon bonds. The Ge-O bonds were also found to disappear. Hydrogen passivation of germanium dangling bonds is suggested by the authors as the reason for these results at high powers. as atomic hydrogen is much more abundant in the plasma source at high powers.

1.2.3 Theoretical calculations of Ge:C bandgap

Omer[16] and Kolodzey have calculated theoretical bandgap energies for a continuum in the $Si_{1-x-y}Ge_xC_y$ system. and as part of the analysis. for the silicon carbide. silicon

germanium and germanium carbide constituents. Their approach uses a linear combination of the atomic orbitals found in the material for varying compositions. This approximation is done by mathematically modeling an unstrained crystal structure. It is important to note that the models did not include strain. as it has been shown[17] that strain reduces the bandgap. In these calculations for $Ge_{1-x}C_x$ alloys it was found that the increase in bandgap was very nonlinear. and instead showed a quadratic behavior. By fitting an approximate linear fit to the initial introduction of C. the L indirect gap was predicted to increase by 29.6 meV per atomic percentage of C. However. the Δ gap only increases by 16.7 meV per atomic percent C. Thus. at approximately 5 atomic percent C. the primary indirect gap at L is predicted to change to an indirect gap at Δ.

1.3 Scope of Project

1.3.1 Research problem statement

In light of the above stated questions and motivations for work with crystalline Ge:C materials. the problem statement for this research is as follows. The processing and properties of crystalline $Ge_{1-x}C_x$ thin films on Si wafers will be investigated. with the final goal being to develop novel structures and devices in this relatively new material. The work can be broadly broken down into three stages. The first stage will be to systematically study the characteristics of the plasma source and how the plasma processing parameters affect the material properties of the resulting films. Initially. for the purpose of comparison. pure Ge films will be grown with similar parameters to that of the $Ge_{1-x}C_x$ alloy films. The second stage of the research is to dope the material n and p type. The maximum doping level and the affect on the electrical properties will be studied. The final stage is to develop novel multi-layer structures that optimize the desirable material properties of Ge:C and Ge films and to develop a 'proof of concept' diode in the crystalline $Ge_{1-x}C_x$ material.

1.3.2 Milestones

In this section the major milestones of the overall research plan will be briefly discussed. This overall summary is intended to give the reader insight into how each of the subtopics relate to the overall plan. The first milestone was to investigate the growth of c-Ge

films on Si wafers. In all of the experiments a factorial experimental design was used. The experimental parameters were substrate temperature, pressure, microwave power, and the flow rate of H_2 gas expressed as a ratio of H_2:GeH_4. The GeH_4 flow was constant. The statistical analysis of this design reveals those variables that significantly alter the measured properties and how to maximize the desired properties. The measured properties include the bandgap, as measured by absorption spectroscopy, the lattice constant, crystal orientation, and grain size estimation, as measured by x-ray diffraction measurements, the film thickness, surface roughness, film texture, and visual defect inspection, as measured by scanning electron microscopy, the crystal order, crystalline phase and an estimate of grain size, as measured by Raman spectroscopy, the electrical conductivity as measured by four point probe and finally the carrier mobility as measured by Hall probe measurements. When germanium carbide films are grown, the atomic percent of substitutional and interstial C as measured by x-ray photoelectron spectroscopy will also be measured.

The next milestone was to use optimized runs from the Ge on Si experiment to generate comparison samples on (111) Ge wafers. A repeat of the above characterization was done on these samples. The only deposition procedure that changed was in the cleaning process. Since H_2O_2 etches Ge, the standard RCA cleaning procedure cannot be used. In a literature search for papers discussing the deposition of materials on Ge wafers it was found that the standard cleaning technique for Ge is to boil the wafer in acetone and methanol, and then to desorb any material from the surface by heating the wafer to 800° C in vacuum. Since these films were grown on a strain free surface, these samples served as a comparison to the films grown on the lattice mismatched Si wafers. Doing this experiment revealed how defects in the Ge on Si films, that arise to relieve the compressive strain between the film and substrate, can be identified in the characterization of the films.

The third milestone was to grow c-Ge:C films on Si wafers. The experimental design was the same as the c-Ge experiment, with the addition of CH_4 flow rate as a variable. A similar statistical analysis and optimization process as above was done for these samples.

The next milestone was to grow optimized $Ge_{1-x}C_x$ samples on Ge wafers. This was again done in a similar manner to the Ge on Ge wafer samples. However, in this case, the defect density should not be reduced, as it is predicted to above. This is because the lattice constant of the Ge:C films should be smaller than that of the Ge wafers, and should be

accordingly expansively strained. This experiment proved that the $Ge_{1-x}C_x$ material has its own unique lattice constant. rather than that of a Ge film with artificially reduced strain. as might be the case in the above Ge:C on Si experiments above.

The fifth milestone of this Ph.D. research was to dope the $Ge_{1-x}C_x$ material both n and p type and to determine the effect on the conductivity and mobility. Optimized samples from the above experiments were used. It is desired to know the maximum level of n and p type doping. the amount of auto doping that occurs as a result of the imperfect vacuum of the deposition chamber. and the effect of doping on the conductivity.

The final milestone of the work was to grow novel layer structures and a 'proof of concept' diode structure. The novel layer structures included growing a $Ge_{1-x}C_x$ buffer layer on top of which Ge films were deposited. The buffer layer should significantly reduce the strain between the Si wafer and the Ge film. A variation of this structure was to grade the Ge:C layer. At the Si/Ge:C interface. the concentration of C was high to lattice match the Si and Ge:C as closely as possible. The C concentration was then continuously lowered to the Ge/Ge:C interface. This would lower the misfit between the Ge:C and Ge. The films for this experiment could then be compared to the Ge films grown on Ge wafers.

Another novel layer structure was to grow several Ge:C layers. with varying high and low C concentrations. If the layers are sufficiently thin. the layers should remain strained and not relax through dislocations. As several layers are deposited the strain between the layers and the substrate will be reduced and the final layer should be able to be grown thicker without relaxation. Thus. the defect density should be lower than the $Ge_{1-x}C_x$ films that were grown directly on the Si wafers. A variation of this structure would be to use alternating layers of Ge and Ge:C initially. followed by a Ge film.

The last experiment of this milestone will be to grow a p/n junction in $Ge_{1-x}C_x$. This diode structure will use the doped layers that were grown in above experiments. A n+ doped Ge:C layer can be grown on a n+ doped Si wafer initially. which will serve as a back contact. The p and n layers can then be deposited to form the junction. Cr and Al can then be deposited on top of the junction to serve as a top contact. The diode structure can be characterized by simple I-V measurements. The diode structure and p/n interface will not be optimized in this experiment. but this structure will serve as a 'proof of concept' device. and will demonstrate that microelectronic devices can be made out of this material.

CHAPTER 2: SAMPLE PREPARATION

2.1 Substrate Cleaning

2.1.1 Ge wafer cleaning

Because Ge is readily etched in H_2O_2[18], the Ge wafers could not be cleaned with typical Si cleaning methods, as these methods use H_2O_2. Instead, the following cleaning methods were used just prior to deposition. The samples were first triple rinsed in deionzied water to remove any large dust particles that may have accumulated on them when they were removed from the clean-room packaging in which they had been shipped. Next, the substrates were boiled in acetone for approximately five minutes to remove any soluble contaminants from the surface. The samples were then boiled in methanol to remove the acetone, as methanol safer for the process vacuum environment as is acetone. The substrates were then removed from the methanol bath, partially dried with dry N_2 and then loaded into the deposition chamber. Once in the chamber the substrates were further cleaned by annealing them at 600° C and by etching the growth surface with a low energy H plasma[19].

2.1.2 Si wafer cleaning

The Si wafers used in this study were cleaned by the standard RCA cleaning method, briefly described in Table 2.1. The first step is used for particle removal from the wafer surface. Next, HF strips the native oxide. The last step grows a thin protective oxide layer on the wafer surface. This oxide layer prevents further oxidation and contamination by hydrocarbons. In addition, a 15 second bath in 50:1 HF, done immediately before loading the substrate in the reactor, strips the protective oxide layer and leaves the surface passivated with hydrogen. This H passivation of the surface prevents any oxidation of the surface for a few minutes until the sample is placed in vacuum. This hydrogen surface is then stripped inside the reactor by a hydrogen plasma, which leaves a bare silicon surface to deposit on.

2.2 ECRPECVD Processing

### 2.2.1 Plasma processing fundamentals

The films and devices were grown using electron cyclotron resonance plasma enhanced chemical vapor deposition (ECRPECVD), which will be abbreviated ECR hereafter. To understand the ECR process, it is important first to briefly review the

fundamentals of plasmas.[20] We will begin with a conceptual model of a typical plasma reactor. As shown in Figure 2.1. we imagine an anode and cathode separated by a volume of gas. In any volume of gas there are a certain number of neutral species. ionized species and free electrons. Placing a voltage between the anode and cathode will cause the electrons to drift toward the anode. The ionized species are generally not accelerated because they have a much larger mass than the electrons. Some electrons will strike the neutral species. and if their energy is high enough. ionize them. This results in the creation of more free electrons. which will also begin to accelerate toward the cathode. causing more collisions. If the applied voltage is greater than a critical voltage. or the breakdown voltage. most of the species in the volume will become ionized. creating a plasma by definition. If the electrons reach the cathode. the process will end. But if instead of a DC voltage we use an insulating cathode with an AC voltage applied. the plasma can be maintained. This is so because during the first half of the cycle. current will flow in one direction through the plasma until the insulator is charged at which point the discharge will be terminated. On the last half of the cycle it will flow in the opposite direction. again until the insulator is charged. If the cycle is short enough. or if the frequency is high enough. there is not sufficient time for the insulator to charge and hence a continuous breakdown is maintained. This effect is observed whenever the frequency is above approximately 1 MHz.

Table 2.1: Si wafer standard cleaning procedure.

SC-1:	15 minutes at 80°C
	100 ml NH_4OH + 100 ml H_2O_2 + 500 ml DI H_2O
HF dip:	15 seconds in 50:1 HF
SC-2:	15 minutes at 80°C
	100 ml HCl + 100 ml H_2O_2 + 600 ml DI H_2O

For this dissertation work an ECR plasma chamber was used. The ECR plasma is simply a variation on the continuous plasma model discussed above. The frequency of the ECR plasma is in the microwave region (2.45 GHz). which allows the EM radiation to be ported into the plasma chamber via wave guides. The ECR process differs from a traditional plasma source in that the plasma is augmented with a magnetic field. Per the Lorentz force. moving electrons in the plasma will execute cyclotron motion around the magnetic field lines[21]. as shown in Figure 2.2.
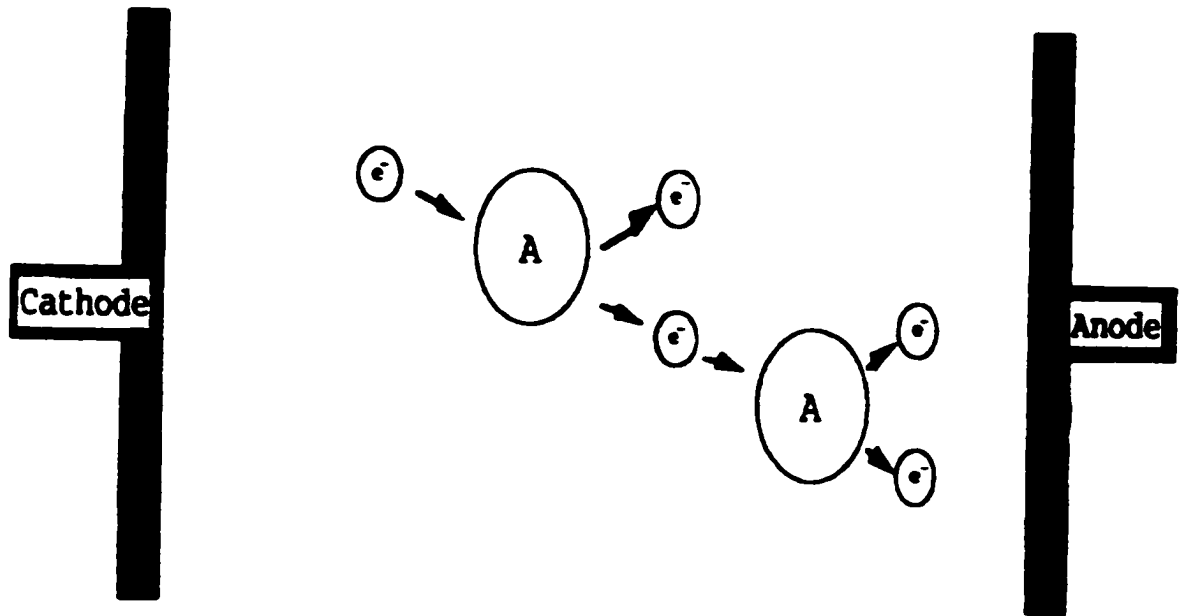
Figure 2.1: Electrical breakdown in plasma gas.
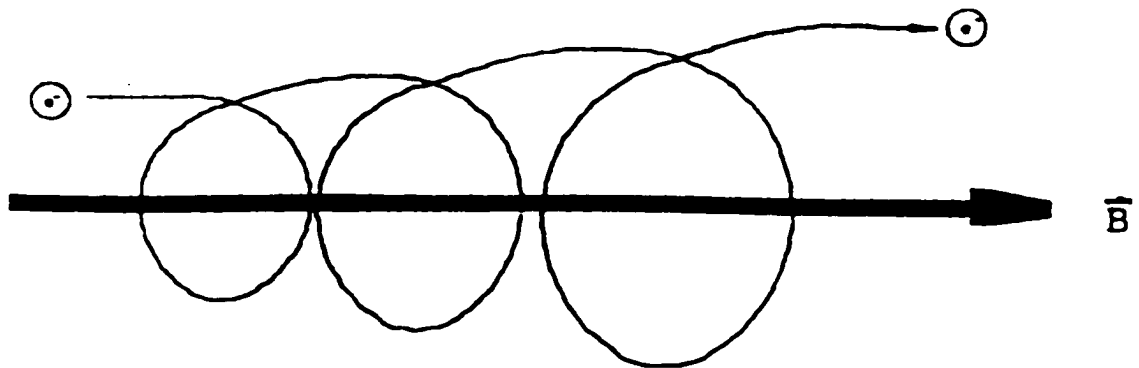
Figure 2.2: Cyclotron motion of electron.

2.2.2 The ECR condition

The cyclotron frequency of the electrons. as derived in the appendix. is given by

$$\omega_o = \frac{qB_o}{m} \qquad (2.1)$$

where B_o is the magnetic field intensity in Tesla. and m is the electron mass. If the cyclotron frequency is matched to the frequency of the incident microwaves then a resonance condition is achieved. This is so because when the microwaves strike the plasma. the elliptically polarized waves are split into a right hand circular wave (RHC) and a left hand circular wave (LHC). As an example. assume that the electrons are rotating in the same direction and at the same frequency as the RHC waves. Then. energy transfer from the microwaves to the electrons becomes quite efficient. The absorption of the LHC is a complex phenomenon to prove. but it is summarized by saying that once the number of species exceeds a critical density. given by

$$N_{cr} = \frac{\omega^2 \varepsilon_o m_e}{q^2} \qquad (2.2)$$

the LHC is also absorbed. ECR plasmas are characterized as having a high density of ionization at low pressures. and highly energetic species are produced. As will become readily apparent. these features of the ECR process are crucial to the growth of the films used in this dissertation.

2.2.3 Growth model

The production of thin films in any plasma CVD reactor depends on collisions between gas phase species. There are several possible outcomes of these collisions. including ionization. excitation. relaxation. dissociation. and recombination. As was discussed above. ionization is crucial to igniting the plasma. Excitation refers to a gas species being raised to an excited energy state. The relaxation process of the species coming out of the excited state may be facilitated by the emission of a photon. The visible photons emitted from the relaxation of the excited species gives rise to the common name associated with this type of reactor. which is a glow discharge reactor. Dissociation is the most important process in PECVD and it will be discussed in more detail below. Recombination is the reversal of dissociation.

The process of dissociation in the ECR plasma source is believed to occur as follows.[22] The first step in the process is the creation of hydrogen ions by an accelerated electron.

$$H_2 + e^- \rightarrow 2H^+ + 2e^- \qquad (2.3)$$
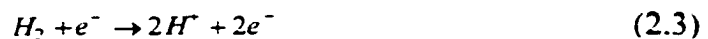
This reaction creates a beam of protons which stream out of the plasma generation area toward the substrate surface. due to the plasma potential with respect to the substrate. The plasma potential for a typical deposition has been measured to be approximately 30 V.[23] The process gasses are introduced in close proximity to the substrate. The reactions for the process gasses are,

$$GeH_4 + H^- \rightarrow GeH_3^* + H_2 \qquad (2.4)$$

$$CH_4 + H^- \rightarrow CH_3^* + H_2 \qquad (2.5)$$

for germane. the germanium source. and methane. the carbon source. respectively. These reactions produce radicals of germane and methane. which will in turn. react with the substrate both physically and chemically. It should be noted that many other gas phase reactions are possible. including pyrolysis. hydrogen reduction. and the formation of different types of radicals. The reactions noted here are the ones that are most productive in quality film production and it is believed that these are the dominant reactions taking place.

At the substrate surface the reactive gas phase species are incorporated onto the surface in one of two ways. First. a reactive species can be physically absorbed at the site of impact. This is not the desired method for incorporating material into the film. for the purposes of this dissertation. but this process does occur during growth none the less. Not all of the impinging atoms will be absorbed: some may be reflected off the surface. or some may only stay on the surface a short time before leaving the surface. The case of physical absorption is schematically described in Figure 2.3. The vertical component of the momentum is absorbed by the substrate as heat. The horizontal component contributes to the surface diffusion energy of the atom. Other factors can influence surface diffusion. including the temperature of the surface. The migrating species may then seek out a nucleation point. A nucleation point is a point on the surface where a group of atoms have condensed to form an island of material. Surface contamination can serve as a condensation point also. As these islands grow. it is possible for one island to coalesce with another. This is the preferred mechanism for growing large grained material. If one island is not able to accommodate another island. two grains will grow.

The second way a reactive species can be absorbed by the film is by a chemical reaction. This is the preferred growth method for crystalline materials. In this process a radical is incident on previously deposited material or it is chemically bonded to the substrate material. A reactive gas species reacts with an active site. as shown in Figure 2.4. where a GeH_3^* radical is schematically incorporated into the Ge lattice. An important mechanism

for the growth of quality crystalline material is surface homogenization by H ions. If the surface shown in Figure 2.4 were not homogenous, that is, if some sites were always active while others were always passive, three dimensional growth or islanding would occur. In the heavily hydrogen diluted ECR plasma, atomic H ions passivate the surface of the film during growth. These sites have a certain probability of becoming active once the H is desorbed from the surface. Since all sites are H terminated, the probability for any site to be active is the same as any other site. Thus, the probability of growth occurring at any point on the surface is the same as any other point on the surface. This process leads to a homogenous growth surface and to a two dimensional film with good crystal quality.
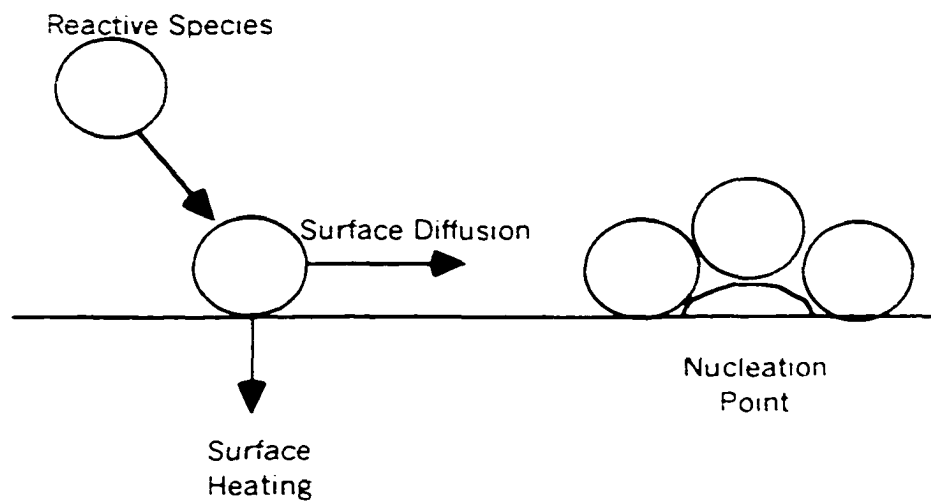

Figure 2.3: Physical absorption on film surface.

The H beam also homogenizes the chemical reactions in the plasma source. This can be understood by reexamining equations 2.4 and 2.5. By breaking the initial process gas molecule into CH_3, the amount of byproduct H_2 that is produced is minimized. Breaking the process gas into any smaller molecules would produce more hydrogen molecules. Producing H_2 in the plasma source is strongly suppressed via Le Chatelier's principle[24], because of the excess H_2 plasma gas that already exists in the source. Limiting the type of radical produced in the plasma source to only one type greatly improves the crystal structure of the resulting film. If this were not the case, if instead several types of radicals tried to chemically insert themselves side by side into the growth surface, voids and other point defects would occur between the dissimilar radicals. But having only one type of radical involved in the deposition process greatly reduces the formation of point defects.

A final way the H beam affects the growth of the film is that it works to etch the

sample surface during growth. H radicals with sufficient kinetic energy can chemically and physically break weak bonds in the crystal lattice of the film upon contact with the substrate. The stronger bonds, those with the correct bond length and bond angle for the diamond crystal lattice, are the only bonds that are left intact. Thus, the non-crystalline material is etched away and all that remains is crystalline material. This reactive etching is very effective in growing crystalline films at low temperatures, as has been demonstrated in growing Si[25] and diamond[26] thin films.
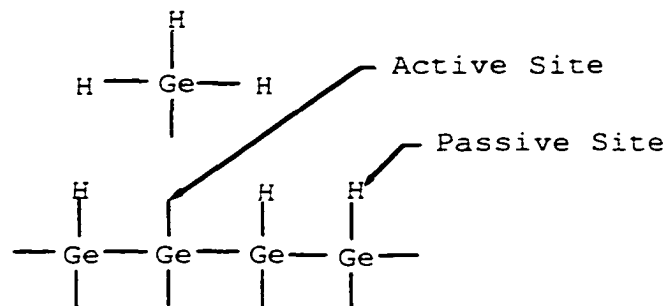
Figure 2.4: Hydrogen homogenization of film surface.

2.2.4 Deposition parameters

One of the advantages of the ECR process is the number of parameters that can be varied. These parameters include source gas selection and dilution, substrate temperature, chamber pressure, microwave power and magnet profile.

The selection of source gasses is the most important parameter and is the starting point for creating a deposition process. For this work common source gasses were chosen, both because of the previous knowledge in working with these gasses and to demonstrate the ability to deposit a unique material from common gasses. Beyond the choice of gasses, the relative dilution of the gases is very important. A heavy dilution of hydrogen is necessary in order to produce the etching and homogenizing effects listed above. As the dilution of methane with respect to germane is changed, the relative number of methane radicals to germane radicals also changes. Thus the C content in the films can be adjusted. However, the dilution of a particular gas also changes the partial pressure of that gas, which can effect the reactive cross section of the gas, leading to unexpected results.

The temperature of the substrate during growth affects the crystallinity of the sample. At higher temperatures, deposited species have sufficient energy to diffuse about the surface

and seek out preferred bonds. This leads to better crystallinity in the films. However in the case of the Ge:C system. lower temperatures are desired. such as to trap the material in a metastable state. This is because the Ge and C will phase separate at high temperatures.

The pressure inside the chamber during deposition has three main effects on the process. First, the pressure alters the plasma chemistry. Secondly, the pressure alters the mean free path of gas phase species in the chamber. At higher pressures. the mean free path is reduced. This results in a lower growth rate because only the radicals produced closer to the substrate than the mean free path distance will contribute to film growth. The same is true for radicals that etch the film. Hence. higher pressures lead to reduced etching in the film as well. The opposite is true for lower deposition pressures. Finally. the energy of ions in the plasma increases as pressure decreases. due to reduced gas phase inelastic collisions. This may change surface reactions and growth rates. In addition. higher energy ions will do more damage to the growth surface. These damage sites can serve as nucleation points and hence. can reduce the grain size of the material.

The power of the microwaves incident on the plasma chamber affects the energy of the gas phase species. Higher powers correlate to higher kinetic energies of the plasma constituents. As the energy increases. the reaction rate for the production of radicals also increases. and there are more gas phase collisions. Hence. the growth rate increases. In addition. the kinetic energy of the etching species also increases. so the rate of etching on the film increases and the damage to the growth surface increases. Lower powers lead to lower kinetic energies. slower growth rates. reduced film etching and reduced plasma damage.

The magnet profile is most critical to the absorption of the microwave energy by the plasma. The intensity of the magnetic field is crucial to obtaining the resonance condition described above. If the profile is not correctly tuned to the input microwave signal. a portion of the power is reflected or the plasma becomes inhomogenous or both. The magnet profile can also be used to move where the resonance point occurs.

2.3 Description of Reactor

A schematic diagram of the reactor is shown in Figure 2.5. As shown. the microwaves are incident though the rear of the reactor. The microwave power source is a Sairem adjustable power source. capable of delivering a continuous microwave up to 300 W and operating at 2.45 GHz. The microwaves are transferred along a coaxial cable to a rectangular wave guide and three stub tuner. The waves pass through a double side polished quartz window to enter the chamber. The magnets consist of copper wire coils. D.C. power

units supply current to the coils and adjusting the current gives the proper magnetic field profile. A restricting orifice achieves directionality of the plasma. An inconel substrate holder supports the substrate and stainless steel masks hold the samples. It is necessary that the substrate holder be made of inconel so that it can withstand heating to high temperatures. Rod heating elements pressure fitted into the sample holder heat the substrate. A Pfeiffer turbo molecular pump evacuates the chamber. A manual gate valve varies system pressure. The plasma gasses are inlet to the rear of the plasma chamber, while the process gasses are inlet in close proximity to the substrate. Unit mass flow controllers control gas flow.
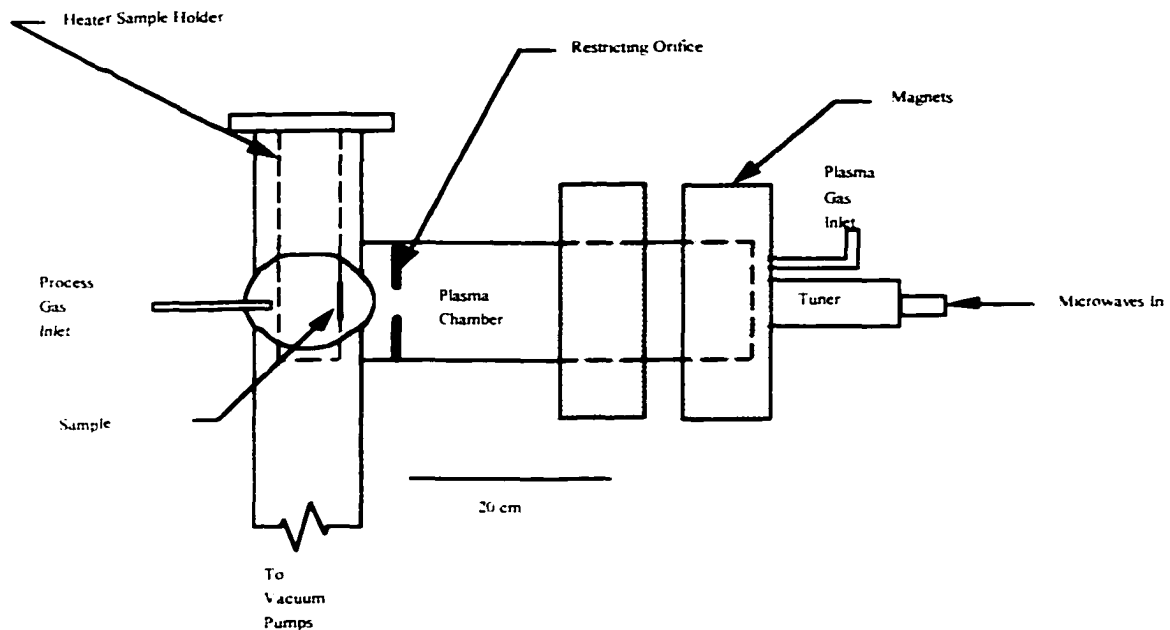
Figure 2.5: Reaction chamber schematic.

CHAPTER 3: CHARACTERIZATION TECHNIQUES

3.1 Plasma Characterization

3.1.1 Past work

The first step in understanding the ECR deposition technique is understanding the plasma source. To facilitate forthcoming discussions of how changing the deposition parameters affects the plasma source. and hence the properties of the resulting films. the work of former Ph.D. student Scott DeBoer. who built the system used in this work as part of his thesis work. will be briefly discussed. Given below for reference are four graphs of common plasma parameters[27] as a function of pressure and power. Figures 3.1 through 3.4. that were generated by DeBoer as part of his research. The two plots of plasma potential show clearly that the potential decreases as pressure increases and as power decreases. This is important information for this work because the higher the plasma potential. the higher the energy of etching species that strike the film. From the plots of electron temperature. we see that electron temperature strictly decreases with pressure. When plotted as a function of microwave power. however. there is a maximum in electron temperature at 100 W for high pressures. and at approximately 150 to 200 W for lower pressures. This is also important for
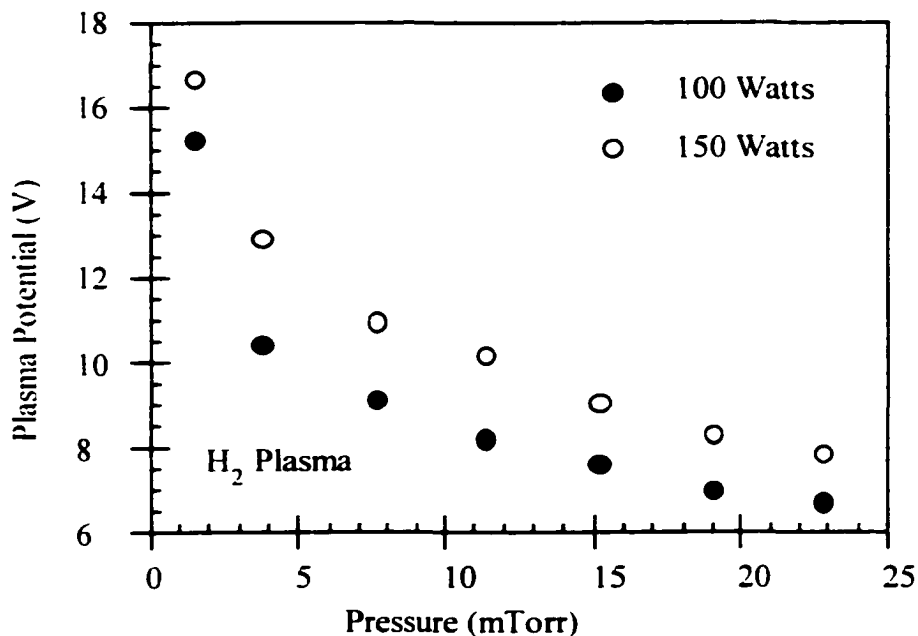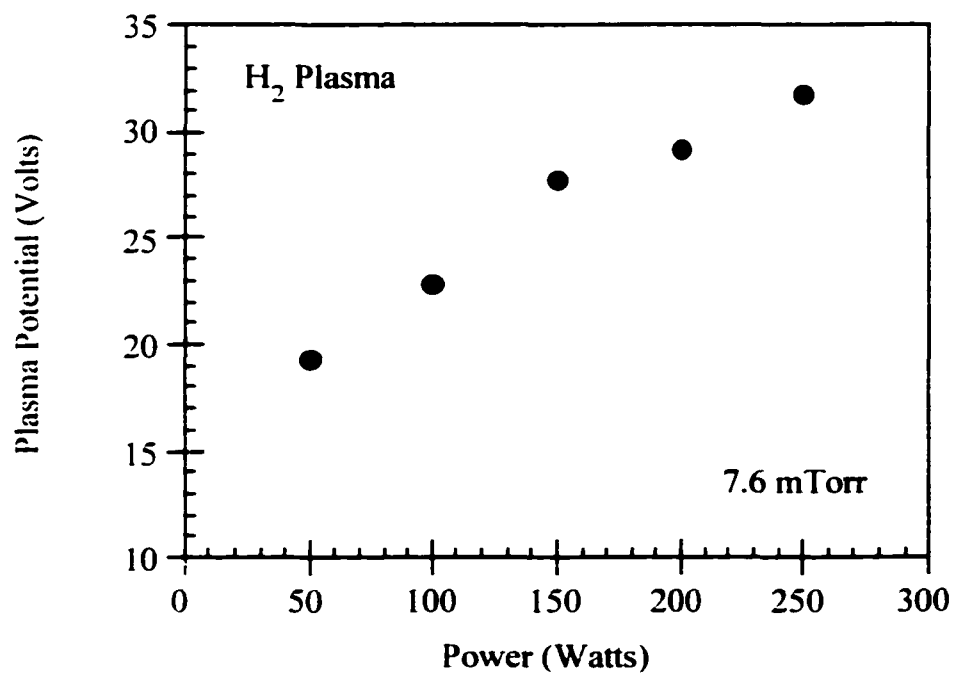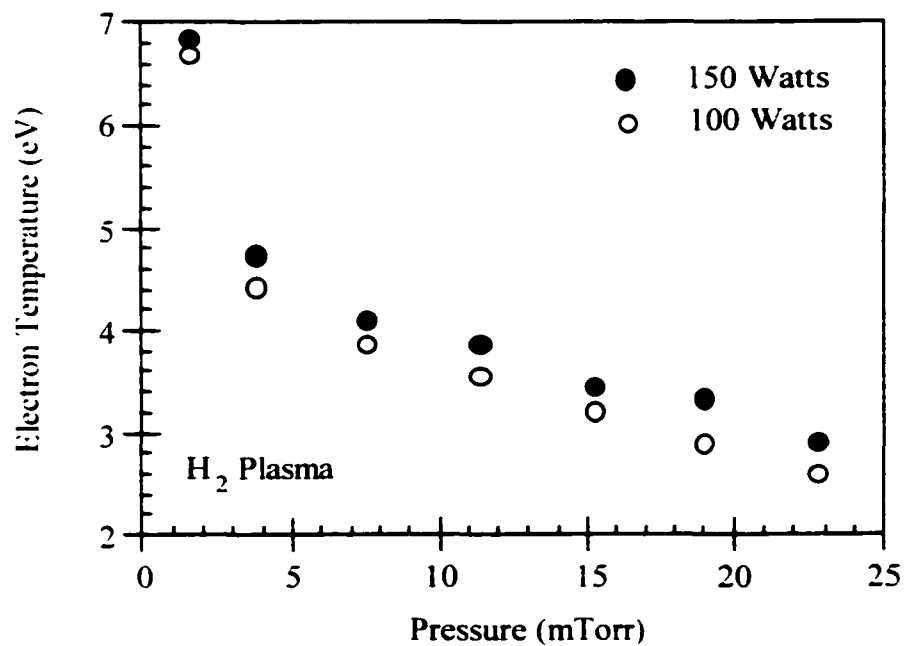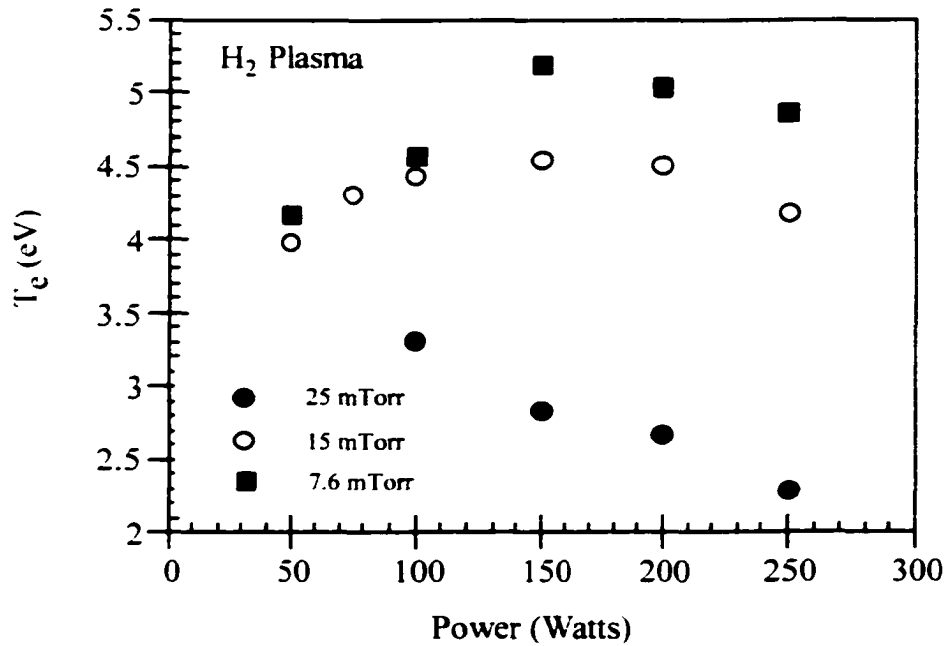

Figure 3.1: Variation of the plasma potential with chamber pressure.[27]

Figure 3.2: Variation of the plasma potential with incident microwave power.[27]

Figure 3.3: Variation of the electron temperature with chamber pressure.[27]

Figure 3.4: Variation of the electron temperature with incident microwave power.[27]

this work, since electron temperature is an indication of reaction rates in the plasma. This information about the plasma characteristics will be used as a guide in developing a fabrication process for this work.

3.1.2 Optical Emission Spectroscopy (OES)

To further characterize the plasma source. OES was used on the ECR system. This work was done in conjunction with the Master's thesis work of Matt DeFreese. which was focused on the characterization of ECR plasmas. OES works by collecting the photons emitted by the plasma source, as was explained in the previous chapter. OES is a method for using this emission spectrum to identify which species are present in the plasma and at what concentrations.[28] This is possible because when an excited species relaxes. it emits photons with only a characteristic wavelength. By separating the wavelengths out of the emission with a monochromator, individual species can be identified. Although it is very difficult to directly quantify the concentrations of species in the plasma, as the intensity at each wavelength is a function of both species concentration and the associated electron impact probability of that species. relative concentrations can be inferred by direct comparisons of the different spectra for different plasma conditions. A commercial OES system and software manufactured by Acton Research Corporation was used for this work.

When analyzing the spectrum from a hydrogen plasma, two peaks are of greatest interest. They are the peaks at 610 nm and 656 nm. The 610 nm peak is the emission line from the diatomic H_2 molecule and the 656 nm peak, denoted as the H_α peak, is from dissociated hydrogen.[29] Looking at the intensities of these peaks gives an idea of how much of the input gas is being broken down by the plasma. As the ratio of the 656 nm to 610 nm peak increases, the degree to which hydrogen is being dissociated increases. It should be stressed again that this is only a semiquantitative measurement, and thus only relative changes between the spectra of plasmas of different system parameters can be compared.

To investigate the properties of germane plasma, helium-germanium plasmas had to be studied in addition to hydrogen-germanium plasmas, because many of the hydrogen and germanium peaks overlapped one another. Three peaks have been identified for this type of plasma. Two are for the Ge atom[30] at 265.2 and 303.5 nm, and one is for the GeH molecule[31] at 246.8 nm.

From the hydrogen-methane plasma spectra, the two most interesting peaks are at 390 nm and 430 nm, which correspond to two different CH transitions.[32] The transitions refer to the level the electron in the CH radical came from. For the purposes of this work, both peaks were taken as an indication of methane radicals being produced.

The OES system was also used to monitor for cross-contamination of dopants when both n and p type materials were being grown. Several peak values were identified[33] for phosphorus and boron are as follows. Peaks for B_2 at 326.9 and 328.5 nm were found and peaks for BH were found at 366.6, 434, and 309.8 nm. Peaks for P_2 at 245.8, 211, 252.1 and 275.5 nm were found. In addition, peaks for PH were found at 339.5, 342.2 and 339.4 nm. Finally, one peak for PH^- was found at 385.1 nm.

3.2 Materials Characterization

3.2.1 Optical

3.2.1.1 UV/VIS/NIR spectroscopy

To determine the absorption coefficient, and thus the bandgap of the material, spectrophotometer studies were performed. The experimental equipment used was a commercial Perkin-Elmer dual beam spectrophotometer. The apparatus generates a beam of monochromatic light and splits it into two separate beams. One beam is used as a reference for comparison to the second beam, which interacts with the sample. A wide range of wavelengths (near-IR, visible, UV) is scanned automatically and an integrated PC records the data.

The absorbance. χ. of a film is defined in terms of the absorption coefficient. α. and the thickness of the film. t,

$$\chi = e^{-\alpha \cdot t} \tag{3.1}$$

The degree to which a particular wavelength of light is absorbed by the material depends on the value of alpha at that wavelength, or in other words. at that particular energy. If alpha can be plotted as a function of energy. then an estimate of the bandgap of the material can be easily determined. as will be shown below. Because the film and the Si wafers are both absorbing. the task of determining alpha as a function of energy can be quite difficult. Amaratunga[34] gives a method for determining alpha for an absorbing film on a semi-absorbing substrate. which is the case for Ge or Ge:C films on a Si wafer. The Amaratunga method is briefly outlined as follows. The technique is based on examining the reflectance spectra from the film only. as any transmission spectra would be attenuated and altered by the absorbing substrate. A typical reflection spectrum is shown in Figure 3.5.
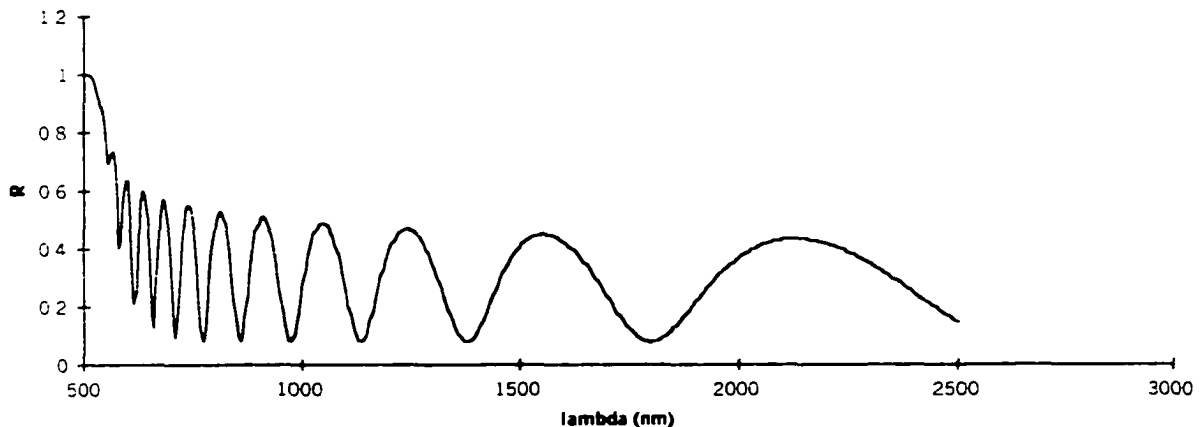
Figure 3.5: Typical reflection spectrum of a thin film.

The reason for the interference pattern in Figure 3.5 is because as the light travels through the sample. reflections will occur from the surface of the film. and the interface of the film and substrate. as shown in Figure 3.6. The interaction in region 2 between the forward traveling and reflected wave will cause constructive or destructive interference effects in the reflected wave in region 1. The first step in the Amaratunga method is to construct smooth envelopes around the constructive and destructive maxima. which will be denoted as R_c and R_d. respectively. The functional form for both curves is a
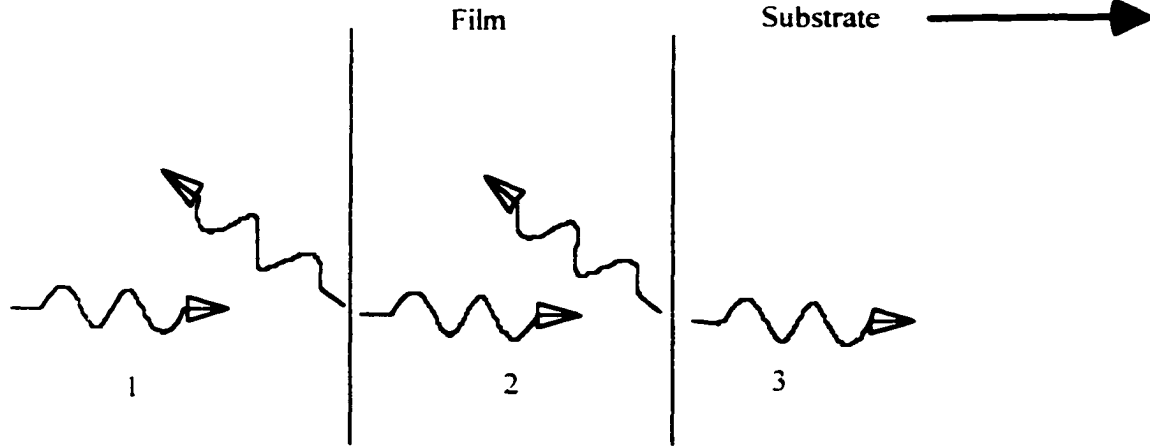
Figure 3.6: Multiple reflections in film.

simple quadratic, which can be easily modeled. Once knowing R_c and R_d, and from a knowledge of the substrate index of refraction, n_s, as a function of wavelength[35], we can solve for the index of refraction of the film, n_f, in the transparent region (approximately 900 nm and higher in Figure 3.5) by.

$$R_c = \frac{(1-n_s)^2}{(1+n_s)^2} \tag{3.2}$$

$$R_f = \frac{(n_f^2 - n_s)^2}{(n_f^2 + n_s)^2} \tag{3.3}$$

and in the weak and medium absorption regions (approximately 900 to 700 nm in Figure 3.5) by.

$$C_1 y^4 + C_2 y^3 + C_3 y^2 + C_4 y + C_5 = 0$$

where.

$$y = \frac{1-n_f}{1+n_f}$$

$$C_1 = (R_c R_d)^f(\pm\sqrt{R_c} - \sqrt{R_d})$$

$$C_2 = R_c + R_d - 2R_c R_d$$

$$C_3 = [(R_c R_d)^f \pm 1](\pm\sqrt{R_c} + \sqrt{R_d}) \tag{3.4}$$

$$C_4 = R_c + R_d - 2$$

$$C_5 = \pm\sqrt{R_c} - \sqrt{R_d}$$

It should be noted that equations 3.3 and 3.4 are for the case where $n_s > n_f$. For the case of $n_s > n_f$ the equation for R_c becomes the equation for R_d and vice-versa. The rest of the analysis

given below holds true when this simple transformation is made. It should also be noted that Equations 3.3 and 3.4 give two unique solutions for n_f. But upon examining plots of n_f as a function of wavelength, it becomes readily apparent that one of the n_f possibilities rapidly converges to 0 in the weak and medium absorption region, leaving only one true value for the index of refraction of the film. In the transparent region, the true curve for n_f can be found by seeing which curve approximately fits curves for known materials, or by comparing the curves to theoretical curves based on the Kramers-Kroning relationship and on known data. Finally, it should be noted that values for n_f can be approximately extrapolated into the strong absorption region from the values of the medium absorption region.

Once n_f has been tediously solved for, we can solve for the absorbance, χ, using either the curve for constructive interference or destructive interference.

$$\chi = \frac{\left(n_f^2 - 1\right)\left(1 - R_c\right) - 4n_f\sqrt{R_c}}{\left(1 - n_f\right)^2 R_c - \left(1 + n_f\right)^2} \frac{n_s + n_f}{n_s - n_f}$$

or,

$$\chi = \frac{-\left(n_f^2 - 1\right)\left(1 - R_d\right) \pm 4n_f\sqrt{R_d}}{\left(1 - n_f\right)^2 R_d - \left(1 + n_f\right)^2} \frac{n_s + n_f}{n_s - n_f}$$

(3.5)

From a knowledge of χ and the film thickness, the absorption coefficient can be easily calculated. Although α is only computed at the points of interference maxims or minima, a smooth curve can be produced by interpolation.

The Armaratunga method has the advantage of being applicable to the case of an absorbing film on an absorbing substrate, but it has the disadvantage of being numerically cumbersome. Swanepoel has proposed a less cumbersome method.[36] The Swanepoel method assumes an absorbing film on a transparent substrate. In general this assumption does not apply to the films grown for this dissertation. However, for Ge films with a bandgap of approximately 0.7 to 0.8 eV grown on Si wafers with a bandgap of approximately 1.2 eV, this technique can be approximately applied. This is so because as the photon energy is increased, the lower bandgap Ge starts to absorb when the larger bandgap Si is still transparent. Unfortunately, this does not work for $Ge_{1-x}C_x$ films that have a bandgap that is similar to that of Si.

The Swanepoel method uses a transmission arrangement, where the photons are incident on the film first, and the amount of radiation exiting the back of the wafer is recorded. This experimental arrangement introduces an additional difficulty in that the wafer is only single-side polished, and hence, the unpolished side scatters the light as it exits. However, if the back of the wafer is placed against the entry window of the integrating

sphere of the Lambda 9 spectrophotometer, then all of the scattered light is collected. The Swanepoel method uses envelopes around the constructive and destructive patterns, similar to the Aramatunga method. The Swanepoel methodology is briefly described as follows. First, the index of refraction of the substrate must be known. This can be found in the literature or from a transmission scan of a bare substrate over the interval of interest. If the substrate is non-dispersive in the interval, then the substrate index of refraction, denoted by s, can be computed from the value of the transmission, denoted Ts, by,

$$s = \frac{1}{T_s} + \left(\frac{1}{T_s^2} - 1 \right)^{1/2} \qquad (3.6)$$

Secondly, continuous curves around the interference maximums, T_M, and the interference minimums, T_m, are constructed. Interpolation techniques must be used to generate a smooth curve between the points. In the absorbing region, the peak values must be adjusted so that the T_M and T_m curves touch at tangential points. An example of how to properly do this is shown in Figure 3.7.
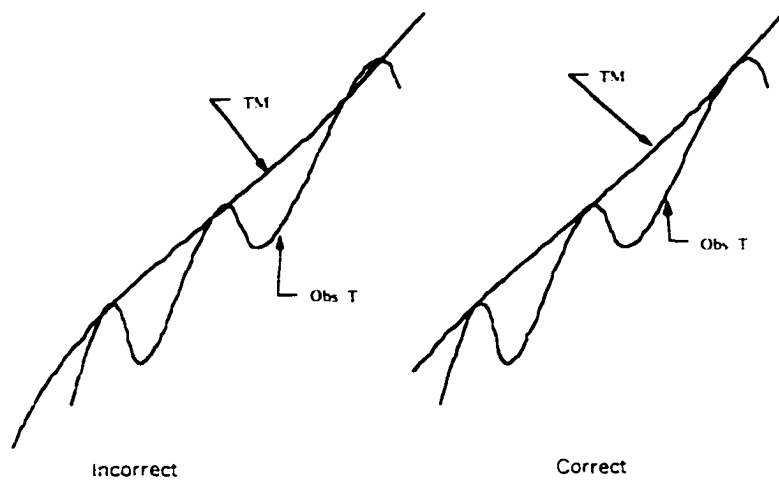
Figure 3.7: Tangential method of constructing interference envelopes.

As a first approximation of the film index of refraction, use the T_M/T_m pair from the above curves for each extreme to calculate n1 from,

$$n = \left[N + \left(N^2 - s^2 \right)^{1/2} \right]^{1/2} \qquad (3.7)$$

where,

$$N = 2s \frac{T_M - T_m}{T_M T_m} + \frac{s^2 + 1}{2} \qquad (3.8)$$

Next, using the values of n1, a straight line plot of $1/2$ vs. n/λ is constructed using the equation.

$$\tfrac{1}{2} = 2d\left(\frac{n}{\lambda}\right) - m_1 \qquad\qquad (3.9)$$

where $l = 0, 1, 2, 3$, etc. and d is the film's thickness. It may be necessary to eliminate the points corresponding to the two smallest λ if they do not fall on the straight line of the other two points. Next. pick the half integer value (1, 1.5, 2, 2.5, etc.) that is closest to the intercept of the above linear equation. This is the true value of m1. or the order of the first interference fringe visible in the spectrum. Half integers correspond to minima. and whole integers correspond to maxims. Use this value of m1 to replot the line. and the slope of that line will be equal to twice the thickness. The value of d obtained from the slope is accurate to within ±0.01 µm. Now assign the order number to each extreme. by adding 0.5 to the next extreme after m1. add 0.5 to the extreme after that. etc. With the order numbers for each extreme. the value of n can be calculated to within 1% by the Bragg diffraction equation.

$$2nd = m\lambda \qquad\qquad (3.10)$$

If a smooth function of n is desired. a parabolic fit (at least for Si and Ge) can be made to the data from.

$$n = \frac{a}{\lambda^2} + \frac{b}{\lambda} + c \qquad\qquad (3.11)$$

The plots of $n(\lambda)$ and T_M are then used to calculate $\chi(\lambda)$ by.

$$\chi = \frac{E_M - \left[E_M^2 - \left(n^2 - 1\right)^3\left(n^2 - s^4\right)\right]^{1/2}}{\left(n-1\right)^3\left(n - s^2\right)} \qquad\qquad (3.12)$$

where.

$$E_M = \frac{8n^2 s}{T_M} + \left(n^2 - 1\right)\left(n^2 - s^2\right) \qquad\qquad (3.13)$$

Finally. using $\chi(\lambda)$ and the thickness, d, $\alpha(\lambda)$ can be calculated from.

$$\alpha = \frac{-\ln(\chi)}{d} \qquad\qquad (3.14)$$

The Swanepoel method contains more experimental steps than the Aramatunga method. but the calculations for the Swanepoel method are straightforward. Hence. the Swanepoel method leads to the absorption coefficient faster. The Swanepoel method is also powerful in that it can estimate a value for surface roughness[37] of the film and correct the T_M and T_m values by.

$$\Delta T_n = \frac{(2\pi)^2}{6} * \frac{C}{A} * T_n\left[\left(\Delta\lambda^2\right) + \lambda_n^2\left(\frac{\Delta d^2}{d^2}\right)\right] \qquad\qquad (3.15)$$

where.

$\Delta T_n \equiv$ amount to add to or subtract from extrema

$C \equiv 2(n^2 - 1)(n^2 - s^2)$

$A \equiv 16n^2s$

$T_n \equiv$ extrema transmiss ion value

$W_n \equiv$ width between n - 1 and n + 1 extrema

$\Delta\lambda \equiv$ slit width

$\lambda_n \equiv$ wavelength of extrema

$\Delta d \equiv$ surface roughness

$d \equiv$ film thickness

$\Delta T_n \equiv$ amount to add to or subtract from extrema

$C \equiv 2(n^2 - 1)(n^2 - s^2)$

$A \equiv 16n^2s$

$T_n \equiv$ extrema transmiss ion value

$W_n \equiv$ width between n - 1 and n + 1 extrema

$\Delta\lambda \equiv$ slit width

$\lambda_n \equiv$ wavelength of extrema

$\Delta d \equiv$ surface roughness

$d \equiv$ film thickness

The estimate for surface roughness can be improved from an initial guess by increasing its value until the values of T_M in the transparent region are equal to T_s. or until the increase in surface roughness makes lower values of T_M larger than T_M at longer wavelengths.

A final method for determining the absorption coefficient is given by Pankove.[38] The Pankove method assumes a transmission spectrum and a transparent substrate. like the Swanepoel method. and is therefore only applicable to certain films in this dissertation. The Pankove method is based on an examination of the attenuation of the light by the film. as shown in Figure 3.8.
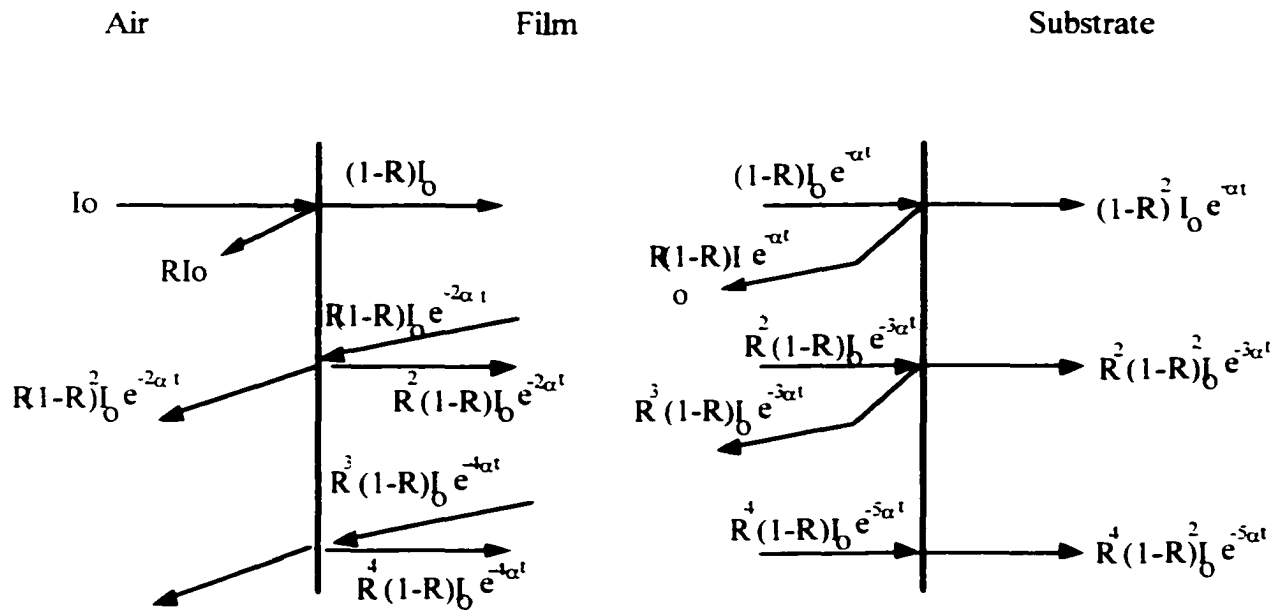
As can be seen. the multiple beams emitted from the film form the series.

$$R^{2(n-1)}(1 - R)^2 I_o e^{-2n-1} \tag{3.16}$$

which can be written.

$$\frac{(1 - R)^2 e^{-\alpha t}}{1 - R^2 e^{-2\alpha}} I_o \tag{3.17}$$

If we then calculate the transmittance T by dividing the above by the incident beam I_o andassume that the quantity αt is large. we are left with.

Air   Film   Substrate

Figure 3.8: Ray tracing in film showing absorption.

$$T \approx (1 - R)^2 e^{-at} \tag{3.18}$$

For convenience we will define absorbance. as $\log_{10}\left(\frac{1}{T}\right)$. Substituting the above equation for T into the absorbance equation and solving for α. the absorption coefficient. yields.

$$\alpha = 2.3\frac{A}{t} - \frac{\ln\left(\frac{1}{1-R_i}\right)}{t} \tag{3.19}$$

By measuring R and T with the spectrophotometer for a given interval of wavelengths. a plot of α vs. λ can be generated.

The Pankove method is by far the simplest method. and a plot of $\alpha(\lambda)$ can be constructed very rapidly. However. there are two drawbacks to this method. The first is that this method does not account for the interference pattern discussed above. and hence the plot of $\alpha(\lambda)$ also contains the interference pattern. Hence. the values of α can be skewed from their true values by a large margin. Constructing quick envelopes around the interference pattern and then taking the geometric mean of the continuous interference envelopes can approximately correct for this problem. This generally gives a smooth $\alpha(\lambda)$ which is approximately correct. The second drawback of the Pankove method is far more serious. This problem concerns the basic formulation used in Figure 3.8. As can be seen. the same reflection coefficient is used for the air/film interface . the film/substrate interface. and the

film/air interface. Obviously, these reflection coefficients are all different, and therefore a basic error exists in this technique. To correct for this problem, separate terms for the reflection coefficient of each interface must be used in the Pankove equations, where the general form of each reflection coefficient is given by

$$R = \frac{(n_1 - n_o)^2 + k_1^2}{(n_1 + n_o)^2 + k_1^2}$$

(3.20)

where the 0 subscript refers to the medium the photon is currently in and the subscript 1 refers to the medium beyond the interface. Using separate reflection coefficient terms in the basic Pankove formalism, we obtain a new summation for the multiple beams emitted from the film.

$$\sum_{t=1}^{x} R_1^{t-1} R_2^{t-1} (1 - R_1)(1 - R_0) I_0 e^{-\alpha(2n-1)t}$$

(3.21)

where R_0 refers to the air/film interface. R_1 refers to the film/substrate interface, and R_2 refers to the film/air interface. It should be noted that terms for the substrate to air interface where also added to this summation, but was found that the effect of these terms was negligible. This summation can then be divided by the original intensity striking the film to obtain the desired form of the equation. However, unlike the Pankove equation, this summation cannot be reduced by a simple series transform. This necessitates computing the sum for each wavelength measured, which is a disadvantage when comparing to the ease at which the original Pankove equation can be computed. However, it was found that computing only five terms of the sum is more than sufficient to obtain good accuracy. (x = 5 in equation 3.21) To check the validity of this new equation, a theoretical film was analyzed. This theoretical film was given in the Swanepoel paper, where it was used to demonstrate that the Swanepoel method determined the optical constants that where used in constructing the theoretical film with great accuracy. For comparison, the original Pankove equation and equation 3.21 where used to analyze the theoretical film. Figure 3.9 shows the resulting simulated transmission curve generated by the Swanepoel method, the Pankove method after the interference pattern was smoothed out as described above and the modified Pankove method where equation 3.21 was used. As can be seen the modified Pankove method matches the Swanepoel method much better than the original Pankove method. The modified Pankove equation therefore matches the correct absorption coefficient of the theoretical film much better than the original Pankove equation.

Once the absorption data were found by appropriate choice of one of the three methods described above, an estimation of the bandgap could be made. In determining the value of the bandgap, two different estimation techniques were used. Both techniques are based on the α spectrum. The first of these estimation techniques is known as the E_{04}
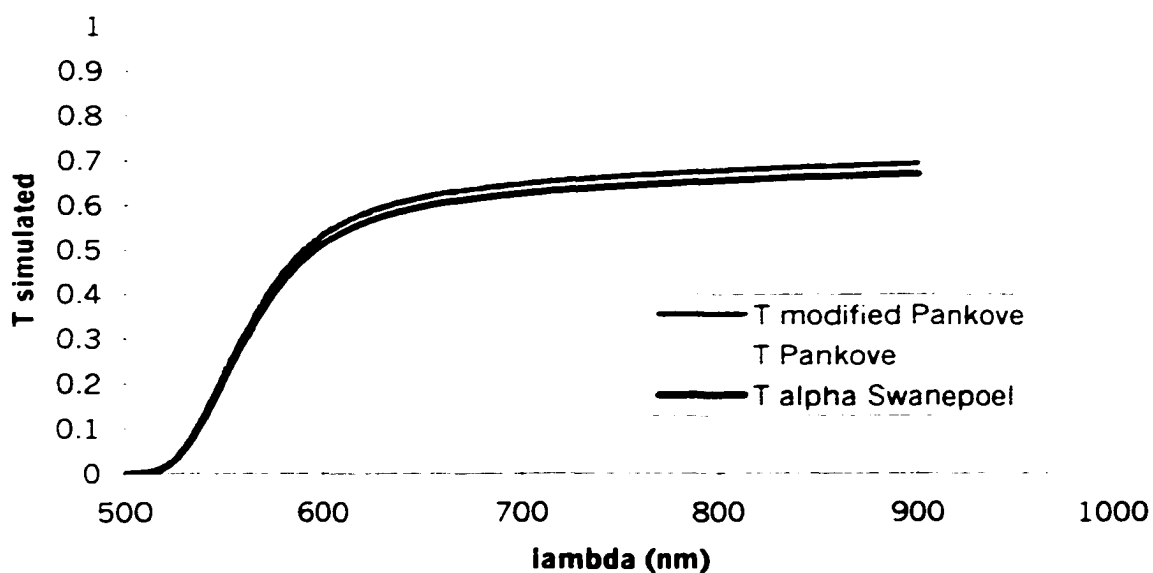
Figure 3.9: **Comparison between the Swanepoel, Pankove and modified Pankove method of simulating the transmission spectra.**

bandgap estimation. The E_{04} bandgap is simply the energy value that corresponds to where α equals 10^4 cm^{-1}. An example of an α vs. energy plot with the E_{04} bandgap equal to 0.87 eV is shown below in Figure 3.10.

The second calculation is known as the Tauc gap estimation. This technique uses a plot of $\sqrt{(\alpha * E_{ph})}$ vs. E_{ph} where E_{ph} is the energy of the incident photons, as shown in
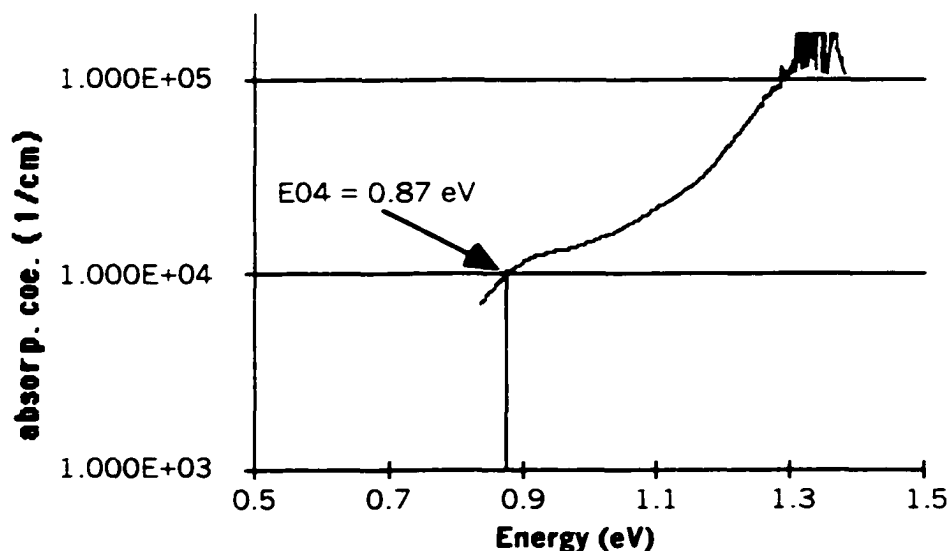
Figure 3.10: α **plot of Ge$_{1-x}$C$_x$ film with E$_{04}$ = 0.87 eV.**

Figure 3.11. The Tauc gap is then determined by extrapolating the linear portion of the plot down to the x axis. Where the extrapolation crosses the x axis is the value of the Tauc gap. Both bandgap estimations were used to compare the various samples produced by this project. Since germanium has a bandgap of 0.7 eV and carbon has a bandgap of 5.4 eV, the bandgap of a Ge:C alloy should have a bandgap greater than 0.7 eV and it should increase with increasing alloyed carbon content. However, an important complication in this idea is that the bandgap of the material will also vary with varying grain size. So when comparing the bandgap of different materials, it is very important to also compare the crystallinity of the two samples.
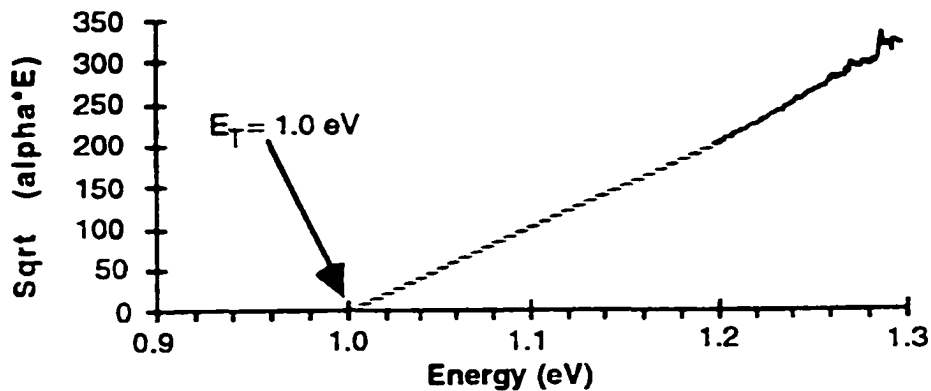

Figure 3.11: Tauc plot of $Ge_{1-x}C_x$ film with $E_T = 1.0$ eV

3.2.1.2 Raman spectroscopy

Raman spectroscopy was extensively used to determine the degree of crystalline quality of the films. The experimental system used was a commercial Bruker instrument, provided by the Materials Science and Engineering department of ISU. Raman scattering is based on the assumption that crystals can be modeled as billiard balls, which represent the atoms, connected by springs, which represent chemical bonds.[39] The vibrational modes of these systems are determined by the mass of the balls, or atomic weights, and the stiffness of the springs, or bond force constants. In real crystals, a Raman measurement uses an intense laser beam to illuminate a sample. The incident wave distorts the electron cloud around the atoms in the crystal. When the wave passes, the stored energy in the distorted cloud is released, mostly at the same frequency of the incident radiation. This is known as Rayleigh scattering. In addition to Rayleigh, Stokes scattering also occurs. Stokes scattering occurs when part of the stored energy is given to the crystal. This energy creates phonons in the

lattice. which subtract energy from the reradiated photons. Anti-Stokes scattering also occurs when the stored energy annihilates a pre-existing phonon. which adds energy to the reradiated beam. The Stokes scattering is the scattering mechanism that produces the useful Raman spectra. and can be mathematically written as.

$$\hbar\omega_s = \hbar\omega_i \pm \hbar\omega_p \qquad (3.22)$$

$$\hbar k_s = \hbar k_i \pm \hbar q_p \qquad (3.23)$$

where the subscript s refers to the scattered photon. i refers to the incident photon. and p refers to the phonon. These equations arise from energy and momentum conservation principles in the crystal. In the above equations the minus sign refers to Stokes scattering and the plus sign refers to an anti-Stokes scattering.

In Raman spectra. the most useful parameter is the position of the observed peaks. Crystalline Ge has only one Raman active phonon mode at 300 cm^{-1} and hence. only one peak at this value.[40] Amorphous Ge can have variety of phonon modes. with peaks centered at 80. 125. 177. 230. 278. 360. 450. 550. 540. 565. 1890 and 1975 cm^{-1}. The frequency relating to the TO band. the 278 cm^{-1} peak. is the most intense and is the peak generally associated with an amorphous sample. In polycrystalline films it is possible to have both crystalline and amorphous phases. Hence. the ratio of intensities of the 300 and 278 cm^{-1} peaks can give an indication of the amount of crystalline and amorphous material. respectively. in the film. A peak for crystalline Ge:C is given in the literature review.

In addition to the wavenumber about which a peak is centered. there are several quantitative parameters that can be measured in the spectrum of a polycrystalline film.[41] The width of the crystalline 300 cm^{-1} peak gives an indication of the crystalline quality of the film. In a single crystal. phonons may be described by a plane wave. whose associated momentum selection rules only allow one frequency in the spectrum. But in a polycrystalline film with finite grain size. a wave packet must describe the phonon with a confinement that is comparable to the size of the grain. The wave packet introduces an uncertainty in the wave vector and therefore an uncertainty in the frequencies of the spectrum. This uncertainty increases as grain size becomes smaller. Peak width will then increase as grain size becomes smaller. Also, if the grain size reduces to a few hundred angstroms. the peak will shift to lower frequencies and become asymmetric with a broad shoulder on the low wavenumber half of the peak. These parameters are schematically shown in Figure 3.12, which shows spectra of a crystalline Si sample and a small grain microcrystalline Si sample.
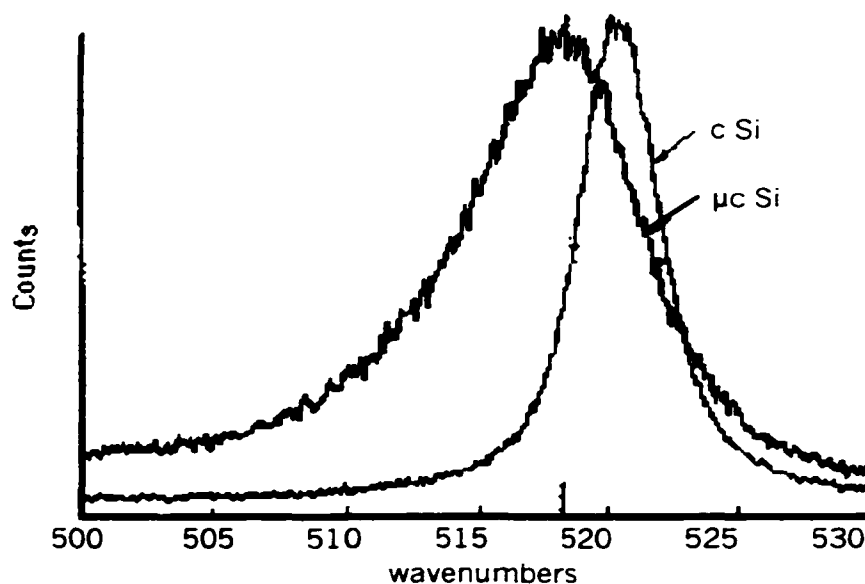
Figure 3.12: Raman spectra of c and µc samples.[41]

3.2.2 Structural and chemical

3.2.2.1 X-Ray Photoelectron Spectroscopy (XPS)

X-Ray photoelectron spectroscopy (XPS) measurements were performed to determine the percentage of alloyed carbon in the films. The measurement apparatus used was a commercial Perkin-Elmer unit supplied by the Materials Chemistry Program of Ames Lab. XPS is based on the interaction of the atoms in a material with incident X-ray radiation.[42] If the energy of the radiation is high enough, it will liberate electrons from the various shells in an ionization process according to the photoelectric law.

$$KE = h\nu - BE \qquad (3.24)$$

where KE is the kinetic energy of the liberated electron. $h\nu$ is the energy of the incident x-ray, and BE is the binding energy of the electron to the nucleus. The XPS technique measures KE. and from a knowledge of hν, calculates BE. The binding energy relates directly to the energy level the electron came from and therefore different electron orbitals of a particular atom can be identified. By this technique all elements except for hydrogen and helium can be identified. The quantity of a particular element in a sample can also be determined if the cross sections of each orbital are known for that element. In a quantitative study, the relative intensities of the peaks for all elements identified are compared. A schematic of the photoelectric process is shown in Figure 3.13, where a 1s electron is raised to the vacuum level by an x-ray.

It is statistically more likely to see electrons from core shells. since they have a larger cross section than the valence electrons. at the wavelength of the x-ray source that was used. The binding energy of these inner core electrons for a given atom is nearly constant. but not exactly constant. Small shifts in peak energy can be   detected if the atom of interest is bonded with other atoms. By comparing these shifts to known chemical compositions. it is possible to distinguish between isolated atoms and chemically bonded atoms. This was of great importance in this study. since the desired product was alloyed Ge:C and not simply Ge with interstitial C atoms as defects. The desired carbide material has a peak at 283 eV.[43] Graphite has a peak at 284 eV and a single carbon atom has a peak at 285 eV.
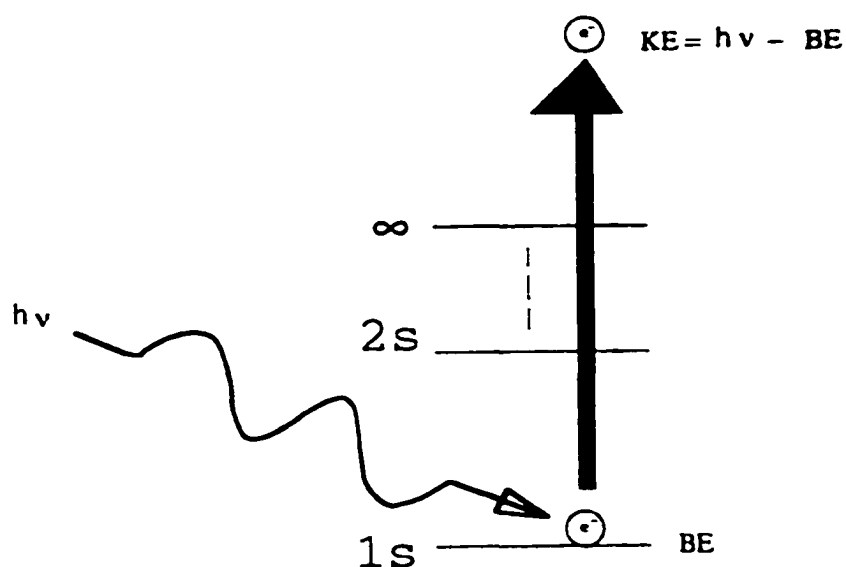
**Figure 3.13: Excitation of an electron to the vacuum level
by an X-Ray.**

XPS was complicated by two factors in this study. The first complication was that since carbon is a light element and it only existed in very small concentrations in the material. the peak intensities for carbon were very small in comparison to the background. Hence. great care had to be taken in finding the intensity of these peaks. Secondly. XPS is primarily a surface technique. since electrons produced more than a few monolayers below the surface will not make it out of the material without incurring inelastic collisions. It was found that the surface of the material was covered with a germanium oxide that contained hydrocarbon and other trace impurities. This layer had a much higher carbon concentration (10 - 20%) and therefore needed to be etched away in vacuum before the true carbon content of the samples could be found. This thin oxide layer was easily etched away by an Ar

plasma, which was generated in the XPS apparatus.

3.2.2.2 X-Ray Diffraction (XRD)

To characterize the crystal structure of the films, x-ray diffraction experiments were performed. The diffractometer used in the experiments is maintained by the Materials Analysis Research Laboratory of ISU. The diffractometer used Bragg-Brentano geometry where both the detector and the x-ray source are swept through angles 2Ø as shown below in Figure 3.14. The basic principal of x-ray diffraction is an application of Bragg's law.[44] Bragg's law states that the interference of reflected x-ray waves from a crystal is at a maximum when the angle of incidence makes the path difference between the reflected waves from two successive lattice planes an integer multiple of the wavelength.
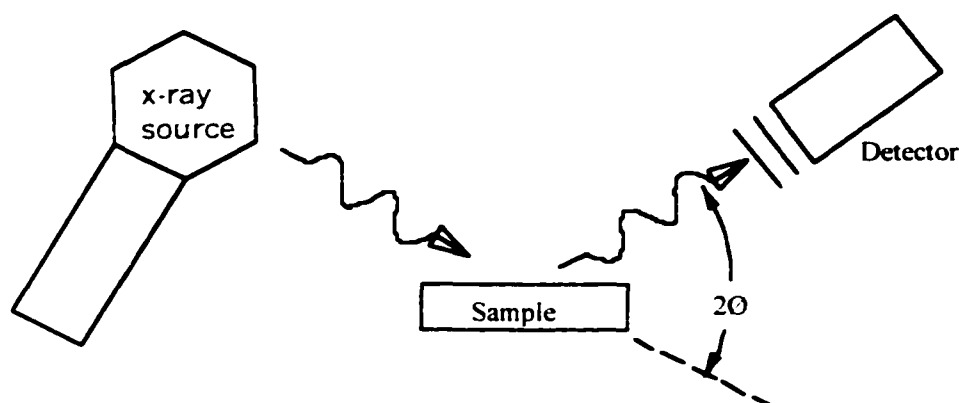

Figure 3.14: Geometry of the XRD experimental system.

One crystal parameter that can be measured using x-ray diffraction is the spacing between lattice planes, d. The geometry of the x-rays striking the crystal is shown in Figure 3.15. If the distance between the atoms is d, then the distance of ABC is 2d sin Ø. If the length of ABC is some multiple of the wavelength, then we will have constructive interference. In other words, at a certain point in space, both waves will be at a relative maximum or minimum at the same time. Hence we can write Bragg's Law as

$$n\lambda = 2d \sin \theta \qquad (3.25)$$

The diffractometer has a known λ and carefully controls Ø such that d can be precisely determined. From d and a knowledge of the Miller index of the plane, the cubic lattice parameter a can be found from

$$d = \frac{a}{\sqrt{h^2 + k^2 + l^2}} \qquad (3.26)$$

It should be noted that it is often observed that the a values of thin films are often shifted to

higher values than the a values of the same material in bulk form.[45]

Other structural information can also be determined from x-ray diffraction. Depending on the particular spectrum. x-ray information can be used to determine strain in the lattice.[46] If the film possesses homogenous strain. or macrostrain distributed throughout the sample. the values of the peak positions will be uniformly shifted. In thin films this usually shifts the d parameters to higher values. and can be measured along various crystal directions as.

$$p_{hkl} = \frac{d_{hkl} - d_{0_{hkl}}}{d_{0_{hkl}}}$$

(3.11)

where $d_{0_{hkl}}$ is the unstrained value of the d spacing of the hkl plane. d_{hkl} is the d value of the sample and p_{hkl} is the degree of strain in the {hkl} direction. Measuring this type of strain can be used. for example. to measure the lattice misfit between the film and the substrate. Inhomogeneous strain. or microstrain. that is different for different grains or may even differ inside one grain. will cause broadening of the diffraction peaks that increases with $\sin\emptyset$.
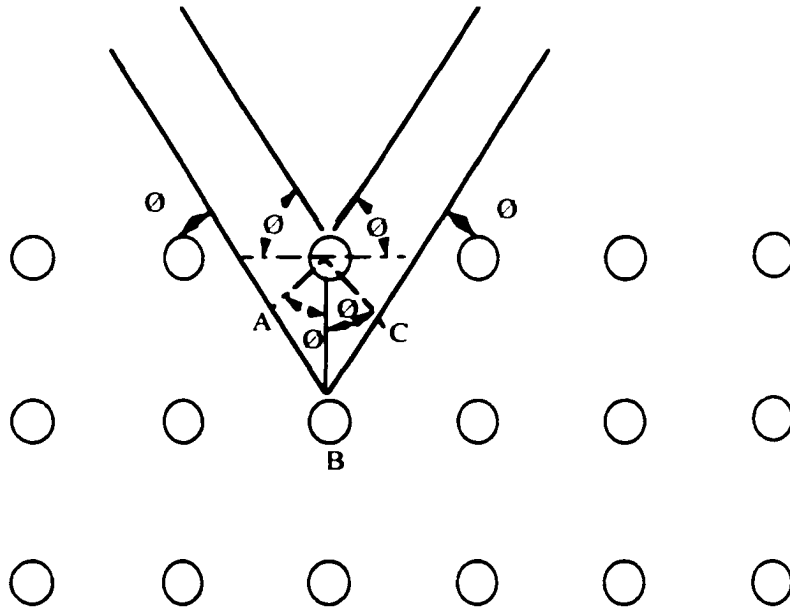
Figure 3.15:   Bragg scattering off a crystal.

If the film does not indicate the presence of inhomogeneous strain. then crystallite size of the grains can be estimated.[44] In this study the broadening of the diffracted peak was measured as simply the width of the peak at half of the intensity of the peak above the background level and then comparing this width to the width of a peak from a single crystal. such as a wafer. The peak width W can be related to the grain size of the film. D. by the

formula.[44]

$$D = \frac{k\lambda}{2W\cos\theta}$$

(3.12)

where λ is the wavelength of radiation. and k is a shape-characteristic constant that can be approximated by one for cubic structures. If the value of D is relatively constant for several planes in the sample. then its value can be used as an estimate of grain size. If the value of D increases with the order of reflection. then it is assumed that inhomogeneous strain is contributing to the peak width, and the two can only be separated by comparing to the spectra of standards of known grain size.

Since these films are grown on single crystal wafers. an epitaxial film should retain the same crystal orientation as the wafer. The single orientation of the wafer implies that only the planes that are perpendicular to that orientation will give rise to peaks in the XRD pattern. If the film is not epitaxial. and consists instead of randomly oriented crystalline grains. the XRD spectrum will appear as a powder diffraction. where all possible peaks are found in the spectrum. Thus. by comparing the found peaks in the XRD pattern of the film to the found peak in the XRD pattern of the wafer. a qualitative measurement of orientation can be made. The degree to which the film aligns itself to the orientation of the wafer gives and indication of whether or not the film is growing epitaxially.

Finally. by comparing the intensity of the diffraction peaks to the standard intensities found in the Joint Committee on Powder Diffraction Standards (JCPDS) Powder Diffraction File for germanium. a preferred orientation can be determined. The preferred orientation is determined from peak intensities that do not follow the trend of the JCPDS file. If the intensity of a particular plane is far greater than expected in relation to the other planes. then it can be inferred that the film possesses a preferred orientation to that plane.

3.2.2.3 Scanning Electron Microscopy (SEM)

SEM pictures were taken of the films in order to measure the film thickness. look for line or planar defects and to assess the overall morphology of the film. The SEM apparatus used was a commercial JEOL unit. supplied by the Materials Analysis Research Laboratory of ISU. The films were prepared for the SEM measurements by first cleaving the wafer and film along a crystal plane. Then the film and wafer were viewed from the side. Sufficient contrast was seen between the Ge and Si atoms to differentiate the film from the substrate. Ge films on Ge wafers could not be measured in this way.

One difficulty that arose in viewing the films in this way is that the top surface of the film scattered the accelerated electrons of the microscope in all directions. This resulted in a blurred image of the top surface. One correction of this problem is to tilt the top edge of the

film away from the accelerating gun. While this reduces the blur of the top edge. this also introduces error in the measurement of the film thickness because the parallax angle was not precisely known. Another way to reduce this problem is to reduce the accelerating voltage of the electron gun. Reducing the accelerating voltage also improved the detail of the planar features seen in the film.

Once an SEM image had been obtained. the pictures were digitized and the film thickness was measured using a Quartz software package. Any features such as defects or surface roughness were also measured in this way.

3.2.3 Electrical

3.2.3.1 Hall mobility

In order to determine the mobility of the majority carriers. Hall mobility measurements were made. The Hall mobility measurement is based on the Lorentz force acting upon free electrons in a semiconductor.[47] A conceptual picture of the experimental set-up is shown in Figure 3.16. As can be seen. a current is driven through the semiconductor by the application of V_A. These moving electrons tend to drift to the left in Figure 3.16. due to the Lorentz force. which is caused by the magnetic field. B. The drift of the electrons can be measured by the Hall voltage. V_H. By comparing the increase in voltage per unit increase in magnetic field strength. the mobility of the electrons can be found from.

$$\mu = \frac{\ln(2)}{\pi} \frac{I_{avg}}{I_{Hall}} \frac{1}{V_{avg}} \left(\frac{dV_{Hall}}{dB} \right)_{avg}$$

(3.13)

For the germanium carbide films grown for this dissertation. and for the room temperature Hall mobility apparatus used. there are two basic physical mechanisms that may change the mobility from sample to sample. The first mechanism is carrier scattering off ionized impurity atoms. such as dopant atoms. As the doping level from sample to sample varies. whether intentionally or otherwise. the carrier mobility will decrease. The second mechanism is scattering off neutral impurity atoms. such as interstial C atoms. and off defects. such as grain boundaries or lattice distortions due to the addition of C. As either the number of neutral impurities increases or the grain size reduces. the mobility will decrease.

3.2.3.2 Four point probe

Four point probe measurements were made on the films in order to determine the conductivity of the samples. The basic experimental set-up for a four point probe

measurement is to place four collinear probes into physical contact with the sample surface. A current is driven through the two outermost probes and the resulting voltage is read by the two innermost probes. The reason for using this arrangement[48] as opposed to just two probes that concurrently pass a current and sense a voltage. is that since the inner two probes pass essentially zero current, they are immune to the contact and spreading resistance experienced by the outer current carrying probes. Thus, the inner probes detect only the resistance of the semiconductor material. The resistivity of the sample can then be defined by the current supplied and the voltage measured as.

$$\rho = 2\pi s F \left(V/_I \right)$$ (3.14)

where s is the spacing between the probes and F is an added factor to correct for the geometry of the film. If the film thickness is much. much less than the probe spacing. the correction factor can be simply written as

$$F = \frac{t}{2s \ln(2)}$$ (3.15)

where t is the thickness of the films.

An important consideration in measuring thin films in this way is that the film is electrically isolated from the substrate. Failure to do so could result in erroneously measuring the resistivity of the substrate if the resistivity of the substrate is lower than that of the film. In this dissertation. isolation between the film and the substrate was achieved by junction isolation. An example of this is to grow an n-type film on a p-type substrate. The resulting depletion region at the junction is sufficient to isolate the two for these measurements.

B
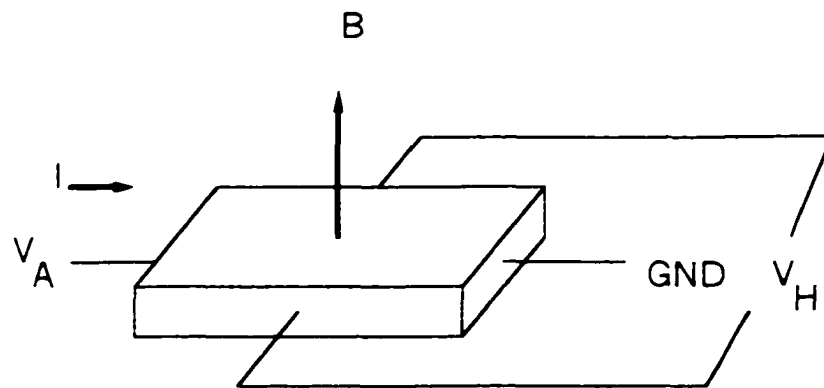
Figure 3.16: Conceptual picture of Hall mobility experiment[46].

Once the resistivity is measured. the conductivity can easily be found by inverting the resistivity. In addition. an estimate of carrier concentration can be made from.

$$\rho = \frac{1}{q\left(\mu_n n + \mu_p p\right)} \qquad (3.16)$$

Equation 3.16 can be simplified by assuming the film is nondegenerate. n-type and at room temperature.

$$\rho = \frac{1}{q\mu_n N_D} \qquad (3.17)$$

A similar equation can be written if the semiconductor is assumed to be p-type.

CHAPTER 4: DATA AND ERROR ANALYSIS

4.1 Experimental Design

This chapter will very briefly cover the choice of experimental design. the statistical methods used to analyze the data and how experimental error was dealt with. To begin this discussion. a brief overview of the design of the experiments will be given. The first type of experimental design that was used. and the experiment type that generated most of the data in this dissertation. is a two level full factorial design.[49] In performing this type of experiment. each of the experimental variables is varied between two levels. The result of the experiment. or in this case the material property measurement. is assumed to vary as according to a two level regression model. For example. if an experiment was done where growth rate is measured and pressure and microwave power are the variables that are set to one of two values. we could model the variation in the growth rate by.

$$y = \beta_o + \beta_1 x_1 + \beta_2 x_2 + \beta_{12} x_1 x_2 + \varepsilon \qquad (4.1)$$

There are several important features of equation 4.1. The value of the growth rate is represented by y. The right hand side of the equation is a linear equation. and hence. this is a linear regression model. The linearity of this model is important to note. as it is assumed that changing the experimental parameters has a linear effect on the outcome of the experiment. The assumption of linearity will have an impact on the experimental design and on how the levels the experimental variables are chosen. The constant β_0 is the average growth rate for the entire experiment. The constants β_1 and β_2 are proportionality constants that refer to pressure and power respectively. The variables x_1 and x_2 refer to the level pressure and power are set to. respectively. The term that contains the constant β_{12} and both experimental variables is perhaps the most powerful feature of this model. This term accounts for the interaction of the two experimental variables. In other words. not only does the model account for how changing a variable affects the outcome. the model also accounts for how changing one variable affects other variables. Even though this is a linear model. some non-linearity in the measured property can be accounted for if there is a strong interaction between the experimental variables. Many times in the data analysis. the interaction between variables was very helpful in determining how the deposition parameters affected the material properties. The last term. ε. represents the random error in the experiment. in the measurement. or both.

In designing the experiments it was desired to obtain the most information in as few

samples as possible. To do this a single replicate of the experiment was done. To explain this. consider the first milestone to be accomplished. the growth of Ge films on Si wafers. For this experiment there were four experimental variables. which were pressure. microwave power. substrate temperature and H_2 flow rate. Each of the variables was varied between a low setting and a high setting. In order to grow samples with every possible combination of the deposition parameters. a total of 2^4 or 16 samples would need to be grown. Table 4.1 shows the possible combinations. with the high and low settings represented by + and - . respectively. In actuality

Table 4.1: 2^4 factorial experiment combinations.

Sample #	Pressure	Power	H_2 Flow	Temperature
1	+	+	+	+
2	-	+	+	+
3	+	-	+	+
4	-	-	+	+
5	+	+	-	+
6	-	+	-	+
7	+	-	-	+
8	-	-	-	+
9	+	+	+	-
10	-	+	+	-
11	+	-	+	-
12	-	-	+	-
13	+	+	-	-
14	-	+	-	-
15	+	-	-	-
16	-	-	-	-

the samples would not be grown in this order. but instead the combinations would be run randomly in order to guard against a systematic error in the experiment. The problem with this experimental design is that since each combination is only used once. there is no way to tell if the material property being measured changes because of the effect of changing the experimental factors or because of random error in the experiment or the measurement. However it is often the case. and it was the case for each of the experiments done for this dissertation. that not every one of the experimental variables has a significant effect on the property being measured. For example. if growth rates are being measured. for the sake of argument assume that substrate temperature does not significantly affect growth rate. If this

is assumed from the data analysis, one can neglect the combinations where only the level of temperature changes. If one neglects temperature, Table 4.1 shows that one now has two identical replicates, with one set being samples 1 – 8 and the other set being samples 9-16. If the data analysis shows that two factors can be neglected for the next material property that is measured, then we will have four replicates with which to estimate the random error. The way that the significance of experimental variables is quantified will be described below.

An additional way to estimate the error, and also a way to test the assumption of linearity discussed above, is to add centering points to the experimental design.[48] Centering points are essentially samples that are grown with deposition parameters which are half way between the levels used in the factorial experiment. If one again uses the example where pressure and power are our experimental variables, Figure 4.1 illustrates the parameters that would be used for centering points. Figure 4.1 shows the required four samples that are needed to test all combinations of the two experimental variables. The fifth sample is placed where the centering point should be. The parameters for sample five would be 150 W and 7.5 mTorr. The centering sample can be repeated several times to find the random error for that setting, and this error can be used to estimate the error for the rest of the samples. Additionally, a plot of the material property being measured versus power would show three points now, instead of only two if no centering point were present and hence an obvious test for linearity readily exists. The use of centering point samples enables an estimate of error and a test for linearity in a much more efficient manner than if three levels for each of the variables was used or if multiple replications of the entire experiment were made.
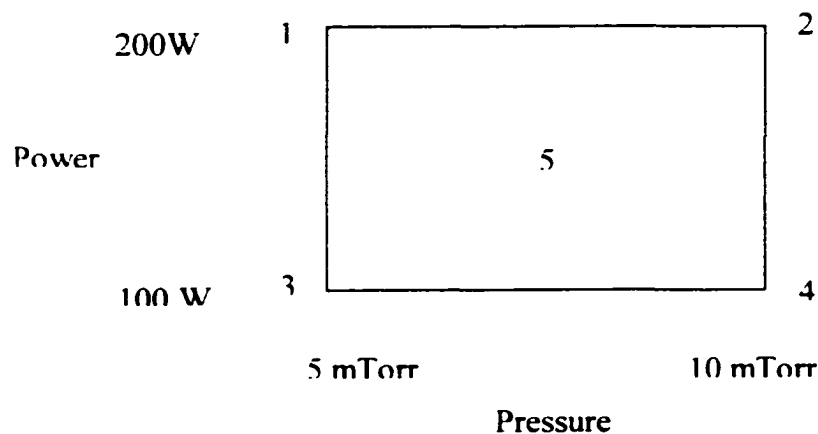
Figure 4.1: Illustration of centering point sample.

The assumption of linearity is a very important consideration when the levels for each experimental variable are being set. Figure 4.2 illustrates the reason for this. As shown in Figure 4.2 there exists a clear linear region as the maximum growth rate is approached. and a clear parabolic region around the area in deposition space where the maximum point exists. This is very representative of most experiments. Since the factorial experiment assumes linearity in the effect of the deposition parameters. for this example the power levels should be set at 100 and 200 W, with a centering point at 125 W. Once the effect of power has been quantified by the factorial experiment. then further experiments can be done to find the optimal power setting, as will be discussed later in this chapter. Obviously. it is impossible to have this data before the factorial experiment is done. but the correct variable levels can be guessed at. based on knowledge of previous experiments or on related experiments. such as plasma characterization data in this instance.
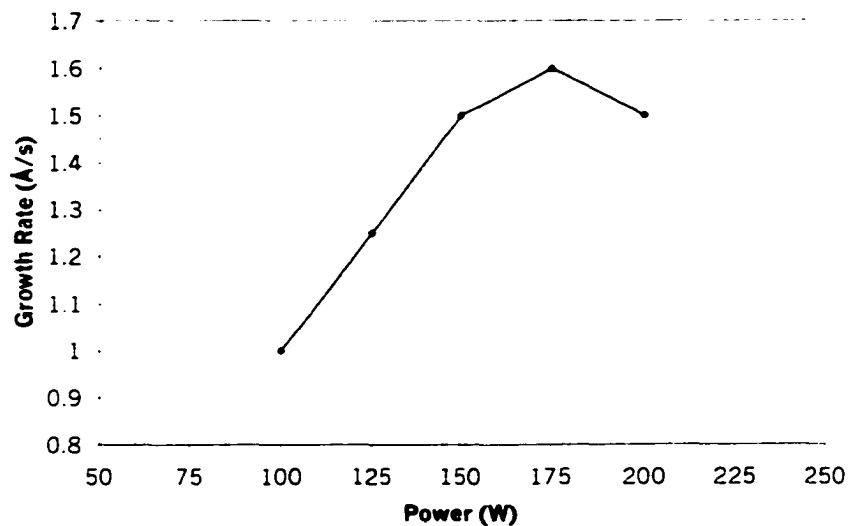
Figure 4.2: Linear and parabolic regions of experimental values.

4.2 Data Analysis

The basic tool used for analyzing the data of these experiments was an analysis of variance (ANOVA) table. The ANOVA table is used to generate the quantitative effect each variable has on the outcome of the experiment, the quantitative effect of each interaction between the various variables. and how these quantities compare to the random error of the experiment.[50] The basic way the ANOVA table produces these quantities is to take all of the measurements from the experiment. and compare the measurements to an F distribution about the mean measurement value. The number of variables in the experiment determines

the shape of the F distribution, and the width of the central peak is determined by the error in the experiment, which can be determined by repetition or centering points as described above. Any experimental measurements that fall inside the central peak of the F distribution are considered to vary only because of the experimental error. Any measurements that fall outside of the central peak are considered to possibly vary because of changes to the variables. If every time a certain variable is changed the measurement also changes outside of the central peak in a predictable way, then the change in the measurement is attributed to the effect of the variable. If the measurement only changes some of the time the variable is changed, the variable is considered to only have a slight effect on the measurement. A similar test is used on the interaction of factors.

The way that quantitative values are obtained is that the percentage change of the measured value each time the variable is at the high value is subtracted from each time the variable is at the low setting. Each of these values is squared and summed. These sums are then divided by the percentage change due to experimental error.

4.3 Process Optimization

Once the quantified effect of each variable and interaction of variables is known, a predicted values model can be constructed. The predicted values model will, as the name suggests, predict the value of the measurement over a continuum of variable values. The model can predict measurements within the regime that the actual experiment was done, and it can also predict measurements slightly outside of the range where actual measurements were taken. However, it should be reemphasized that since the predicted values model is a linear model, care should be taken when predictions are made outside of the range where measurements where taken. Figure 4.2 illustrates this. If higher powers than 150 W are predicted, the linear predicted values model will probably inaccurately predict the outcome of the measurement.

To construct the predicted values model, the quantified effects of the variables, or interactions of variables, are used as the β coefficients in equation 4.1. The values of the variables are used as the x variable in equation 4.1. Finally, the experimentally determined random noise is used for ϵ. With all of these values, any combination of variable can be used to predict a measurement value, y.
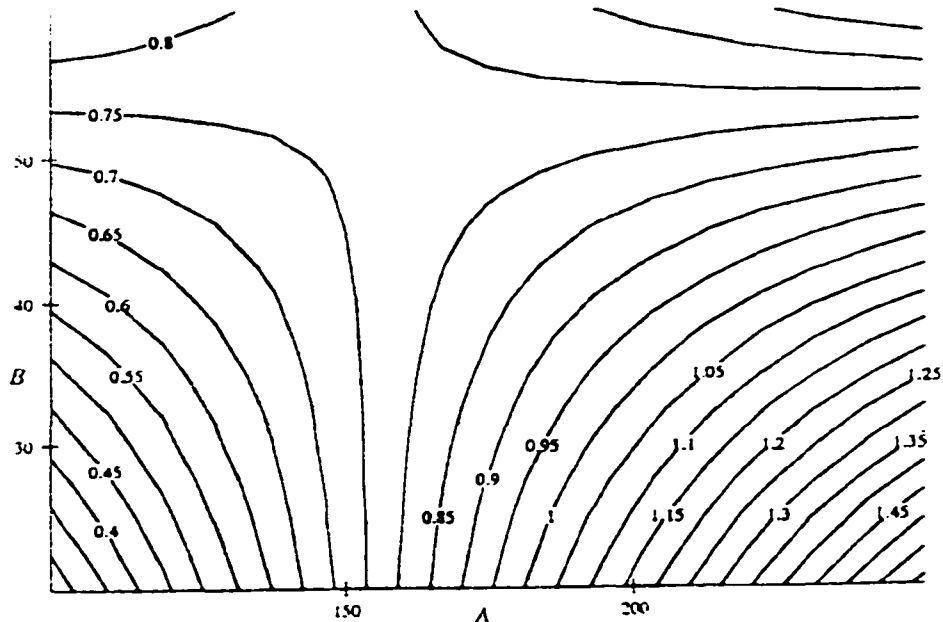
Noting that the predicted values model only contains what are believed to be the important variables, it is important to test the validity of this model. This can be easily done by taking the quantified effects of the important variables and dividing them by all of the

quantified effects of all of the variables. If this ratio is close to one, then it is believed that all of the important factors have been found. A way of expressing this ratio is to say that the variables selected represent a certain percentage of the variability in the experiment.

Graphical representations of the predicted values model are useful ways to visualize how the measurement value changes in parameter space. A three dimensional plot of the predicted values model is called a response surface. An example of a response surface is shown in Figure 4.3, where growth rate is the measured value. The relative maxima and minima instantly identify the areas of parameter space that warrant further investigation. Although the predicted values model is a linear model, non-linearities exist in the plot because of the interaction between variables. Because only two experimental variables can be plotted at once, numerous response surfaces must be generated for all of the possible combinations of the rest of the variables. Another useful graphical tool is a contour plot of the predicted values model, shown in Figure 4.4. Contour plots are very useful in that the plots for different measurements can be overlapped to find regions in parameter space where desirable values of both measurements exist.
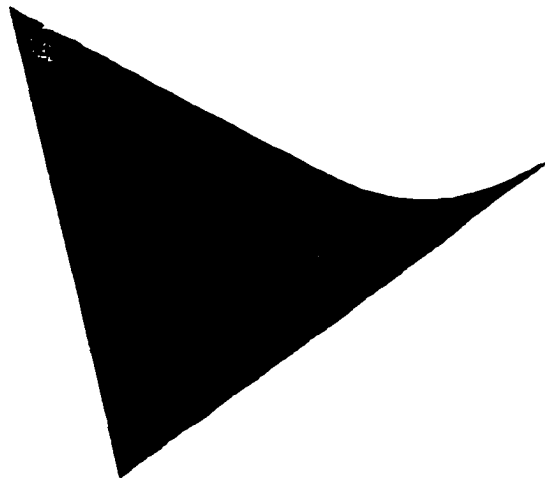
Figure 4.3: Response surface for growth rate.

Figure 4.4: Contour plot for growth rate.

The predicted values model can also be used to develop parameters that will optimize the measured values. This is done by changing the experimental variables in the direction that improves the predicted value. Actual experiments are then done with these new parameters. and incremental steps are made in that direction until the measured value stops improving. At this point the new parameters can be kept as the approximate optimal variables. or a new factorial experiment can be done in this region. provided the experiment is based on a quadratic predicted values model.

4.4 Error Analysis by Residuals

A few comments will be made about the analysis of error. Determination of the experimental error has been discussed above. In addition to the experimental error. several other error issues can be analyzed through the use of residuals. Residuals are the difference between the value of the measurement from the experiment and the value of the predicted values model. using the same parameters as what were used in the experiment. This difference is known as the residual for the measurement.

The first test of a residual is to convert it to a standardized residual. This is done by dividing its absolute magnitude by the square root of the experimental error. If a normal distribution is made of the standardized residuals. none should fall outside 3 or 4 standard

deviations. If any of the standardized residuals fall outside these boundaries. that measurement should be called into question. The measurement should be double checked for errors and repeated if necessary. It is important to rid the data of any spurious measurements. as they can wrongly affect the importance given to the experimental variables.

Several other tests can also be done with the residuals. The residuals can be plotted against the time at which the experiment was performed. If the value of the residuals increases or decreases with time. a systematic error in the experiment can be detected. Another test would be to plot the residuals against the value of the variable setting. This will reveal if more or less error occurs when one of the variables is set to a particular value. A similar plot would be to compare the residuals and the value of the measurement to see if the amount of error increases with the size of the measurement. A final test is to simply plot the residuals versus the variable settings and to just look for any type of pattern. For example. if the value of the residuals all increase and then all decrease as the experimental variables are increased in values. then a systematic error in the experiment may exist.

# CHAPTER 5: RESULTS AND DISCUSSION

5.1 Ge Films on Si Substrates

5.1.1 Growth rate

The first experiment done. with regard to germanium films grown on silicon substrates. was an analysis of growth rate. From the statistical analysis of the data. it was found that the standard error for the experiment was ± 0.15 Å/s. This error was believed to be sufficiently small. The most important experimental variables that affect the growth rate are power. H_2 dilution and pressure. Modeling these factors with a linear predicted values model gives a regression fit factor of 0.73. indicating an acceptable fit. Another way of stating the regression fit is to say that 73% of the variation in growth rate that was seen can be explained using only the variables listed above. Analysis of the residuals does not indicate any obvious systematic error in the data.

The major single variable effects will be discussed. in addition to the two major variable interactions. Three variable interactions and higher will not be discussed. even though they may have been used in constructing the predicted values model. due to their complexity. As can be seen in Figure 5.1, increasing the microwave power from 150 to 200 W increased the growth rate from 0.66 to 0.85 Å/s. This is attributed to an increase in electron temperature at higher powers that increases the amount of dissociation in the plasma. This increases the production of radicals. which increases the deposition rate. Figure 5.1 also shows that the data are somewhat non-linear. as were all of the single variable data. and this resulted in reducing the linear fit of the data to the model. As can be seen in Figure 5.2, decreasing the H_2 dilution from 80:1 to 40:1 increased the growth rate from 0.65 to 0.86 Å/s. It is believed that the lower H_2 dilution decreases the in situ etch rate. So. that rate of deposition is proportionally greater than the rate of removal. In addition. as H_2 is increased. the number of gas phase collisions is increased. which may reduce the electron temperature of the source. Increasing the pressure from 7 to 13 mTorr increased the growth rate from 0.66 to 0.85 Å/s, as seen in Figure 5.3. This was an unexpected result. It is believed that the higher pressures and the resulting shorter mean free path lengths lead to a reduced etch rate and hence. the growth rate increases.
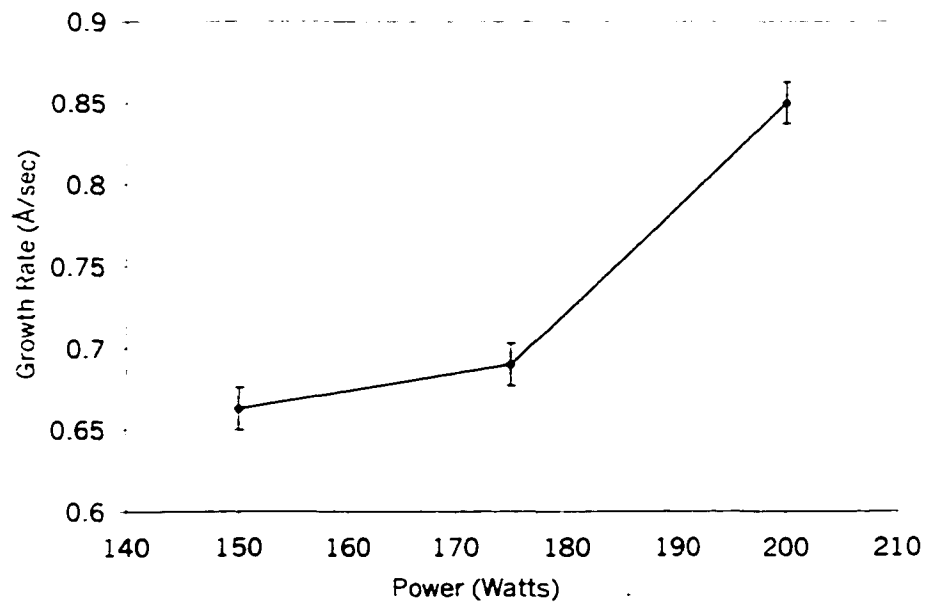
Figure 5.1: Growth rate increases as power increases.
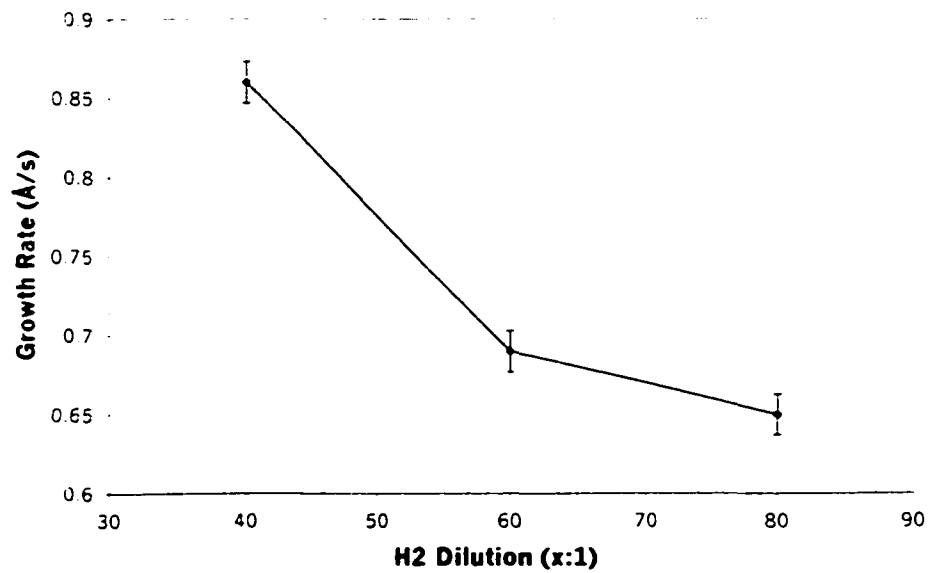
Figure 5.2: Growth rate decreases as H_2 flow increases.
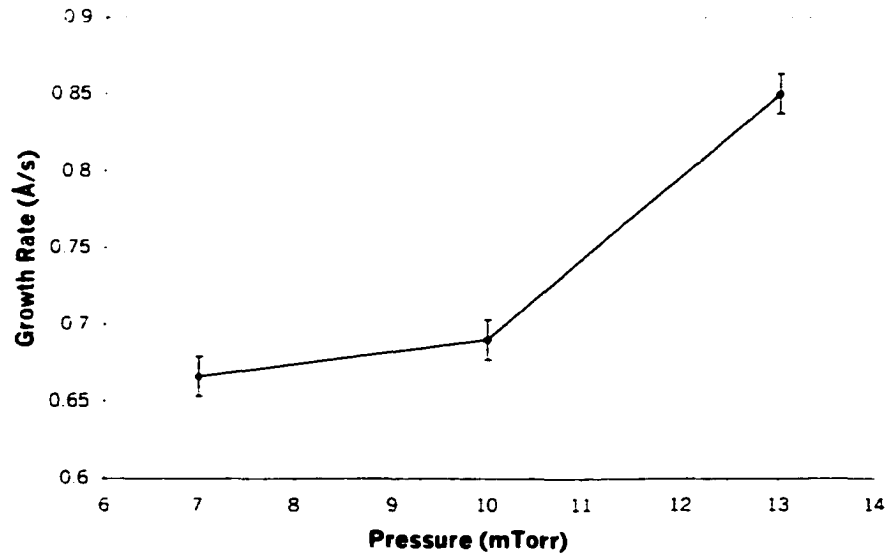
Figure 5.3: Growth rate increases as pressure increases.

The statistical analysis also showed that two two variable interactions and two three factor interactions are important. The interaction between temperature and pressure was significant. At 350° C. changing the pressure has little effect on the growth rate. But at 550° C. changing the pressure from 7 to 13 mTorr increased the growth rate from 0.55 to 0.98 Å/s. Based on the above pressure data, where it was believed that higher pressures reduced the etch rate. it seems here that the addition of high temperatures improves the crystallinity of the material and this also reduces the etch rate. So the combination of high pressures and high temperatures increases the growth rate by a large margin.

The other two factor interaction was between pressure and H_2 flow. For all cases. increasing pressure increased growth rate. But the growth rate was highest when H_2 flow was lowest. This strongly indicates that the principle limiting factor in the growth rate of the material is the etch rate. Here. the higher pressure and lower flow of H_2 both lowered the etch rate. which in turn increased the growth rate.

5.1.2 XRD grain size and structure

In nearly all of the samples that were grown. the XRD pattern indicated that the films had aligned themselves to the single crystal orientation of the Si wafer. In other words, the grains of the films were growing heteroepitaxially. Of the few films that did not align to the Si crystal. the general deposition parameter settings that led to powder-like films were high

powers. high H_2 dilution and low temperatures. As will be explained below. these types of parameter settings reduced the grain size. and it is believed that a very small grain size kept the film from aligning itself to the crystal order of the substrate.

The 2^4 factorial experiment for grain size showed that the standard error for the experiment was ±175 Å. which is fairly low in comparison to the effect of the important factors. The important factors were shown to be power, H_2 dilution. a two factor interaction between power and H_2 dilution. and a two factor interaction between temperature and pressure. Using these factors in a linear model gives a fit parameter of 0.73. which is a reasonable fit. It was surprising that temperature was not an important single parameter, and thus one must conclude that the etching effect of the H ions. and the surface diffusional energy imparted by the plasma are more important than the energy imparted by the substrate temperature. for the temperature range in which the samples were grown.

As the power was increased from 150 to 200 watts. the grain size decreased from 740 Å to 364 Å. as shown in Figure 5.4. This suggests that the higher powers are not beneficial for two possible reasons. First. as the power increases. the growth rate also increases. Thus. any particular 2-D layer does not have time to coalesce its grains before another 2-D layer is deposited over it. A second possibility has to do with plasma damage. As stated in earlier chapters. the H beam produced in the plasma etches the film during growth. It is also true that the H beam etches the substrate during the initial stages of growth. If the energy of the H beam is too great. this etching can damage the growth surface by producing point defects in the crystalline structure. In this case. higher powers do more damage to the film. and produce more point defects on the surface. These point defects serve as nucleation sites. which act as a growth site for grains. So if more point defects are created. more grains start to grow on the surface. As stated earlier. higher powers also increase the growth rate. and so these grains may not have time to coalesce. This results in an overall smaller grain size for the film.

As the H_2 dilution was increased from 40:1 to 80:1. the grain size decreased from 798 Å to 306 Å. as shown in Figure 5.5. This is most likely due to the increase in H ion bombardment at the higher H_2 flow. The increased H ion bombardment leads to an increase in plasma damage and hence to an increase in defect sites. These data reinforce the idea of plasma damage limiting grains size. as was discussed with the power data.

The two variable interaction between power and H_2 dilution showed that when the power was at 200 W. changing the H_2 dilution had little effect on the grain size. However. when the power was 150 W changing the H_2 dilution from 80:1 down to 40:1 greatly increased the grain size from 287 Å to 1194 Å. This strongly indicates that power and H_2 dilution should both be lowered to maximize the grain size. The growth rate and plasma damage explanations given above can both explain this result. and both ideas are reinforced by this result. It also seems to indicate that power has more of an effect on the amount of plasma damage than the flow rate of H_2. This seems reasonable. because if the H ions are of low energy. an abundance of H ions will not do more damage to the growth surface.
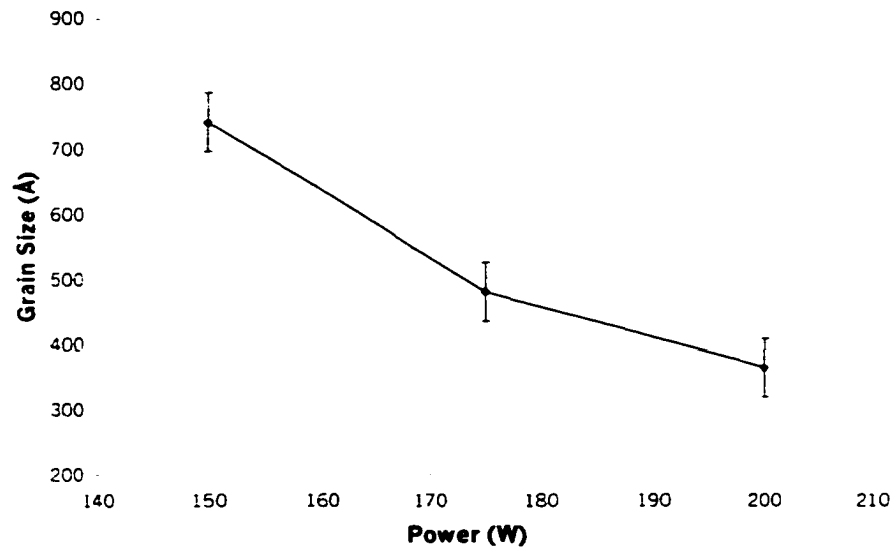
Figure 5.4: Grain size decreases as power increases.

The two variable interaction between temperature and pressure showed that at high pressures. changing the temperature had little effect on the grain size. But at lower pressures. decreasing the temperature from 550° C to 350° C decreased the grain size from 800 Å to 250Å. This can best be explained by considering that at low pressures. the growth rate is slower. Combining a slower growth rate with a higher temperature allows the grains time to coalesce. The higher growth rate at the higher pressure apparently negates the benefit of higher temperatures.

Based on the findings of the factorial experiments. the grain size of the Ge films was optimized. using the optimization techniques discussed in earlier chapters. Two different regions of parameter space were explored. The first region consisted of higher temperatures, higher powers and higher H_2 dilutions. The best grain size obtained from this region was 5574 Å. which is nearly twice as large as any sample from the factorial experiment. Earlier in this section it was shown that high powers and high H_2 dilutions produced many grains on the growth surface. But apparently the higher temperature of this sample. combined with a slower growth rate. was sufficient to coalesce the grains into larger ones.
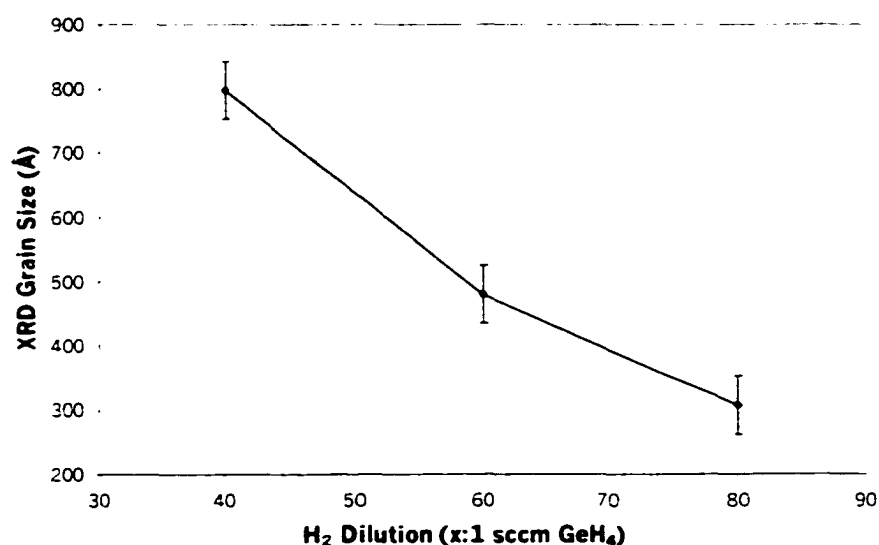
Figure 5.5: Grain size decreases as H_2 dilution increases.

The second region that was explored used lower powers. lower H_2 dilutions. and was grown at a slightly lower temperature than the previous sample. The best grain size achieved was 2353 Å. So it seems that the ion bombardment is less of a problem at high temperatures because the ion energy lowering parameters of this sample reduced the grain size.

5.1.3 Raman crystal structure

From the 2^4 statistical analysis. the standard error for this experiment was 1.17 cm^{-1}. which is relatively large. The important variables were found to be H_2 dilution and pressure. and there was an important three parameter interaction between power. H_2 dilution and

temperature. A linear model was fit to these factors and a regression fit of 0.64 was obtained. This is a low value for the fit parameter, and it is probably due to the high experimental error. It seems reasonable to assume that these two parameters are important to crystallinity. It is surprising though that power did not have a large effect on the crystallinity by itself. This suggests that the etching effect is the same for 150 W as it is for 200 W. This would seem to indicate that 150 W supplies sufficient energy to break Ge - Ge bonds. Since the Ge - Ge dissociation energy is only 274 kJ/mol, compared to 460 kJ/mol for Ge - C bonds, this seems reasonable. It was also interesting to note that temperature by itself did not have a large effect on the FWHM values. Thus it seems that the benefits to grain size from the etching effects of the H ions are more important than the benefits of temperatures up to 500° C.

As the H_2 dilution is increased from 40:1 to 80:1, the average FWHM value decreases from 8.1 to 5.8 cm^{-1} as shown in Figure 5.6. Therefore the extremely high dilution of H_2 is beneficial to growing crystalline films, and the importance of in situ H ion reactive etching is reinforced. The second possible explanation for this effect is that the high H_2 flow makes the plasma source more uniform. This concept was discussed in an earlier chapter. As stated earlier, this produces primarily only one type of radical, which is very beneficial to growing crystalline films.

As the pressure was increased from 7 to 13 mTorr the FWHM value decreased from 7.6 to 6.2 cm^{-1}, as shown in Figure 5.7. This is somewhat surprising in that it seems to almost contradict the findings of the H_2 dilution effect. As pressure is increased, the mean free path is reduced, less H ions make it to the substrate, and the etch rate decreases. Despite this, the crystallinity improves at higher pressures. Secondly, it was found from the growth rate experiment that the growth rate is higher for higher pressures. This is also confusing because this would lead one to expect more crystalline films at the lower pressure where the growth rate is slower. But since the films are more crystalline at higher pressures, the conclusion that must be reached is that the higher pressures work with the H_2 dilution to make the plasma more uniform. Again, as the pressure of the H_2 increases, it suppresses the production of the H_2 byproduct. So if the overall pressure of the chamber is raised, then the partial pressure of the H_2 gas is also raised. And again, the higher pressure should enhance the uniformity of the plasma. In review of this pressure data and comparing it to the H_2

dilution data, it seems that making the plasma more uniform is the most important factor in growing crystalline films.

Based on the data of the factorial experiment, minimization of the Raman FWHM was attempted. Although several parameter regions were explored, the FWHM value could not be reduced much from the lowest values in the factorial experiment, which were approximately 5 cm^{-1}. The reason the value could not be minimized further is most likely due to the large experimental error and the consequential low fit parameter for the linear model. In other words, because the model did not fit the data very well, optimization using the model did not work very well.
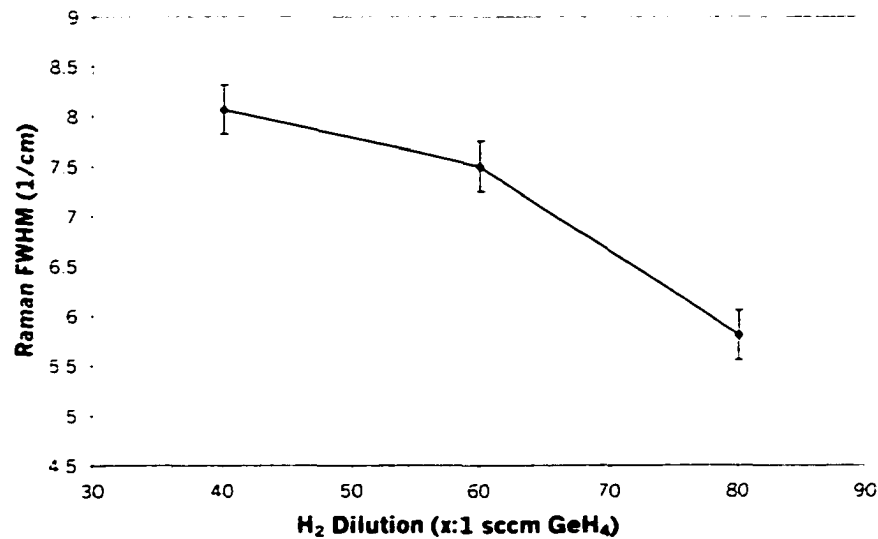
Figure 5.6: Raman FWHM decreases as H$_2$ dilution increases.

5.1.4 Conductivity and mobility

Electrical measurements were also made on the Ge films to determine how the material properties affected carrier transport. Conductivity measurements were made on the films, and the average value of the conductivity was approximately 1.8 1/Ω•cm. This corresponds to a doping level of approximately 3 E 15 cm^{-3}.

Mobility measurements were made using the Hall mobility apparatus. The films had an average value of approximately 1200 cm^2/V•s. The values did not vary much depending on the grain size of the material. The mobility of single crystal Ge is 3900 cm^2/V•s. The lower mobility of these films indicates that they are polycrystalline.
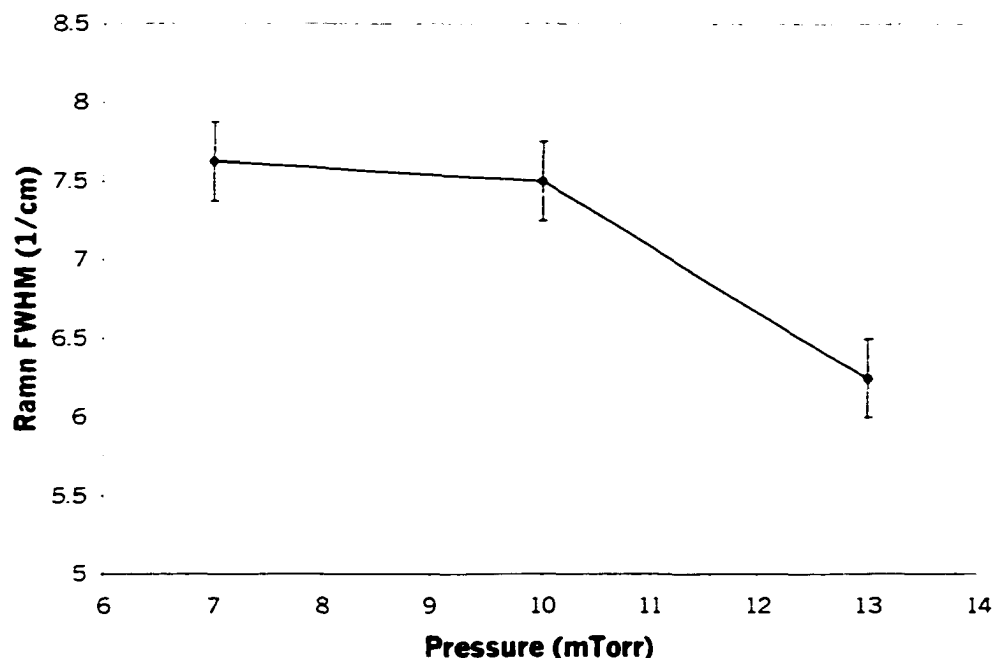
Figure 5.7: Raman FWHM decreases as pressure increases.

5.1.5 Bandgap

The bandgap of the films was determined using the spectrophotometer. The value of the bandgap was plotted as a function of grain size and as a function of crystal order as determined by Raman FWHM. The results of this are shown in Figures 5.8 and 5.9 respectively. As can be seen, the bandgap increases rapidly below about 200 Å for the E_t bandgap data, and below approximately 400 Å for the E_{04} data. On the other hand, the increase in bandgap due to an increase in Raman FWHM is more continuous and much more subtle. While these results are predictable, it is important data to have because in the germanium carbide experiments, the increase in bandgap as a function of C content will be determined. So increases that are due to reduced grain size or reduced crystal order need to be filtered out of the data in order to that the true increase solely from the presence of substitutional C could be determined. Failure to filter the data would undoubtedly result in an erroneous increase in bandgap per atomic percent C, as the incorporation of C often degrades the crystallinity of the sample, and this degradation of the crystallinity would increase the bandgap in and of itself.
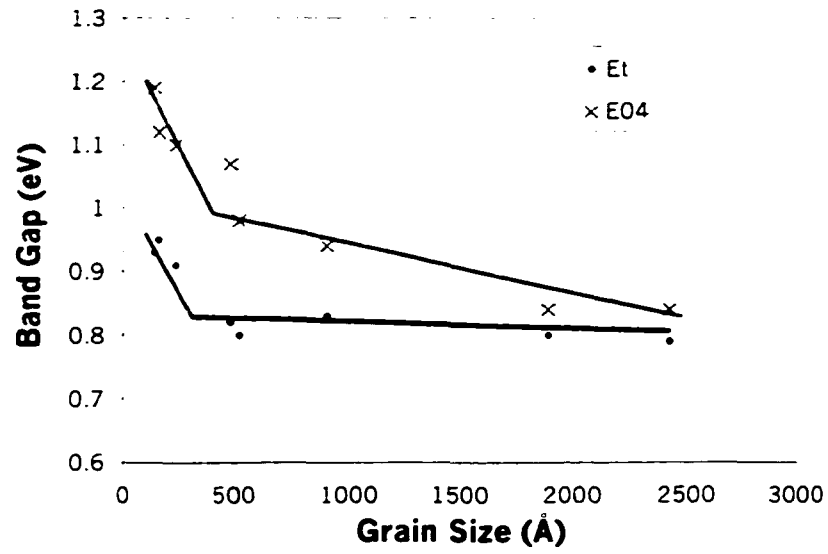
Figure 5.8: Bandgap increases rapidly below approximately 200 Å.
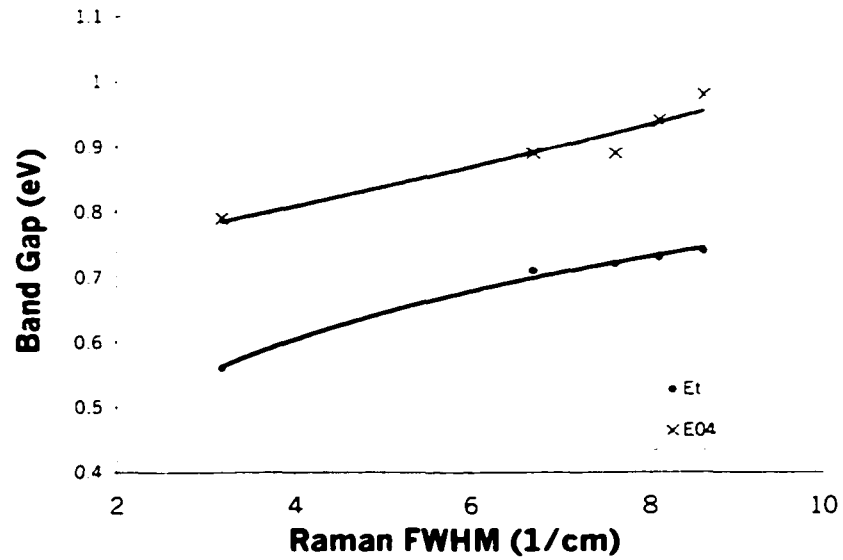
Figure 5.9: Bandgap increases moderately as Raman FWHM increases.

5.2 Ge Films on Ge Substrates

The next set of experiments studied Ge films grown on Ge substrates. The purpose of these experiments was to compare these films to the Ge films that were grown on Si substrates. To make Raman measurements of the films, a different experimental set-up needed to be used. This is because the spectra of the Ge wafers had a background that was so large that it obscured the Ge peak. From the literature concerning Raman measurements of single crystal Ge[51-52], it was found that a laser wavelength of approximately 500 nm or 1500 nm needed to be used. Hence, a Raman system provided by Glen Schrader of the Chemical Engineering Department of ISU was used, as it used a wavelength near 500 nm. The Raman data of the films showed little difference between the peaks for the Ge substrates and the Ge films. A comparison of the peaks for the wafer, for the film at the top surface, and for the film in the bulk of the material is shown in Figure 5.10. All of the peaks were centered on 303 cm^{-1}, and they were very symmetrical. The spectra of the top surface of the film shows a much more intense background curve and additional broad peaks, both of which indicate the presence of impurities on the surface of the film. The intensity of both peaks was nearly the same. The FWHM value of the film peak was increased by approximately 10%, which indicates that the crystal quality of the film was slightly degraded as compared to the wafer, although the two peaks are very similar.

XRD measurements of the Ge wafer and film showed the Ge peaks were similar in position and shape. The pattern for the film indicated that the film was of the same single orientation as the wafer. The peaks for the wafer and the film were much broader than peaks for Si wafers, which indicates alignment problems with the Ge wafers.

5.3 Ge$_{1-x}$C$_x$ Films on Si Substrates

The next set of experiments involved the growth of Ge$_{1-x}$C$_x$ films on Si. First the plasma source was characterized using OES. Next, a full factorial experiment was done for these samples in a similar manner to the Ge on Si wafers experiment above, however, a five variable experiment was used instead of a four variable experiment. The extra variable was the flow rate of methane gas, which was the C source.

5.3.1 Characterization of Ge$_{1-x}$C$_x$ plasma

As was stated in earlier chapters, the first step in understanding the deposition process is to understand the plasma source. To this end, OES characterization of the plasma source

was done. The measurements were done to qualitatively measure the amount of different species in a $Ge_{1-x}C_x$ plasma. Although several species were measured, only the results concerning the dissociation of H_2 will be discussed in this section. The reason for concentrating on these results is that they give a qualitative understanding of how the electron temperature varies in the plasma. The electron temperature is important to creating radicals and to in situ etching.
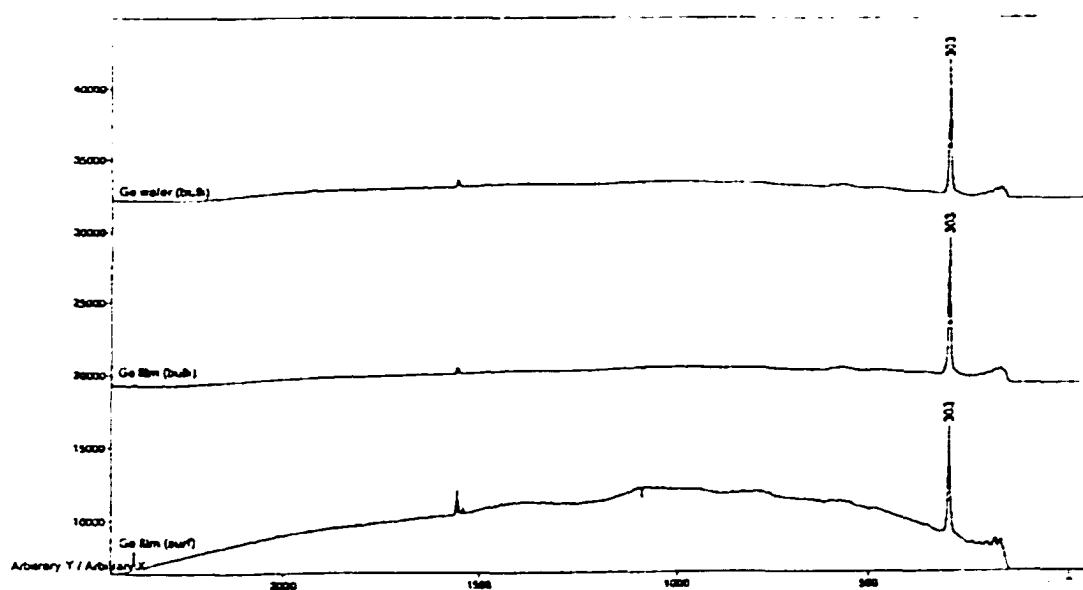
Figure 5.10:   Raman spectra of Ge wafer, Ge film at the surface of the film, and the Ge film in the bulk of the film.

A factorial statistical experiment was performed on the OES measurements, where power, pressure, the flow rate of H_2, the flow rate of CH_4, and the flow rate of GeH_4 were varied. The results of the statistical analysis showed that the standard error in the H_α/H_2 ratio was ±0.00864, which is very small in comparison to the effects of the variables. The low error is undoubtedly attributable to the high precision of the OES unit. The important parameters identified were the flow rate of GeH_4, pressure, power, and H_2 flow, a two variable interaction between H_2 dilution and GeH_4 flow rate, and two three variable interactions. Using these four variables in a linear model explains only 61% of the
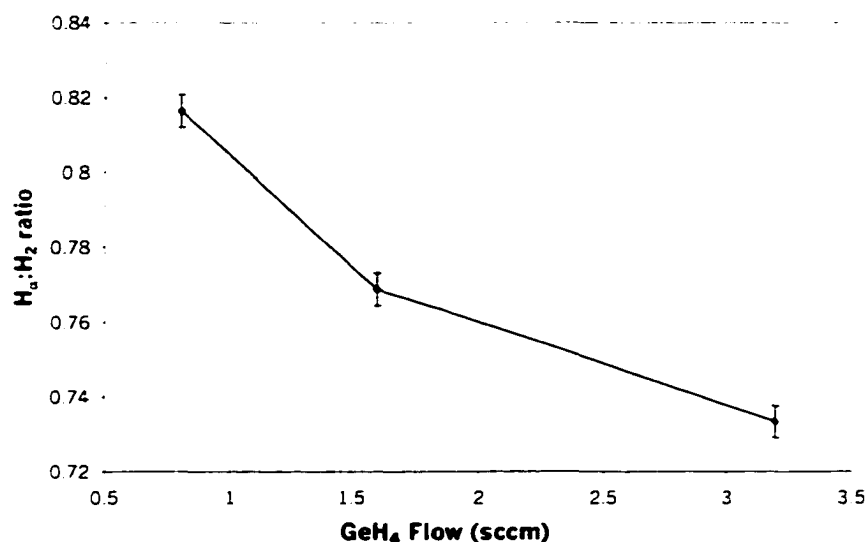
variability. Since so little of the variability was explained. a more complete error analysis was performed on the data. as will be explained below.

As the flow rate of GeH_4 was increased from 0.8 sccm to 3.2 sccm. the H_α/H_2 ratio decreased from 0.82 to 0.73. as can be seen in Figure 5.11. This was by far the biggest effect of all the parameters. This effect is attributed to lowering of the electron temperature by inelastic collisions in the gas phase between GeH_4 molecules and thermal electrons. These inelastic collisions cause the electrons to lose energy, and the average energy of all the electrons in the source is reduced. This has the effect of reducing the electron temperature. and hence. fewer of the H_2 molecules are broken apart. The reason this effect is not as large as when the CH_4 flow is raised. is that the GeH_4 is a much larger molecule than CH_4 and hence. it has a much larger cross section for electron impact. Another possible reason is that GeH_4 has lower lying electron orbitals available for impact excitation. Thus. the effect of increasing GeH_4 flow is much larger than the effect of increasing CH_4 flow.

As the pressure was increased from 7 to 13 mTorr. the H_α/H_2 ratio decreased from 0.8 to 0.75. This effect is also most likely caused by an increase in gas phase collisions. and reinforces the ideas described above. This effect could also be possibly attributed to a decreased mean free path at the higher pressures. Since the OES scan was done in the general area of the substrate holder. which is approximately 20 cm from the plasma source. the number of metastable species reaching the substrate holder area was greatly reduced. Similarly. as power was increased from 100 to 200 W. the H_α/H_2 ratio decreased from 0.84 to 0.79. This can again be attributed to an increase in gas phase collisions.

As the flow of H_2 was increased from 15:1 to 30:1. the ratio increased from 0.8 to 0.84. This seems somewhat contradictory to the idea of increased collisions at higher gas flows. One possible explanation is that H_2 is a smaller molecule and hence. it does not present as much of a problem with collisions. The higher flow rate, however. does result in more H_2 molecules being available to be dissociated. This may indicate that there are more energetic electrons present than H_2 molecules. Examining the two variable interaction between H_2 dilution and GeH_4 flow rate. which can be seen in Figure 5.12. can test this idea. The data indicated that for both 30:1 and 15:1 H_2 ratios. increasing the GeH_4 flow rate lowered the H_α/H_2 ratio. But at the low GeH_4 flow rate the 30:1 H_2 dilution had a higher H_α/H_2 ratio. while at the higher GeH_4 flow rate the 15:1 H_2 dilution had a higher H_α/H_2 ratio.

This effect is attributed to an increased amount of H_2 dissociation at the lower GeH_4 flow rate by the higher number of H_2 molecules available with the higher H_2 dilution. But at the higher GeH_4 flow, the increased number of H_2 molecules only adds to the lowering of the electron temperature by inelastic electron collisions. as described above.

Figure 5.11: Electron temperature decreases as GeH_4 flow increases.

Because the linear model explained so little of the variability in the experiment. a more in depth error analysis was performed. The residuals vs. normal probability showed that the data followed a normal distribution. aside from the effects of the important parameters. The residuals vs. fitted values showed no type of pattern in the data that would indicate a systematic error. Residuals vs. GeH_4 flow showed that the spread of the residuals is slightly higher for 5% GeH_4 than for 10% GeH_4. None of these error analyses shows a problem in the data. But. a plot of peak height vs. time reveals that the values continually increase with time. as is shown for Figure 5.13. which shows the intensity for three measurements at the same parameter settings. This is probably the key to the variability problem. because the 5% data were taken all together, and then at a later time. the 10% data were taken. This suggests splitting the 5% and 10% data into two blocks. This was done by splitting the 5% and 10% data into two separate 2^4 designs. When this was done. the same effects of power. pressure. and H_2 flow were seen. But because the data all came from the

same GeH₄ flow block. the fit of the linear model increased to 82%. The electron temperature data suggests that the lower GeH₄ flow rate is better in that the electron temperature is higher at the lower setting. In addition. previous research in growing germanium carbide materials. during the Master's research work. also indicated that a low flow rate of germane is desirable because the deposition rate of Ge is much higher than the deposition rate of C. Thus. it is necessary to limit the growth rate of Ge by limiting the reactants via a low gas flow. Based on this reasoning, all of the subsequent experiments involving Ge:C plasmas were done with a low GeH₄ flow rate.

5.3.2 Growth rate

The statistical analysis of growth rate revealed that the experiment had a standard error of ± 0.0102 Å/s. which is quite acceptable. The only significant single variable was power. and even the effect of changing power by itself was the smallest of the important variables. There were three significant two variable interactions and two three variable interactions. The more important of the two variable interactions was between power and pressure. The interactions between temperature and pressure and between power and CH₄ flow were also found to be important. Using these factors only explained 51% of the variability. and this is because the linear model is not very appropriate for this experiment. as will be explained below.

As the power was increased from 150 to 175 W. the growth rate increased from 0.15 to 0.21 Å/s. However. further increasing the power from 175 to 200 dropped the growth rate from 0.21 to 0.18 Å/s. These findings are shown in Figure 5.14. The initial increase is easily explained by an increase in electron temperature giving an increase in dissociated radicals. The slight decrease at the highest powers seems to indicate that either an increase in gas phase collisions. or an increase in in situ etching. leads to a decrease in growth rate. Because the effect is non-linear. a linear model does not fit these data very well. This also indicates that 175 watts is optimal for growth rate.

Because pressure shows up in so many of the two and three factor interactions. its singular effect was explored. Increasing the pressure from 7 to 10 mTorr increased the growth rate from 0.17 to 0.21 Å/s. a surprising increase. as shown in Figure 5.15. Raising
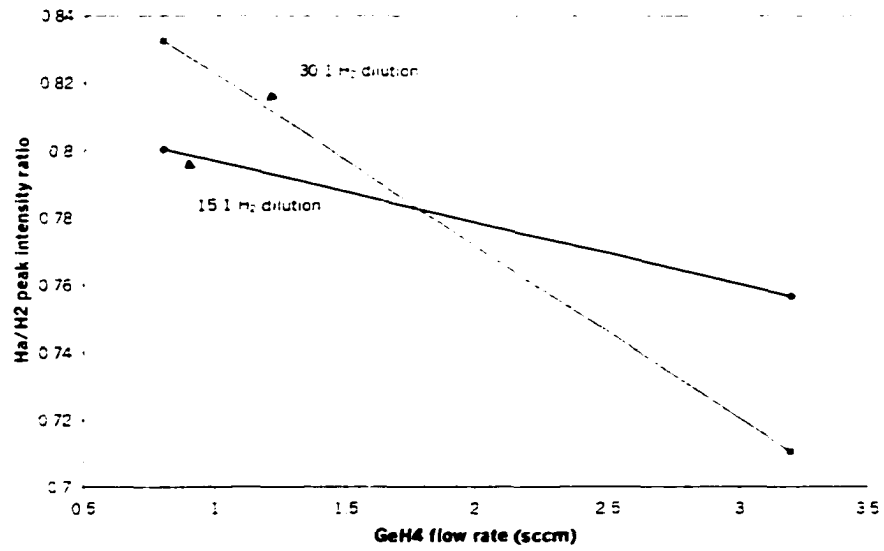
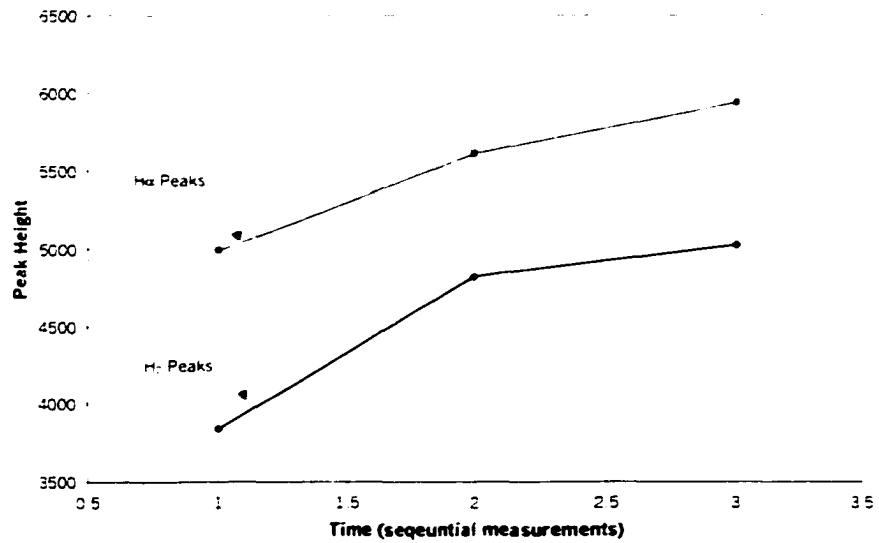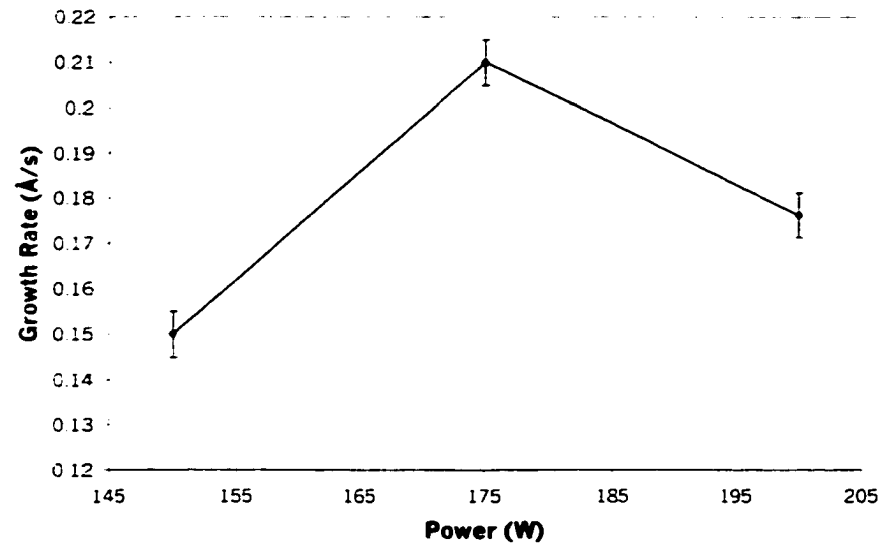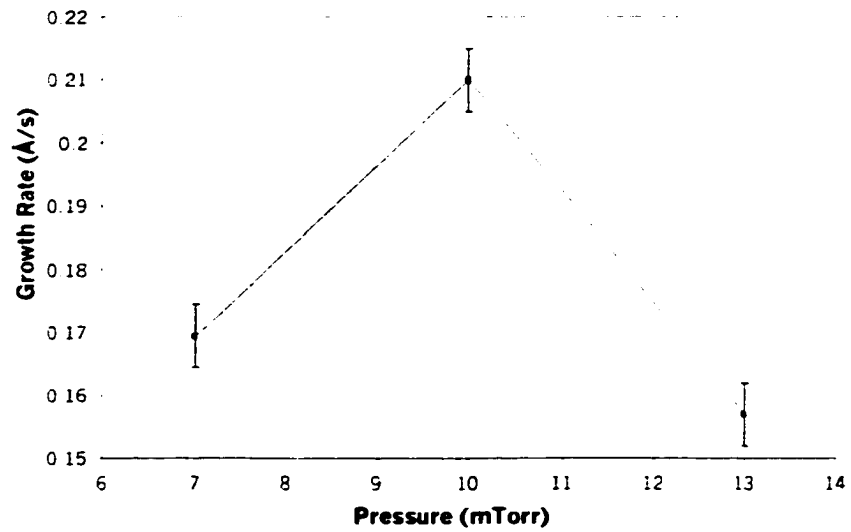**Figure 5.12: Two variable interaction between H₂ and GeH₄ flow.**

Figure 5.13: Peak height as a function of time.

Figure 5.14: Growth rate as a function of power.

Figure 5.15: Growth rate as a function of pressure.

the pressure from 10 to 13 mTorr decreased the growth rate from 0.21 to 0.16 Å/s, which is to be expected from the reduced mean free path of the radicals. The initial increase in growth rate as the pressure was raised is attributed to a decrease in substrate etching. Again, because these data are nonlinear, a quadratic model should be used to find an optimal pressure, which appears to be near 10 mTorr.

The two factor interaction between power and pressure is explained as follows. At lower pressures 150 W is better than 200 W. It is thought that at the lower pressure a lower power reduces the etching effects, which increases the growth rate. At higher pressures, however, 200 W is much better than 150 W, as 200W gives 0.22 Å/s and 150 W gives only 0.12 Å/s. This is attributed to the reduced mean free path at higher pressures being overcome by an increase in dissociated radicals. This two factor effect indicates then, that higher pressures severely limit mean free path, and this has a large affect on growth rate. But this problem can be overcome with higher powers.

The two factor interaction between power and CH_4 flow is explained as follows. At high methane flow rates, there is little difference between the growth rates achieved at either 150 or 200 W, although 150 W is slightly better. This is thought to be because gas phase collisions lower the growth rate, and the lower power setting reduces these collisions. At lower methane settings however, 200 W is much better, as 200 W gives a growth rate of 0.21 Å/s and 150 W only gives 0.14 Å/s. This is attributed to the fact that at low CH_4 flow rates, gas phase collisions are not as problematic, and hence, the higher power produces more radicals.

The two factor interaction between temperature and pressure showed that at high pressures, temperature made virtually no difference, as would be expected. However, at low pressures, 350° C gave a growth rate of 0.23 Å/s while 550° C gave only 0.14 Å/s. This surprising result is thought to occur because at the higher temperatures, Ge and C are more likely to phase separate to some degree. The resulting graphite that precipitates out of the alloy is etched away very efficiently at the lower pressures.

5.3.3 Atomic percent substitutional carbon

The next set of experiments that were done dealt with the amount of substitutional carbon in the films. Three important criteria about these experiments should be pointed out.

First. the values presented here refer only to XPS data that corresponds to alloyed C. which gives an XPS peak of 283 eV. Any other XPS data. the peaks that correspond to interstitial carbon. carbon-carbon clusters or hydrocarbon contamination. are not reported in the following discussion. Secondly. a thin oxide layer was etched from the surface of the film before the measurements were taken. by an Ar ion beam in vacuum. This allowed the bulk C content to be determined as opposed to a surface concentration. Finally. under certain conditions the desired two dimensional growth model was destroyed. Under these conditions. the film grew in disconnected columns. A representative SEM cross section of this type of film morphology is shown in Figure 5.16. As can be seen. the film starts to grow by 2-D layers for approximately 700 Å and then degenerates into the disconnected column growth. It is believed that these columns start to grow at sparsely separated nucleation sites. As growth begins on these sites. the strain caused by the incorporation of C in the material is relieved by increasing the surface area of the grain. The surface area is increased by growth perpendicular to the growth surface. If this process were undisturbed the grain would grow as a sphere. thus minimizing the total energy of the structure. However. more material is deposited as the grain grows and this leads to a column growth. Careful examination of the SEM picture shows that the width of the column reduces toward the top. indicating that as growth proceeds. the grain is trying to produce a sphere. It was generally found that lower temperatures. higher powers and higher H_2 flow reduced the tendency of 3-D growth. It is believed that the lower temperatures reduce the surface diffusion energy of the deposited material and hence. it is not able to rearrange itself into the strain-reducing column structure. From the experiments of germanium carbide films on Si wafers it was found that higher powers and higher H_2 flow increased the number of grains, as will be discussed below. Under these conditions the grains are closer together and are not separated enough to degenerate into the column growth. It was also found that the column structure of these films resulted in very high C contents. up to 15 atomic percent. However. it is believed that the increased surface area of the disconnected columns allowed for a high surface concentration of C at defect sites on the surface of the column. Hence. the results from these samples do not represent true alloyed C values and so none of the films that had this structure were used in the following results.

The statistical analysis of the XPS data showed the experiment had a standard error of ±0.15 atomic percent. which is moderately high. The error is most likely due to inaccuracy of measuring low levels of C. and due to the fact the above mentioned 3-D films were thrown out even though the parameters they were grown with may have produced some alloyed C if the film had not grown with columnar structure. Additionally. if a peak was centered on a value other than 283 eV. the C value was set to zero. So a 283 eV shoulder was not considered. because no peak shape analysis software was available for the data. Analysis of the data showed that ten two. three and four variable interactions involving power. H_2 dilution. CH_4 dilution. and temperature were significant. Using these effects in a linear model explained only 61% of the variability. The reason for the inadequacy of the linear model is the moderately high standard error.
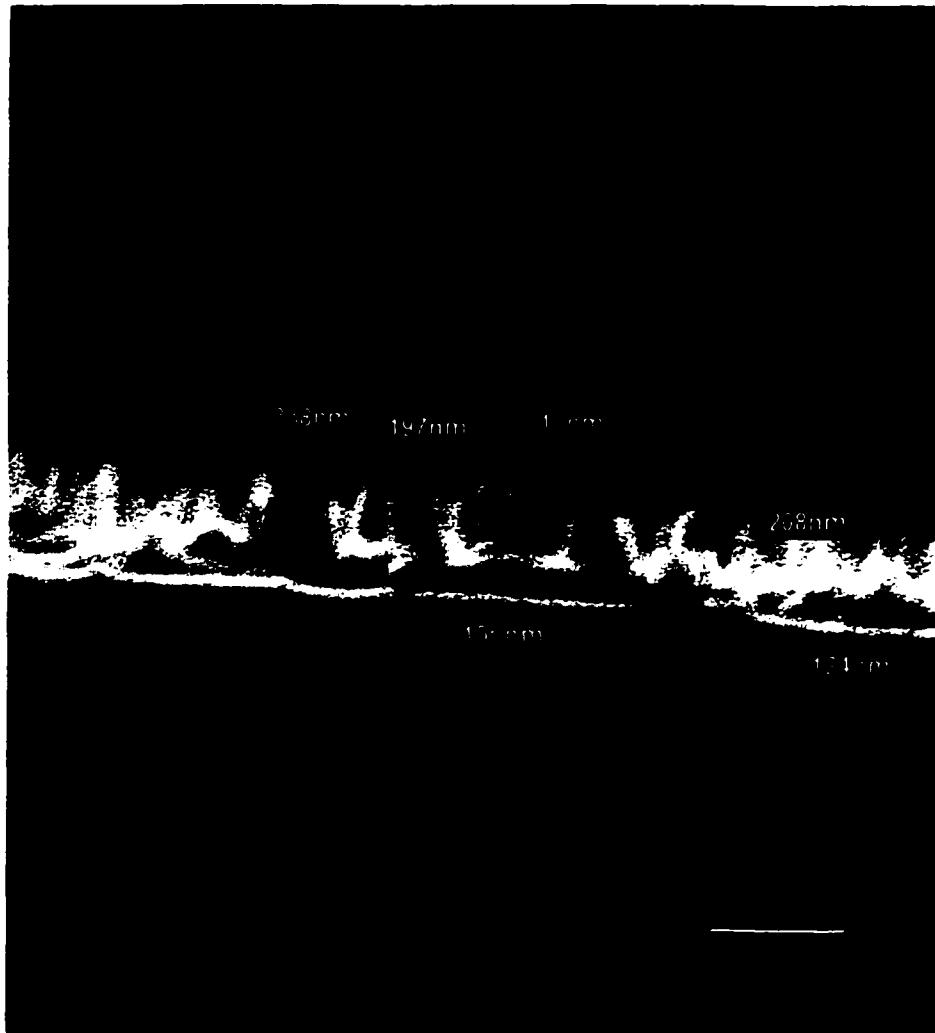
The power and temperature interaction showed that at low temperatures. 200 W produces more alloyed C. but at high temperatures. 150 W produces much more. This result is shown in Figure 5.17. The probable reason for this result is that at low temperatures. Ge and C do not phase separate. and so the higher power deposits more C on the surface for incorporation. But at high temperatures. the Ge and C are more likely to phase separate. which will lead to isolated C atoms on the surface of the film. At high power settings. these atoms are etched away at an extremely high rate. At the lower power. they are not etched away as quickly. and there is a possibility that subsequent layer growth may incorporate the C atoms that are present on the growth surface.

The H_2 dilution and methane interaction revealed that at high CH_4 flow. higher H_2 dilution produces more alloyed carbon. as can be seen in Figure 5.18. But at low CH_4 flow. H_2 dilution is not very important. In the OES experiment it was shown that higher H_2 flows produced a higher $H_\alpha{:}H_2$ ratio. Thus. there are more H ions available to break apart the CH_4 molecules. Apparently at low CH_4. enough H ions exist to break apart all of the methane even at the low H_2 flow setting. But at high CH_4 flow there are more CH_4 molecules available and so an increase in H ions is required to dissociate all of them. Breaking all of the methane molecules then results in more C in the films.

The power and CH_4 interaction is explained as follows. At low CH_4 flow, power is not important. But at high CH_4 flow. a lower power setting produces more carbon in the film. This result can be seen in Figure 5.19. This interaction can be explained using a

concept that was discussed under the power and temperature interaction. For this interaction, when the flow rate of methane is high, more C atoms and graphite will exist on the growth surface. If the atoms remain on the surface as a new layer is deposited, there is a chance that they will be incorporated into the film. However, at the high power setting, all of this material is etched away before it has a chance to incorporate itself into the new layer. Since this idea has been supported by two interactions, its validity is strongly reinforced.

Figure 5.16: Three dimensional film morphology.
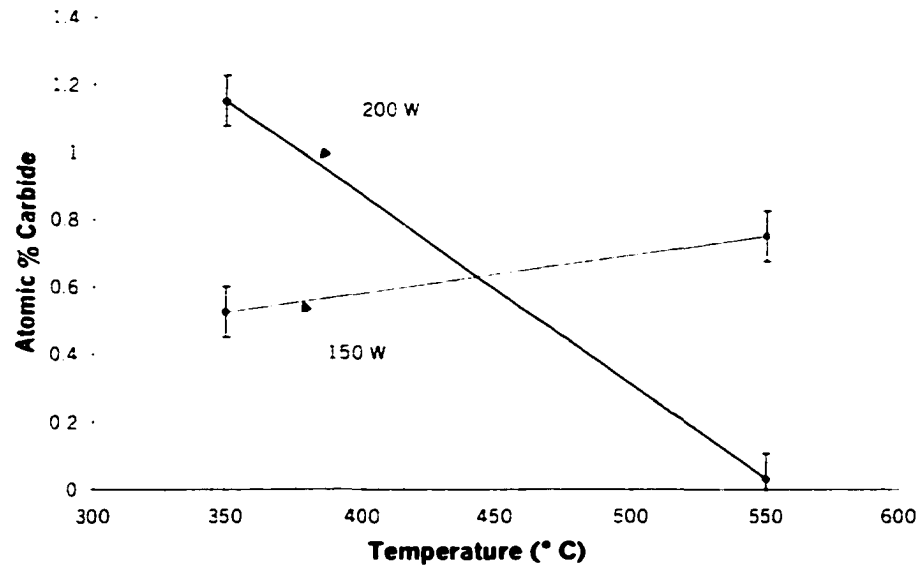
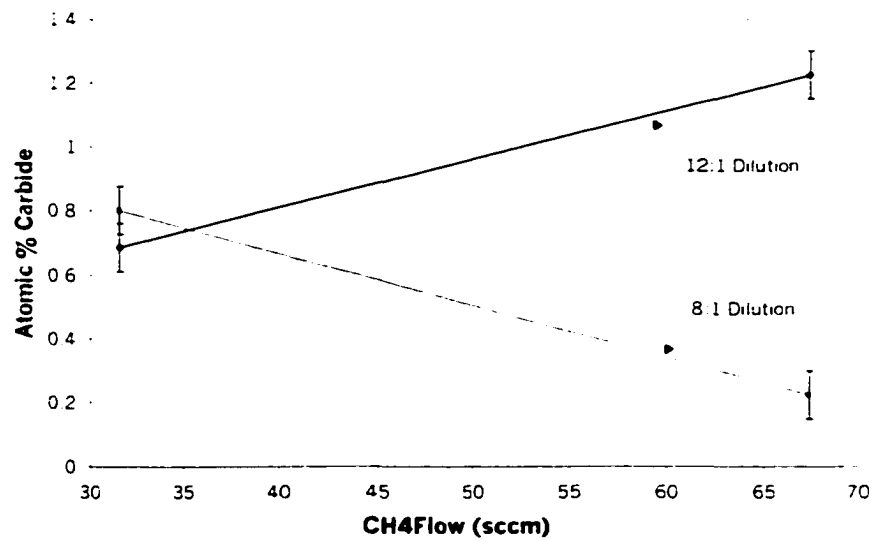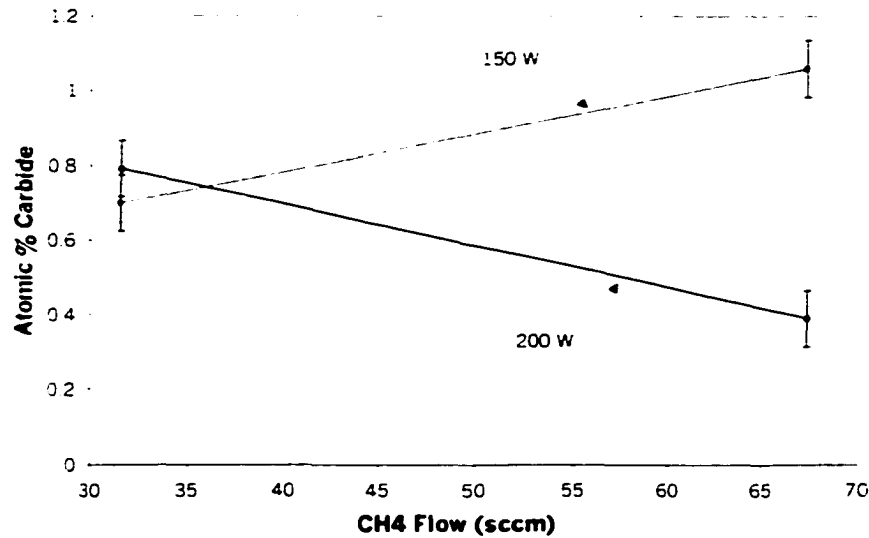**Figure 5.17: Two variable interaction between power and temperature.**

Figure 5.18: Two variable interaction between H₂ dilution and CH₄ flow.

1.2

150 W

1

0.8

Atomic % Carbide

0.6

0.4

200 W

0.2

0

30   35   40   45   50   55   60   65   70

CH4 Flow (sccm)

Figure 5.19: Two variable interaction between power and CH₄ flow.

The temperature and CH₄ flow interaction showed that at low CH₄ flow. lower temperatures result in more C in the films while at high CH₄ flow. higher temperatures are better. although there is not a great difference. These findings are shown in Figure 5.20. Based on the above temperature result that indicated that phase separation occurs at the high temperature setting. this data suggests Ge and C do not phase separate at the lower temperatures. On the other hand. when the flow of CH₄ is high. more C atoms and graphite will be present on the surface. as was suggested previously. In this case higher temperatures allow these atoms to diffuse along the surface. which increases the chance that they will become incorporated. This benefit of higher temperatures seems to offset the loss of C due to phase separation at the high methane flow setting.

Based on the linear model constructed for this data. the amount of substitutional carbon in the films was maximized. In general it was found that the C content could be optimized by decreasing the etching of the plasma and by increasing the surface diffusional energy of the deposited species up to a point. Decreasing the etching was accomplished by decreasing the H₂ dilution to approximately 5:1. increasing the plasma pressure to 15 mTorr and decreasing the plasma power to 100 W. Increasing the surface diffusional energy of the deposited species was accomplished by raising the deposition temperature to 450° C. Raising the temperature further introduced the unwanted effects of phase separation of the

Ge and C. or the degenerative 3-D column growth described above. It is believed that lowering the degree of etching keeps C atoms from being etched away from the surface before they can be incorporated. and the higher surface diffusional energy allows the species to orient them into a lattice position. Because the Ge and C have such a different bonding structure. more energy is required for them to form bonds. And indeed. the bond disassociation energy for the Ge-C bond is higher than the Ge-Ge bond.[53] But the C-C bond is a stronger bond than the Ge-C bond. so if the substrate temperature is not raised too much. the C-C bonds will not form on the surface. Using these parameters. the highest carbon content achieved was 4.8 atomic percent. which is an improvement of approximately 20% over the factorial experiment.
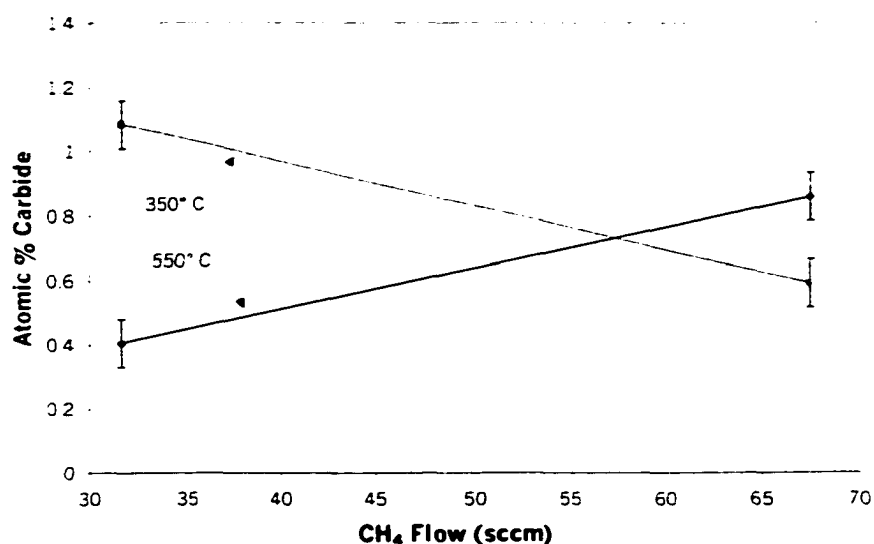
Figure 5.20: Two variable interaction between temperature and CH₄ flow.

5.3.4 Raman crystal structure

The statistical analysis on the Raman data showed that the experiment had a standard error of ±0.4 cm^{-1}. The error is attributed to the weak Raman signal that was obtained. as the FWHM was difficult to accurately measure on the small peaks. The most important effects on the width of the Raman peak were a two variable interaction between power and temperature. and a two variable interaction between pressure and CH₄ flow. Using these

factors explained only 58% of the variability using a linear model. Because so little of the variability of the experiment could be explained with the linear model, the most significant of the single variables. H_2 dilution. CH_4 flow and power, were investigated. It was found that these factors were very linear. Hence, it is believed that the low fit of the linear model is attributed to the error in collecting the measurements.

The analysis of the single parameters. H_2 dilution. CH_4 flow and power, was as follows. The H_2 dilution was found to be the most significant of the single variables, but its effect was still small as compared to the two variable interactions. The trend of adjusting the H_2 was found to have the same effect as was found in the Ge on silicon wafer experiment. In both cases, increasing the H_2 dilution sharpened the Raman peaks. As the methane flow was increased from 31.6 to 67.4 sccm the FWHM decreased from 7.4 to 6.5 cm^{-1}, as can be seen in Figure 5.21. Although this is a moderate decrease, it is surprising that the FWHM was reduced at all. This effect is attributed to slower growth rates at higher CH_4 flows. Slower growth rates arise because of the associated reduction in electron temperature. A slow growth rate improves the crystal structure of the film by giving time for deposited species to migrate about the growth surface and insert themselves into proper lattice sites. In addition, there is more time for the etching benefits of the plasma to act upon the growth surface. Finally, as the power was increased from 150 to 200 W, the FWHM was reduced from 7.2 to 6.7 cm^{-1}. This result is shown in Figure 5.22. This small effect is attributed to increased etching at the higher powers. As can be seen in both figures, the data is extremely linear.

The most significant two variable interaction was between power and temperature, and the result is shown in Figure 5.23. At 350° C, the power had little effect on the Raman peak width. But at 550° C, the 200 W FWHM was only very slightly higher, while the 150 W FWHM increased by nearly 35%. It is believed that at 550° C, the Ge and C begin to phase separate, which leads to decreased crystallinity because of the associated distortion of the lattice. At higher powers, all of the distorted non-crystalline material is etched away. But at the lower power setting, not all of the non-crystalline material is etched away and hence, the FWHM of the material is larger. This idea is consistent with the above data.

The next most significant two factor effect was between pressure and CH_4 flow rate, and the results are shown in Figure 5.24. At the lower CH_4 setting, the pressure made no difference. But at the higher methane flow, lowering the pressure from 7 to 13 mTorr

reduced the FWHM from 7.6 to 5.5 cm^{-1}. This effect is attributed to the fact that at higher methane flow rates and at lower pressures. the growth rate is slower. The slow growth rate results in more crystalline material. because the deposited species have more time to fit themselves into proper lattice positions before subsequent growth occurs.
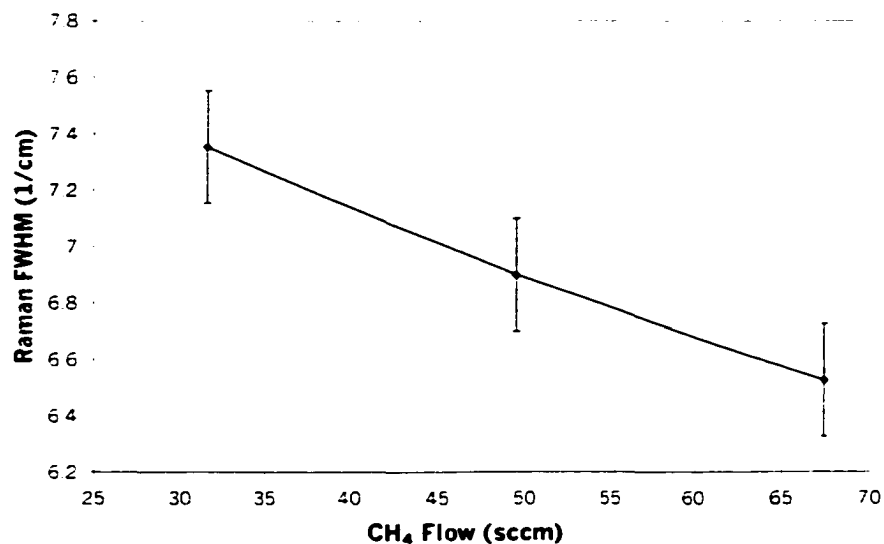
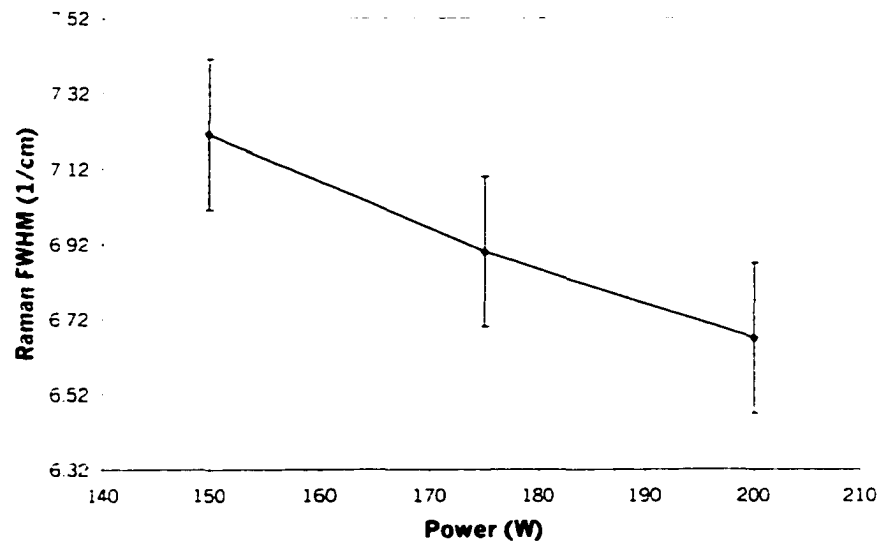Figure 5.21: Raman peak width as a function of CH₄ flow.

An attempt was made to minimize the Raman peak width value using the linear model that was constructed for this data. Unfortunately. as was the case for the Ge on Si data. the Raman FWHM value could not be decreased significantly from the factorial experiment values. Again. it can be assumed the low fit of the linear model to the data. which is attributed to the error in collecting the data. is the reason the predicted values model did not succeed in optimizing the FWHM values. In other words. since the linear model did not fit the data very well. the optimization process that used the linear model to minimize the FWHM did not work very well either.

5.3.5 XRD grain size

The next set of experiments were concerned with the XRD grain size and structure of the films. The statistical analysis revealed the experiment had a standard error of 54 Å. which is relatively high. The high error is attributed to the inherent inaccuracy of Schreer's

formula. which is especially inaccurate for a large grain size. The most important variables were found to be power. temperature and a two variable interaction between power and CH_4 flow. There were also the slightly less significant effects of a two variable interaction between H_2 dilution and CH_4 flow and a two variable interaction between power and pressure. Using these effects in addition to the three and four variable effects that were also found in a linear model explains about 70% of the variability. It is believed that the error in the experiment and the non-linearity in some of the factors limited the fit of the linear model.

As power was increased from 150 to 175 W. the grain size reduced from 607 to 512 Å. as can be seen in Figure 5.25. Increasing further to 200 W increased the grain size again to 587 Å. The smaller grain size at higher powers is attributed to increased plasma damage of the growth surface. which resulted in more nucleation points during growth. A possible reason for the increase in grain size at 200 W is that the gas phase molecules are broken down more completely to Ge or GeH. and these incorporate into existing. H passivated grains easier. Another possible reason for the grain size increase at the highest power setting is that the growth rate is slower at the highest power setting. and this gives the grains sufficient time to coalesce before the next layer is deposited.

Figure 5.22: Raman peak width as a function of power.
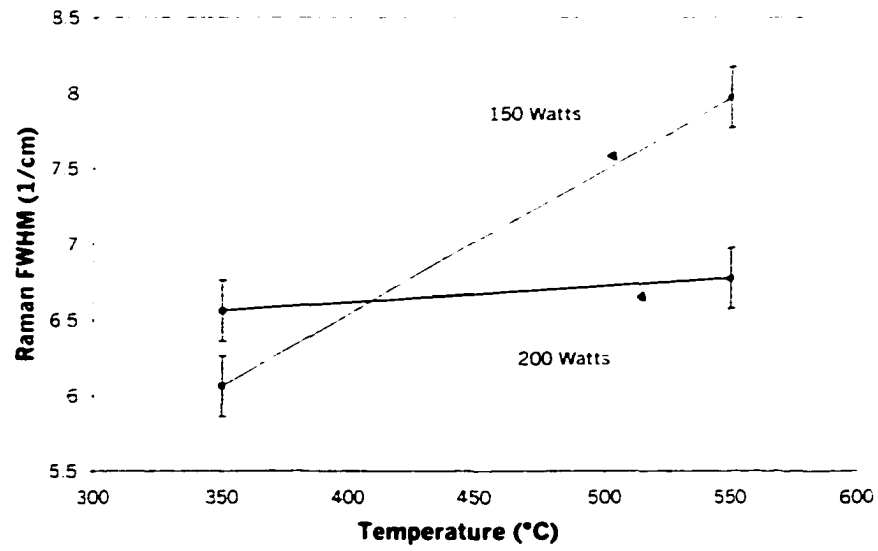
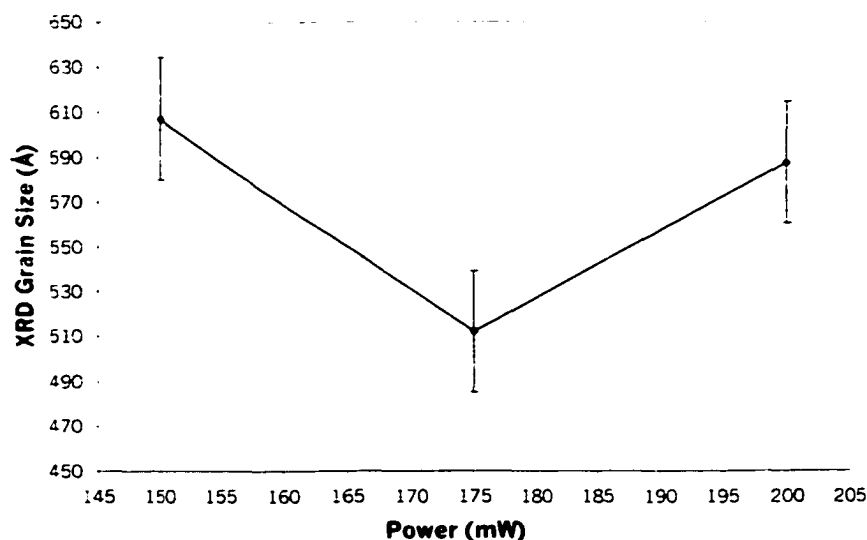**Figure 5.23: Interaction between power and temperature.**
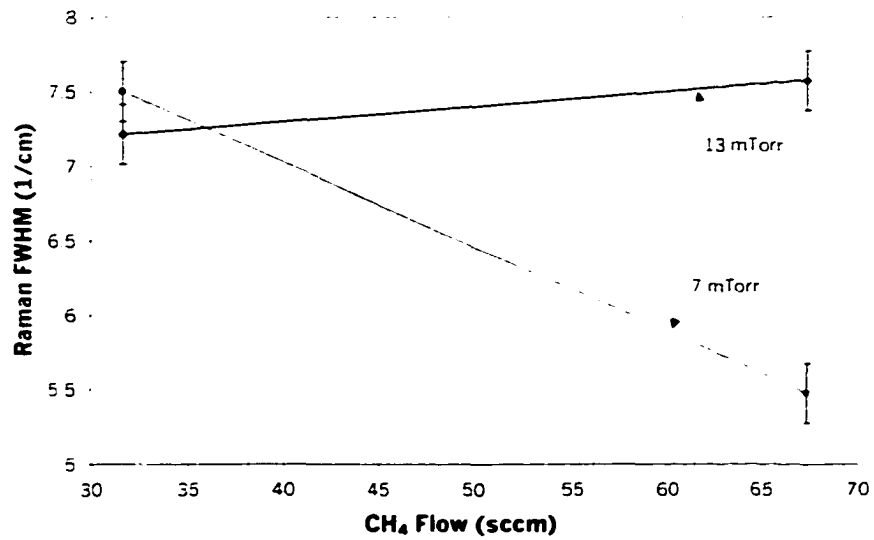
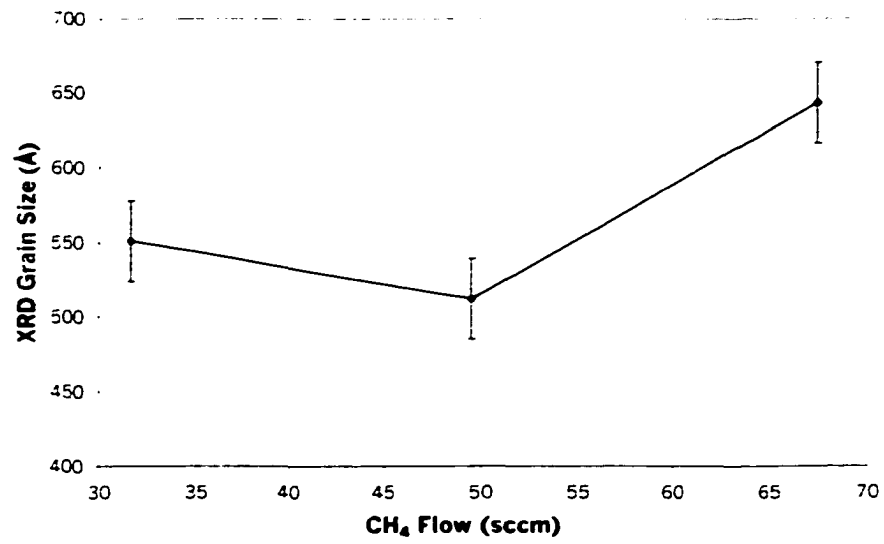**Figure 5.24: Interaction between pressure and CH₄ rate.**

As CH_4 flow was increased from 31.6 to 49.5 sccm. the grain size slightly reduced from 551 to 512 Å. although this is nearly enclosed by the error margin. Increasing the CH_4 flow to 67.4 sccm increased the grain size to 643 Å. The data is shown in Figure 5.26. This is attributed to a reduced growth rate at higher CH_4 flows. which allows grains to coalesce before another layer is deposited on them.

As temperature was increased from 350 to 450° C. essentially no change occurred. But when the temperature was raised to 550° C. the grain size increased from 512 Å to 701 Å. as can be seen in Figure 5.27. This is attributed to grain coalescence.

A two variable between H_2 dilution and CH_4 flow was found to be significant. as can be seen in Figure 5.28. At low CH_4 flow. the dilution is not very important. But at high CH_4 flow. a lower H_2 dilution produces grains of 826 Å. as opposed to 461 Å at the high H_2 setting. This can be explained by considering that at low H_2 flow the plasma damage is reduced. The contribution of methane flow can be thought of in two ways. First. a high CH_4 flow results in a slow growth rate. which helps the coalescence of grains. Secondly. the reduced electron temperature that is caused by the high CH_4 flow will help to minimize the plasma damage. So the combination of low H_2 flow and reduced electron temperature at high CH_4 flow together greatly reduce the damage to the growth surface by the plasma. This significantly reduces the number of nucleation sites and results in a larger grain size.

**Figure 5.25: Grain size as a function of power.**

Figure 5.26: Grain size as a function of CH₄ flow.
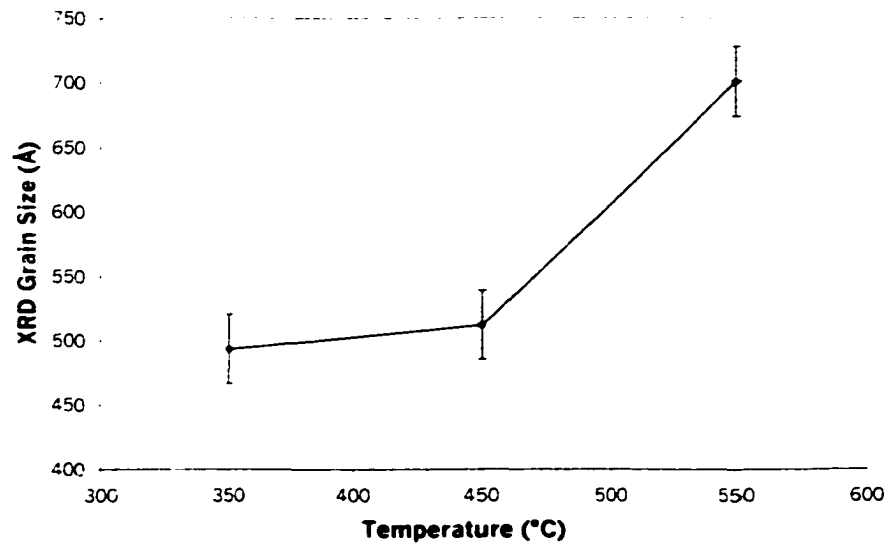


Figure 5.27: Grain size as a function of temperature.

A two variable interaction between power and CH_4 flow was found to be important, as can be seen in Figure 5.29. At low CH_4 flow, 200 W gives nearly twice as large of grains as 150 W. while at high CH_4 flow, exactly the opposite is true. The low CH_4 flow phenomena can be explained the same as the above single factor case for power. But at high CH_4 flows, gas phase collisions become more important. These collisions create higher order gas phase molecules, which do not incorporate into existing grains easily, and hence, it is more likely for more small grains to grow.
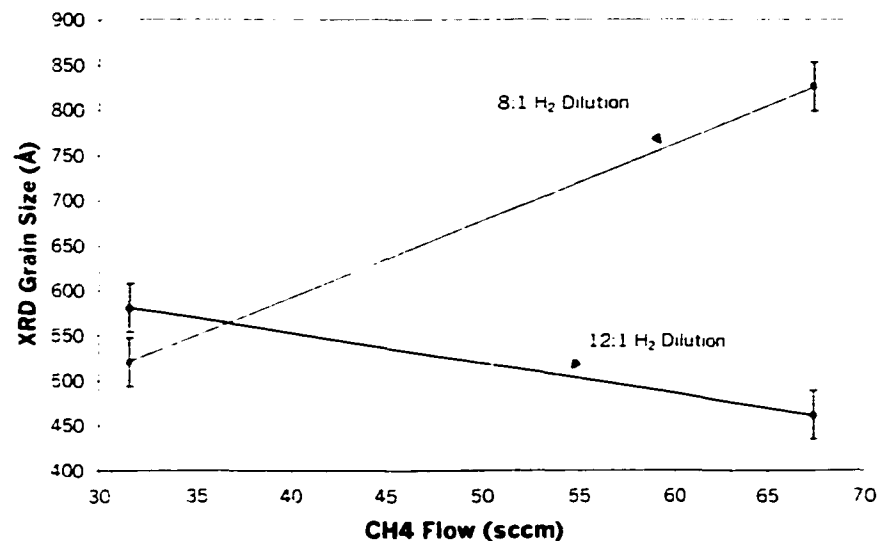
Figure 5.28: Interaction between CH_4 flow and H_2 dilution.

The predicted values model that was constructed for the grain size data was used to maximize the grain size of the films. For this process, regions of parameter space that optimized the grains, while at the same time produced an appreciable carbon content, were explored. The samples that produced the best grain size were achieved with a temperature of 350° C, a pressure of 13 mTorr, a CH_4 setting of 6.8 sccm, an increased power setting of 225 W, and an increased H_2 dilution of 15:1. It was very surprising that a higher power and H_2 flow setting were beneficial to larger grains, as this is the opposite result that was found for the Ge on Si data. It must be concluded then that the presence of methane molecules in the

plasma sufficiently reduces the electron temperature as to reduce the damage done by the plasma. Using these parameters produced films with a grain size of 0.52 μm and a atomic percent C content of approximately 3%. This is a grain size that is roughly double that of any grain size from the factorial experiment.
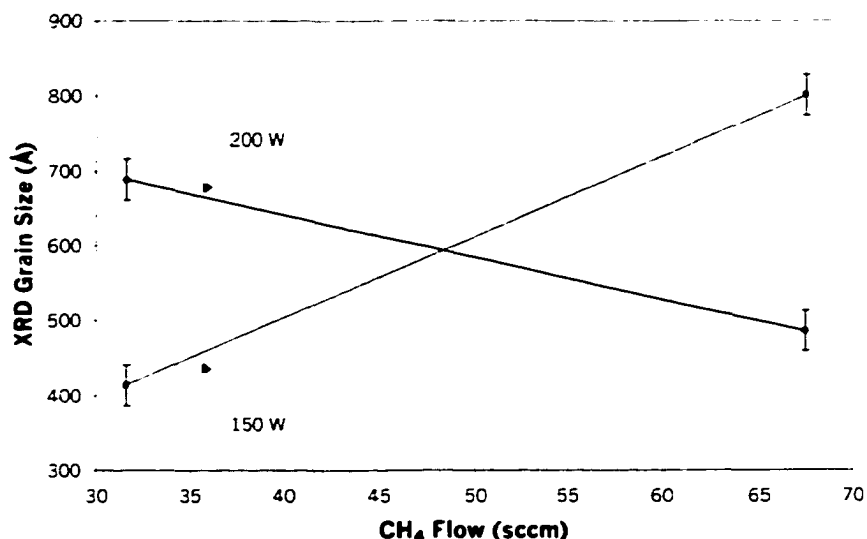

Figure 5.29: Interaction between CH₄ flow and power.

5.3.6 Bandgap

The next experiment for the germanium carbide samples on silicon was to investigate how the bandgap varied. The same factorial experimental design as above was used for this data. and the important effects were determined. By careful examination of the data. however. it was realized that most of the important effects were the same as those effects that produced more C in the films. The only two exceptions to this were a pair of two variable interactions. which included power. pressure. and CH₄ flow. These effects seemed to effect the crystallinity of the samples. as the interactions could be matched to effects from earlier Raman and XRD data. It is assumed then that the compensations for reduced grain size and increased Raman FWHM that were discussed in the Ge data did not fully account for an increase in bandgap from poorer crystal quality.

To determine the effect of C content on the bandgap. a plot of atomic percent carbide versus the Tauc and E_{04} bandgap estimations was constructed. as shown in Figure 5.30. As can be seen. the Tauc bandgap increases by approximately 21 meV per percent alloyed C.

while the E_{04} bandgap increases by approximately 28 meV per percent C. It should be noted that these bandgap values have been corrected for the effects of grain size and Raman FWHM. as was described earlier in the Ge films on Si data. This correction proved to be very important because the increase rates before the correction were as high as 50 meV per atomic percent C. In the introduction to this dissertation it was noted that Orner and co-workers predicted an increase in bandgap of approximately 30 meV per percent alloyed C. The data collected in this experiment underestimates the increase in bandgap by approximately 18%. The source of this disagreement may lay in the fact that Orner predicted the primary indirect gap to shift from being centered at the L point to being centered along the Δ line. because the bandgap does not increase as fast along the Δ line as it does at the L point. Hence. it is possible that the bandgap increase is more rapid while it is centered at the L point. and then slows down as the shift to the Δ line occurs. The average increase over the entire region. then. is at a slower pace than what was predicted for the L point. Another reason for the disagreement lies in the fact that Orner et al.. did not account for strain in their calculations. Because these films were not perfectly lattice matched to the Si wafer. they are significantly strained. Since strain acts to reduce the bandgap. the internal strain of the films caused the bandgap to increase at a slower rate than what was predicted by Orner. This idea is reinforced by the fact that the bandgap increased at a faster rate in the samples that had a large C concentration. where the strain is relieved the most.
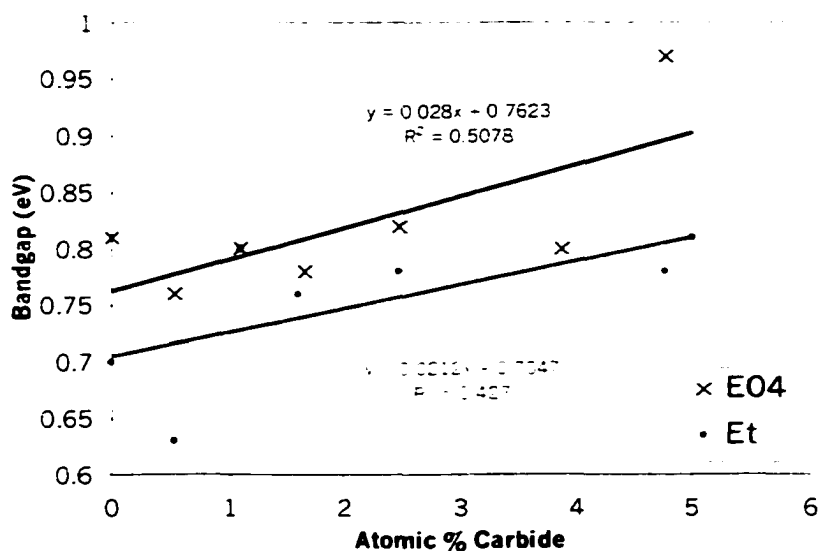
Figure 5.30: Bandgap as a function of alloyed C content.

The bandgap data shown in Figure 5.30 have a maximum of approximately 1 eV for the E_{04} data and approximately 0.8 eV for the Tauc data. Thus. when the C content approaches 4.5 to 5 atomic percent. the bandgap of the material approaches that of Si. This is a very important result as it shows that Ge:C has a much more useable bandgap than pure Ge. In other words. thermal noise would be much less of a problem with Ge:C as it would with pure Ge.
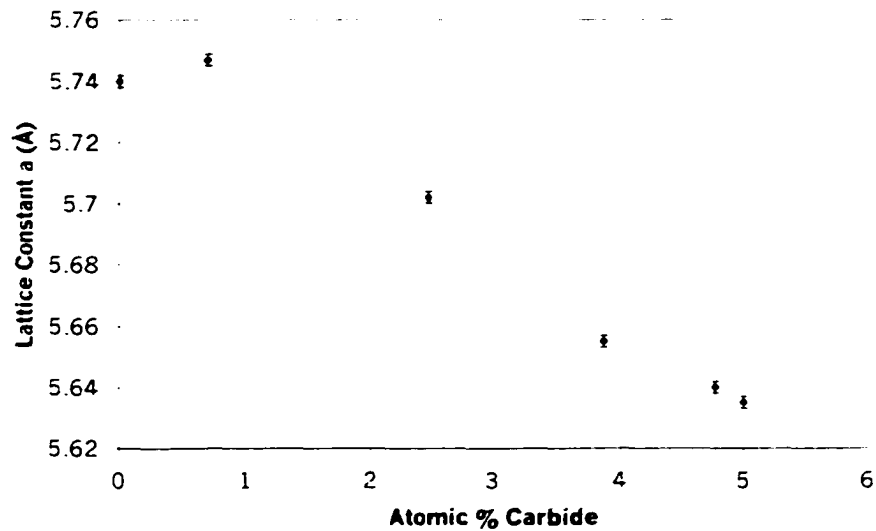
5.3.7 Lattice constant

Similar to the bandgap data. the change in the lattice constant a in the samples was investigated. Again. similar to the bandgap data. a factorial experiment was done. but all of the effects that changed the lattice constant significantly were effects that also increased the atomic percent of substitutional C. The results are shown in Figure 5.31. The value for the pure Ge sample has a lattice constant which is approximately 0.1 Å larger than the value for bulk Ge. As was mentioned in the chapter on characterization. the reason for the higher values is the strain of growing a thin film on a dissimilar substrate. However it is unclear as to why there is an initial increase in the lattice constant once trace amounts of carbon are introduced. A possible reason may be that the sporadic incorporation of trace amounts of C in the Ge lattice causes distortions in the lattice. which ultimately result in an increase in the lattice constant. Beyond the initial increase there is a linear decrease in the lattice constant of 0.0266 Å per atomic percent alloyed C. At this rate. the carbon would compensate for the mismatch between Ge and Si when approximately 8 atomic percent C had been incorporated. This is less than the Vegard's law prediction of approximately 10 atomic percent. The discrepancy is most likely due to the inaccuracy of Vegard's law as applied to this situation.

5.3.8 Conductivity and mobility of intrinsic films

Electrical measurements were also made on the Ge:C films to determine how the material properties affected carrier transport. Conductivity measurements were made on the films. and the affect of alloyed C was investigated. The results are shown in Figure 5.32. As can be seen. there is an initial dramatic increase in the conductivity. This is most likely due to a decrease in the growth rate. as does accompany an increase in C content. which allows more time for unintentional dopants to insert themselves into the material as it grows. At

high C content, the conductivity begins to drop off. This is most likely due to a degradation of the electrical properties because of the presence of C in the lattice.

Mobility measurements were also made on the germanium carbide samples. The films had an average mobility value of approximately 70 $cm^2/V \cdot s$, which is a reduction of 96% from the pure Ge samples. The large decrease in mobility is attributed to the presence of C in the Ge lattice. Due to the large difference in bond length between Ge-Ge and Ge-C bonds, the C atoms distort the Ge lattice. The distorted positions where the C atoms exist will then serve as scattering sites for conducting electrons. The increase in scattering sites tends to lower the mobility of the carriers. This can potentially be a significant problem with the material system, because one of the reasons for using germanium based materials is that they have a larger mobility than silicon based materials. This may be an indication that it would be better to use germanium carbide as a buffer material upon which to grow pure Ge. The buffer layer could allow lattice matching and the pure Ge layer would then allow for high mobility.

Figure 5.31: The lattice constant a as a function of alloyed C content.
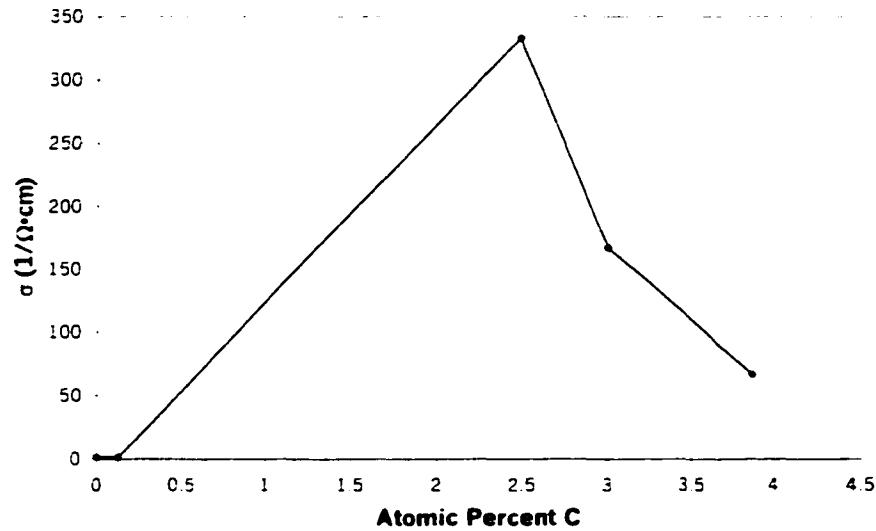
Figure 5.32: Conductivity as a function of alloyed C content.

5.3.9 Doped films

Because it was desired to use the films in diode structures. experiments were performed in doping the films both n and p type. A set of deposition parameters that produced films with a Raman FWHM of 5.2 cm^{-1}. a grain size of 686 Å. and a C content of 2.5 atomic percent was used as a control set of parameters. The films produced from these parameters were measured for conductivity. Next. experimental films were grown where phosphine gas was added for n type films. or diborane was added for p type films. The results are shown in Figure 5.33. In the figure. positive sccm values refer to PH_3 flow and negative sccm values refer to B_2H_6 flow. As can be seen. with no dopant gas flowing. the conductivity of the film is approximately 330 1/Ω•cm. This corresponds to an n-type impurity concentration of approximately 2 E 18 cm^{-3}. The reason for this extremely high unintentional doping level is that the growth rate of the films is extremely slow. This allows a great deal of time for impurities to incorporate themselves into the lattice as the films grow. The source of the contamination is the air in the lab room and the imperfect vacuum of the reactor. contamination of counter surfaces where the samples are loaded. and oxygen contamination that is produced by etching from the quartz window of the reactor. This result suggests that in order to grow pure $Ge_{1-x}C_x$. an extremely clean environment is required. unless a higher growth rate can be achieved for the films. As PH_3 is added to the films. the conductivity increases up to a value of approximately 5.000 1/Ω•cm. which corresponds to

an impurity concentration of approximately 1 E 20 cm^{-3}. The conductivity saturates at this level. and this is due either to an inability of the plasma to produce any more P radicals or it is due to an inability of the material to make any more P atoms electrically active. As B_2H_6 is added to the plasma the conductivity drops down to a value of approximately 1.7 1/Ω•cm at a diborane flow rate of 10 sccm. It is believed that this amount of B in the lattice is enough to compensate for the n type impurities and this makes the conductivity closer to that of intrinsic Ge. This conductivity value corresponds to an impurity concentration of 7 E 14 cm^{-3}. As more B_2H_6 is added. the conductivity increases as the film becomes p type. The maximum p type conductivity is only 218 1/Ω•cm. which corresponds to an impurity level of 3 E 18 cm^{-3}. The reason that a higher p type conductivity could not be achieved is most likely the fact that the film is highly doped n type automatically due to contamination.
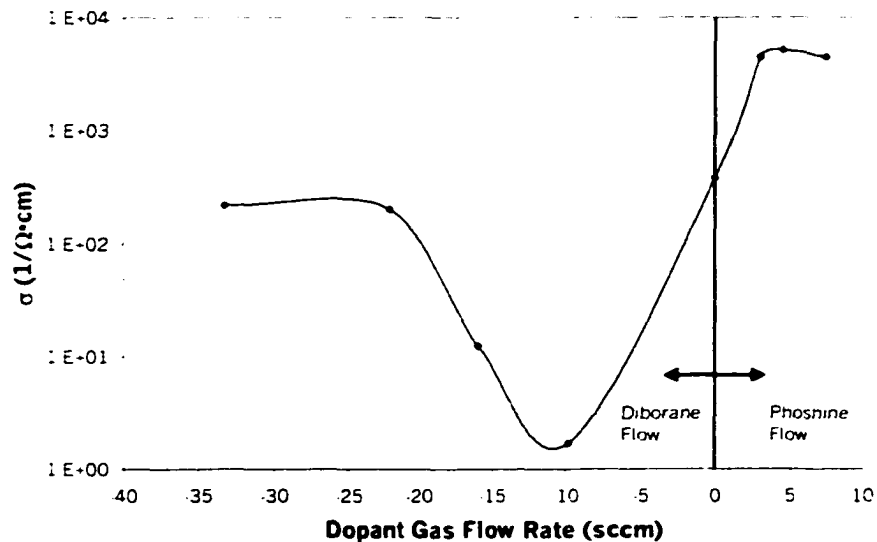
Figure 5.33: Conductivity as a function of dopant gas flow. Positive sccm refer to PH_3 flow and negative sccm refer to B_2H_6 flow.

It was originally assumed that adding P to the $Ge_{1-x}C_x$ lattice would improve the grain size of the material. It was thought that. because the size of P is between that of Ge and C. it would help to alleviate some of the strain caused by the lattice mismatch between Ge and C. However. it was found that the grain size of the n type films was reduced by more than 60%.

Hence. it must be assumed that the added substitutional atoms only serve to further distort the Ge lattice.

OES of the plasmas containing phosphine and diborane was done such that cross contamination between the gasses could be monitored. It was found that cross contamination was a significant problem when switching from an n type dopant to a p type dopant. Etching and depositing cleaning layers on the chamber walls between dissimilar dopant plasmas did very little to reduce the cross contamination. It was found instead that in order to minimize cross contamination. a ten minute evacuation of the dopant manifold. followed by 40 Ar purges of the dopant manifold. followed by a 45 minute evacuation of the dopant manifold was needed to eliminate cross contamination of the dopant gasses. The reason that such an extreme purge and evacuate procedure is required. it is believed. is that the dopant manifold contains a section of flexible tubing. This tubing has ˙accordion˙ baffles in it. which undoubtedly trap gas. and make full evacuation of the flexible tubing very difficult.

5.4 $Ge_{1-x}C_x$ Films on Ge Substrates

The next set of experiments involved growing Ge:C films on Ge wafers. As was mentioned in the section discussing Ge films on Ge wafers. the Ge wafers give a Ge [400] peak that is centered approximately 6° lower than the true value of [400] for germanium. and the peaks are quite broad indicating a lack of correct alignment. Adding 6° 2Θ to the measurements gives a lattice parameter a of 5.694Å. which was verified by several wafer measurements. This then is taken as the standard a for Ge.

The XRD spectra of the $Ge_{1-x}C_x$ films grown on Ge wafers showed the small broad peak for the wafer and then a small unresolved peak for the film. The peak analysis software was used to resolve the two peaks by fitting a Pearson function to the two peaks. Doing so allowed a determination of the a of the material. which was found to be 5.518 Å.

For the sake of comparison. a sample was grown on a Si wafer that had the same parameters as the $Ge_{1-x}C_x$ on Ge sample. XRD was used on this sample to determine an a of 5.695 Å. which is very close to the pure Ge value. The films also had a germanium carbide [002] peak which gave an a of 5.684 Å. which would normally indicate the film had just a

trace of C. However, the XPS data determined the film had approximately 3 atomic percent C incorporated. So, when the film was deposited on Si it had a lattice constant equal to germanium's lattice constant and so it was totally relaxed. But when the film was deposited on Ge it had a much lower lattice constant, indicating that it was not relaxed and that it had a substantial amount of alloyed C. This would seem to suggest that when the film was deposited on Si the lattice mismatch strain caused total relaxation of the film and so the lattice constant is skewed. But when the film is deposited on Ge the film is strained due to the presence of C in the film, but it does not relax, and grows very thick in a strained state.

Also, the lattice constant of the film on the Ge wafer is quite close to that of Si. This would lead one to expect that the film could grow on Si without relaxation. But since the film that was deposited on the Si was totally relaxed, it may be assumed that the initial growth layer is mostly Ge, which is greatly strained, and therefore it relaxes. The initial relaxed layer serves as a template for subsequent growth and hence subsequent growth is relaxed.

Raman spectroscopy of the film showed that the c-Ge peak was slightly asymmetrical, with the high wave number side having a larger intensity than the low side. The peak value was the same as for Ge. The FWHM of the peak increased by approximately 18% over the Ge peak, and it was at a slightly lower intensity. Figure 5.28 shows a comparison of the Raman spectra collected from the Ge wafer, the top surface of the Ge-C film, and the bulk of the film. These data indicate then that the grain size and the crystal order of the germanium carbide film were slightly reduced compared to the Ge wafer.

5.5 Stacked $Ge_{1-x}C_x$ Layer Structures on Si Substrates

The next set of experiments involved the growth of stacked $Ge_{1-x}C_x$ layer structures on Si wafers. The purpose of these structures is to improve the grain size and crystal quality of Ge and Ge:C films that are grown on Si wafers.

5.5.1 $Ge_{1-x}C_x$ buffer layer

The first type of structure is a thin buffer layer that is grown on the Si wafer first, followed by a Ge film that is grown on top of the buffer layer. The idea behind this structure is that the buffer layer would compensate for the lattice mismatch between the Ge and Si.

The buffer layer's corresponding factorial experiment sample had a grain size of 5255 Å. a Raman FWHM of 7 cm^{-1}. and it had approximately 3 atomic percent C incorporated. The lattice constant a of this sample was 5.674 Å. although this is most likely the value for a relaxed film. The buffer was grown for 90 sec. giving it a thickness of 21 Å. This thickness was chosen because it is less than the critical thickness reported by Osten and co-workers. Hence. the buffer layer should not relax. The corresponding factorial experiment film had a grain size of 1893 Å and a Raman FWHM of 5.4 cm^{-1}. It had a lattice constant of 5.676 Å. It was grown to a 0.3 to 0.4 μm thickness on top of the buffer layer.
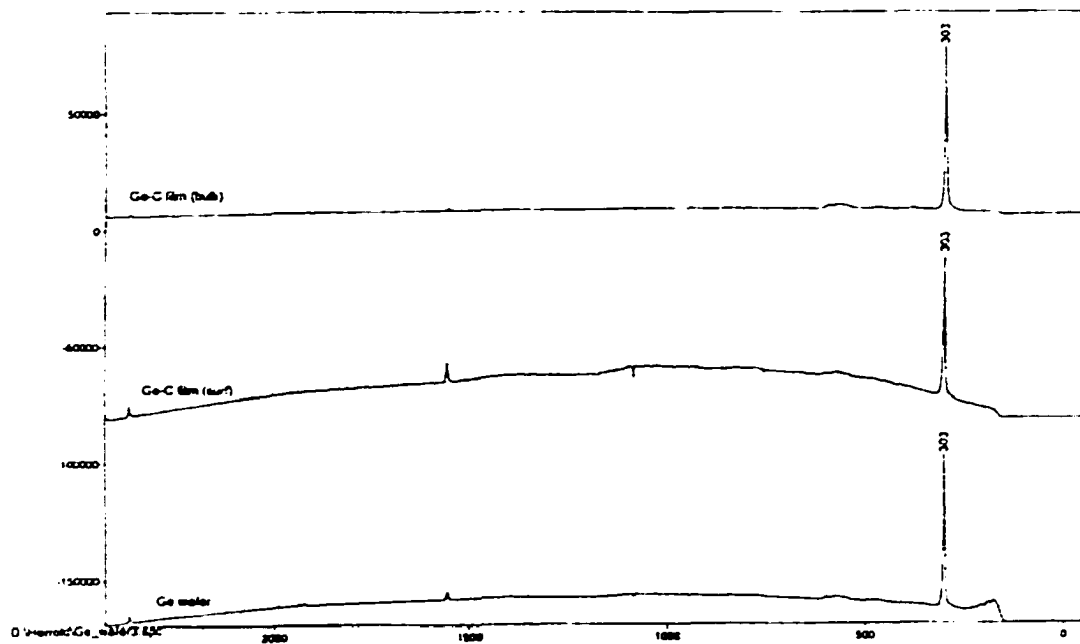
Figure 5.28: Raman spectra of Ge wafer, Ge-C film at the surface of the film, and the Ge-C film in the bulk of the film.

The grain size of the Ge film after it had been grown on the buffer layer was 2913 Å. Thus the grain size of the Ge film was improved by 54%. This strongly indicates that the strain of growing Ge on Si had been greatly reduced by the buffer layer. Raman measurements of the structure were made. and the FHWM value was determined to be 6 cm^{-1} although the FWHM had to be determined manually because the peak was too small to be profiled by the peak analysis software. This is an improvement in the FWHM value of approximately 14%. and this again indicates that the buffer layer improved the quality of the film.

5.5.2 Graded Ge$_{1-x}$C$_x$ buffer layer

A similar buffer layer to the previous structure was grown. with the difference being that the C content in the buffer layer was graded. The concentration near the Si/Ge:C interface had a high C concentration and this concentration was gradually lowered until there was no C at the Ge:C/Ge interface. It was expected that this structure would alleviate strain by reducing the lattice mismatch on both the Ge and Si sides. The parameters of this buffer layer were identical to the preceding buffer layer. The flow rate of methane was reduced to zero in ten equal steps as the film grew. To make the grading from the buffer to the Ge film easier. parameters that more closely matched the buffer layer were used for the Ge film. The corresponding factorial experiment Ge sample had a grain size of 662 Å. and a Raman FWHM of 5.1 cm^{-1}.

The grain size of the buffer layer sample was found to be 680 Å. The Raman peak was again too small to be profiled by the peak analysis software. but the FWHM was measured manually and determined to be 5 cm^{-1}. It was very surprising that this structure did very little to improve the quality of the film. It is unclear why this structure does not work better than the non-graded buffer layer.

5.5.3 Ge$_{1-x}$C$_x$ strained superlattice

The next type of structure that was grown was a strained superlattice structure. The first of these was used to improve the quality of a Ge film grown on a Si wafer. The initial layer grown on the wafer was a Ge:C layer whose corresponding factorial experiment sample had a grain size of 5255 Å. a Raman FWHM of 7 cm^{-1}. and it had approximately 3 atomic percent C content. The intent was to lattice match to the Si wafer as closely as possible. The

layer, and all subsequent layers of this type, was grown approximately 14 Å thick. The layer was kept thin so as to stay below the critical thickness for $Ge_{1-x}C_x$. The alternating layer was a Ge layer. The purpose of this layer was to relieve the strain caused by incorporating C into the Ge lattice. The corresponding factorial experiment sample had a grain size of 662 Å after correcting for Si broadening, and a Raman FWHM of 5.1 cm^{-1}. The thickness of this layer was 29 Å. This is certainly thicker than the critical thickness for Ge, but it is was very difficult to grow much of a thinner layer with the deposition system used, especially with a pure Ge layer as its growth rate is much higher than that of $Ge_{1-x}C_x$. A total of twenty alternating layers were deposited and then the pure Ge film was continued until 0.4 µm total thickness was achieved.

This sample had a grain size of 839 Å, which was an improvement of 27% over the sample that did not have the superlattice structure. The improvement in grain size was not as good as the single germanium carbide buffer layer sample, which was described above. The reason this structure did not work as well as the buffer layer sample can probably be attributed to the increased complexity of the structure and to the number of interfaces, each of which had the potential to reduce the grain size if an interface of high quality was not grown. The sample had a Raman peak at 305 cm^{-1}, and a FWHM of 7.7 cm^{-1}. So the FWHM of the superlattice structure was worse than the FWHM of the original Ge film that did not have a superlattice. It is interesting to note that the FWHM of the final Ge layer in the superlattice is similar to the FWHM of the original $Ge_{1-x}C_x$ film that was deposited on the Si wafer. So it may be the case that the initial $Ge_{1-x}C_x$ film that was deposited had a FWHM of 7.7 cm^{-1}, and this initial $Ge_{1-x}C_x$ layer set the FWHM of all subsequent layers. This would seem reasonable, since the initial $Ge_{1-x}C_x$ layer served as a template for all of the following layers.

The second type of superlattice structure that was grown was used to improve the quality of a $Ge_{1-x}C_x$ film grown on a Si wafer. This structure had an initial layer that contained approximately 2 atomic percent carbon incorporation. The alternating layer was also a germanium carbide layer, but it only had approximately 0.5 atomic percent carbon concentration. So the first layer was deposited to reduce the stress of the lattice mismatch to the Si wafer, and the alternate layer was used to reduce the internal strain of the material caused by trying to incorporate a significant amount of C into the Ge lattice. There were 20

layers total in the structure. Each layer was roughly 25 Å. which is close to the critical thickness for germanium carbide. A thick layer was then deposited on top of these stacks. with a total thickness including the stacks of 0.31 μm.

It was found that the sample had a Raman FWHM of 4.9 cm^{-1}. where as the sample that was grown with no superlattice had a FWHM of 8.9 cm^{-1}. It is assumed that the strain relief provided by the stacked layer improved the crystal ordering of the thick layer. and this is why the stacked layer sample had a FWHM that was 45% smaller than the no superlattice sample. This is so because the strain tends to distort the lattice. pulling atoms off their correct lattice sites. and this tends to increase the FWHM. But reducing the strain through the superlattice approach then allows more of the atoms to stay on their lattice positions and hence. the FWHM value is smaller.

The grain size of the stacked layer sample had a grain size of 1091 Å. whereas the sample sans superlattice had a grain size of 667 Å. The increase in grain size of 38% is also attributed to strain relief. for the same reasons as those listed above.

5.6 Ge$_{1-x}$C$_x$ Diodes

Using the doped layers that were described in earlier sections. a simple p/n junction was fabricated. The device was grown on a n$^-$ Si wafer. which served as the back contact. An n$^-$ Ge$_{1-x}$C$_x$ layer was deposited first. to make an ohmic contact with the Si. The germanium carbide contained approximately 3 atomic percent C. had a Raman FWHM of 5.2 cm^{-1} and a grain size of 686 Å. The bandgap of the material was approximately 1 eV. An n Ge$_{1-x}$C$_x$ layer. followed by a p Ge$_{1-x}$C$_x$ layer was deposited next. The thickness on the n and p sides were approximately 0.2 μm. which is much longer than the junction depletion width at any bias. and much longer than the calculated diffusion lengths. Metal contacts were then made to the p layer. The first type of contact that was attempted was an evaporated circular Cr dot. 100 Å thick. on top of which was evaporated an Al bussbar contact. The reason behind this type of contact was that it was desired to measure the photocurrent of the diode. The above described contact was desirable because the Cr would allow light to pass through. and yet still be able to be somewhat conductive. at least good enough to carry current to the bussbar contact. The bussbar would then carry current to the probes. Unfortunately. it was

found that although this type of contact was tried many times, it always produced a shorted contact. It was found, however, that if just the Cr was evaporated and Ag paint was applied to a small area of the Cr, a suitable ohmic contact could be made through the Ag paint. It is believed then that the Al bussbar was shorting through the diode, probably due to Al spiking.

An I-V curve of the diode is shown in Figure 5.34. As can be seen, the I-V trace has the correct forward and reverse bias characteristics. The diode begins to conduct at a forward bias of approximately 0.5 V, which is appropriate for the bandgap of the material. The diode begins to breakdown at a reverse bias of approximately −1.3 V. It can be assumed that the breakdown mechanism seen is not punchthrough, because this is a very long diode with balanced doping on either side of the junction. It is also unlikely that the mechanism is Zener breakdown, because it occurs at relatively low reverse bias. The assumed breakdown method is then impact ionization breakdown. The impact ionization breakdown voltage, V_{BD}, can be calculated from the critical electrical field for impact ionization, E_{crit}, by,

$$V_{BD} = \frac{\varepsilon \bar{E}_{crit}^2}{2qN_d}$$

(5.1)

Evaluating equation 5.1 gives a breakdown voltage of 1.5 V, which is very close to the breakdown voltage of the device, -1.3 V.
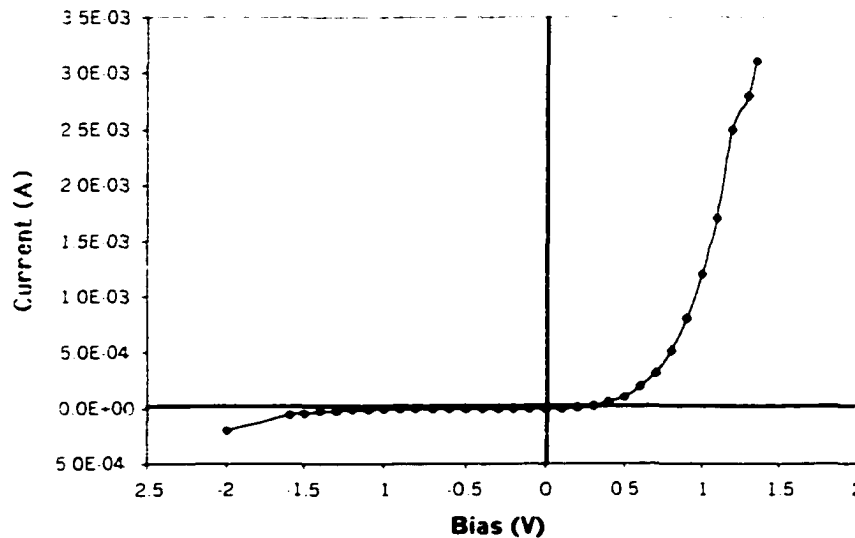
Figure 5.34: I-V trace of Ge-C diode.

The forward bias characteristics do not follow a standard ideal diode model, but instead a model that includes Shockley, Read, Hall (SRH) needed to be used. A semilog plot of current versus bias for the experimental diode, the ideal diode model and the SRH model are shown in Figure 5.35. As can be seen, the current never follows the ideal diode model. The SRH model uses a recombination time of $3 * 10^{-7}$ s, which was found by numerical iteration. The SRH model follows the data quite closely, and hence, it is believed that generation-recombination current heavily dominates the junction. This indicates that the junction is not a high quality junction. An experiment was also performed to determine the photocurrent of the diode. For this experiment, an I-V curve was generated in a light tight box, and then repeated with the diode illuminated by a 1X sun lamp. The comparison between the two curves is shown in Figure 5.36. As can be seen, the photocurrent is larger in the reverse bias region. This indicates that the diode is absorbing the light and collecting the associated carriers that are generated.
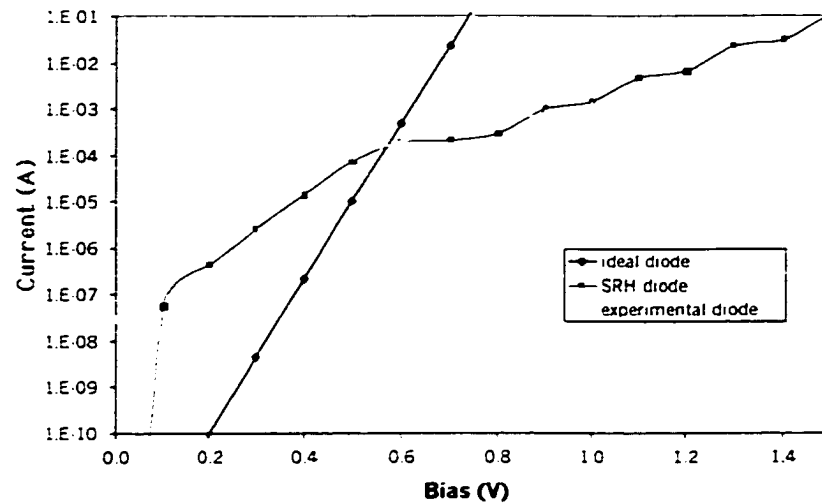
Figure 5.35: Comparison between data, ideal diode model and SRH diode model.
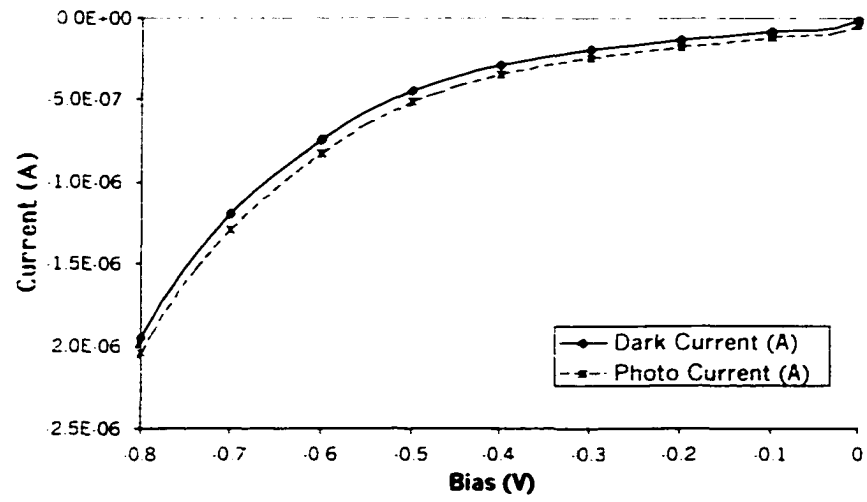
Figure 5.36: Comparison between light and dark current for Ge:C diode.

CHAPTER 6: CONCLUSIONS

Despite the interest in Group IV alloy materials for use in devices that operate in severe environments or that have device characteristics superior to pure Si microelectronics. the Ge:C system has been relatively ignored due to the difficulty in fabricating the material. Recently. however. a few research groups have had success in producing thin films of germanium carbide. This dissertation has focused on the fabrication of $Ge_{1-x}C_x$ materials by ECRPECVD processing. Intrinsic thin films of Ge and $Ge_{1-x}C_x$ have been grown on Si and Ge substrates. Doped films of $Ge_{1-x}C_x$ have also been grown on Si wafers. Finally. multilayer structures and diodes have been grown on Si.

The experiments involving the growth of Ge films on Si wafers revealed that a grain size up to 0.55 μm. and a Raman FWHM down to approximately 5 cm^{-1} could be achieved. It was found that lower powers and lower H_2 dilution was beneficial to increasing the grain size. To decrease the Raman FWHM. higher H_2 dilutions and higher pressures are needed. The mobility of the films was approximately 1200 cm^2/V•s. and there was very little dependence on grain size. When comparative films were grown on Ge wafers. the quality of the films significantly improved. which demonstrated the effects of strain between the lattice mismatched Ge and Si.

Next. $Ge_{1-x}C_x$ films were grown on Si wafers. A maximum of 4.8 atomic percent carbon could be substitutionally alloyed in the films. while still maintaining good crystal quality. This raised the bandgap up to a maximum value of 1 eV. and contracted the lattice by a maximal amount of 0.1 Å. A maximum grain size of 0.52 μm could be attained. at a C content of 3 atomic percent. It was surprising that the grain size was not larger than the best Ge on Si film. but it is believed that the presence of C strained the film. and this strain ultimately limited the grain size. Evidence of this strain was found in the Raman data. and the FWHM value could only be minimized to approximately 6 cm^{-1}. The mobility of the samples was roughly 70 cm^2/V•s. which is significantly less than that of the Ge samples. C is believed to serve as scattering sites. which limit the mobility. Representative $Ge_{1-x}C_x$ films were grown on Ge wafers. It was found that these films contained a significant amount of strain. indicating that the $Ge_{1-x}C_x$ films have a different lattice constant than the Ge wafers.

Multilayer Ge:C structures were also grown on the Si wafers. The first of these was a

thin $Ge_{1-x}C_x$ buffer layer on top of which a Ge film was grown. The buffer layer served to significantly reduce the strain and defects normally found in a Ge film grown on a Si wafer. This was evidenced by a 54% increase in grain size and a 14% decrease in Raman FWHM. A slight variation of this structure was to use a graded buffer layer. Quite surprisingly, grading the layer did not significantly improve the Ge film. Another type of multilayer structure that was grown was a Ge/Ge:C superlattice on top of which a Ge film was grown. The superlattice improved the grain size of the film by 27%, but the Raman FWHM value only increased slightly. The poorer performance of the superlattice compared to the buffer layer is attributed to the complexity of the superlattice and to the fact that the superlattice requires many high quality interfaces. Another superlattice was grown where alternating layers of high and low C content $Ge_{1-x}C_x$ layers were grown. A thicker Ge:C layer was then grown on top of the superlattice. The presence of the superlattice increased the grain size of the $Ge_{1-x}C_x$ layer by 38%, and dramatically decreased the Raman FWHM value by up to 45%. It is assumed that the superlattice helped to reduce the strain caused by the substitutional C. and this improved the grain size and Raman FWHM of the film.

The final experiment was to fabricate a simple diode structure in the Ge:C material system. Prior to the diode, doped films were made. It was found that a maximum n doping of 10^{20} cm^{-3}, and a maximum p doping of 3 * 10^{18} cm^{-3} could be achieved. The n type autodoping value was found to be 2 * 10^{18} cm^{-3}. Using these doped layers a diode was fabricated on a n$^-$ Si wafer, which served as the back contact. Cr and Ag paint were used for the top contact. It was found that any contact that used Al caused a short, and this is attributed to Al spiking into the $Ge_{1-x}C_x$ material. The I-V trace of the diode was found to have the correct rectification characteristics and the diode had a turn on voltage of approximately 0.5 V. The diode went into impact ionization breakdown at a reverse bias of approximately −1.5 V. Modeling the I-V curve with a Shockley, Read, Hall model determined the recombination-generation time of the diode to be 3 * 10^{-7} s. The diode was found to be dominated by Schockely, Read, Hall trapping, indicating that the junction was not of high quality.

In conclusion, ECRPECVD processing has been shown to be an effective means of producing crystalline $Ge_{1-x}C_x$ thin films on silicon substrates. This dissertation has determined how to the deposition parameters affect the material properties, and how to

control the parameters to produce films with a variety of desirable qualities. including large grain size. good crystal quality. and engineered band gaps and lattice constants. By doing so. the knowledge of the fundamental physical processes involved with the growth of $Ge_{1-x}C_x$ thin films has been expanded. In addition. new areas of research in multilayer $Ge_{1-x}C_x$ structures and diodes have been presented. In light of the results discussed in this dissertation. the use of $Ge_{1-x}C_x$ thin films as lattice matching layers for the purpose of fabricating high speed Ge devices on Si wafers. or the use of $Ge_{1-x}C_x$ devices in high efficiency optoelectronic applications warrants further research in this area. This dissertation has shown that despite the difficulty in fabricating $Ge_{1-x}C_x$ materials. this new material system has significant benefits that can be realized.

APPENDIX: ELECTRON MOTION IN A STATIC MAGNETIC FIELD

Free electrons in the plasma generation region spiral around the static magnetic field lines. due to the Lorentz force.

$$\vec{F} = q(\vec{v} \ x \ \vec{B})$$ (A-1)

If we assume that $\vec{B} = B_o \, \hat{a}_z$. this can be written as shown in Equation A-2.

$$m \frac{d^2x}{d^2t} \hat{a}_x + m \frac{d^2y}{d^2t} \hat{a}_y + m \frac{d^2z}{d^2t} \hat{a}_z = qB_o \left(v_y \, \hat{a}_x - v_x \, \hat{a}_y \right)$$ (A-2)

By equating components. we get the results shown in Equation A-3.

$$m \frac{d^2x}{d^2t} = qB_o v_y \qquad m \frac{d^2y}{d^2t} = -qB_o v_x \qquad m \frac{d^2z}{d^2t} = 0$$ (A-3)

Now by integrating with respect to t. we get Equation A-4.

$$\frac{dx}{dt} = \frac{qB_o y}{m} + C_1 \qquad \frac{dy}{dt} = -\frac{qB_o x}{m} + C_2 \qquad \frac{dz}{dt} = C_3$$ (A-4)

The result in Equation A-4 can be put back into Equation A-3 to get separated differential equations. For example. the equation for x is

$$\frac{d^2x}{dt^2} + \omega_o^2 x = x_o \omega_o^2$$ (A-5)

where $\omega_o = \frac{qB_o}{m}$ and $x_o = \frac{C_2}{m \omega_o}$. The solution to this equation is

$$x = x_o + R\cos\left(\omega_o t + \phi\right)$$ (A-6)

where R and φ are the constants of integration. By taking the derivative of Equation A-6 we get the x-component of the velocity.

$$v_x = \frac{dx}{dt} = -R\omega_0 \sin\left(\omega_0 t + \phi\right) \qquad \text{(A-7)}$$

This result can then be substituted back into Equation A-4 in order to get

$$y = y_0 - R\sin\left(\omega_0 t + \phi\right) \qquad \text{(A-8)}$$

and

$$v_y = \frac{dy}{dt} = -R\omega_0 \cos\left(\omega_0 t + \phi\right) \qquad \text{(A-9)}$$

where $y_0 = \dfrac{C_1}{m\,\omega_0}$. Now if we square and add Equations A-6 and A-8 we see that the motion of the electron in the plane perpendicular to the magnetic field is circular with radius R.

$$\left(x - x_0\right)^2 + \left(y - y_0\right)^2 = R^2 \qquad \text{(A-10)}$$

From Equations A-7 and A-9 we can solve for the radius.

$$R = \frac{\sqrt{v_x^2 + v_y^2}}{\omega_0} = \sqrt{v_x^2 + v_y^2}\left(\frac{m}{qB_0}\right) \qquad \text{(A-11)}$$

Since the velocity of the electron in the z-direction (parallel to the magnetic field) is constant, the electron spirals around the z-axis with a frequency of

$$\omega_0 = \frac{qB_0}{m} \qquad \text{(A-12)}$$

and a radius given by Equation A-11 above.

REFERENCES CITED

[1]   R.A. Soref. Proc. IEEE 81. (1687) 1993.

[2]   A.R. Powell. K Eberl. B. A. Ek. S. S. Iyer. Journ. Cryst. Growth. (127) 1993.

[3]   R. Davis. G Kelner. M Shur. W. Palmour. J Edmond. Proc. IEEE 79. (677) 1991.

[4]   J. Kolodzey. et. al.. Appl. Phys. Lett. 67 (13) 25 September 1995.

[5]   M. Krishnamurthy. J. Drucker. A. Challa.. J. Appl. Phys.. 78 (12) December 1995.

[6]   M. Krishnamurthy. and W. Weber. J. Appl. Phys.. 82. 3287 (1997).

[7]   W. Weber. B. Yang. M. Krishnamurthy. 73 (5) 3 August 1998.

[8]   H. Osten and J. Klatt. Appl. Phys. Lett.. 65 (5) 1 August 1994.

[9]   M. Copel. M Reuter. E. Kaxiras. and R. Tromp. Phys. Rev. Lett.. 63 (632) 1989.

[10] L. Hall. J. Electrochem. Soc.. 119. 11 (1972).

[11] E. Palange. L. Ragni. L. Gaspare. G. Capellini. and F. Evangelisti. J. Appl. Phys.. 83 (11) 1 June 1998.

[12] F. LeGoues. J. Tersoff. M. Reuter. M. Hammar. and R. Tromp. Appl. Phys. Lett.. 67 (16) 16 October 1995.

[13] M. Tod. J. Kouvetakis. D. Smith. Appl. Phys Lett.. 68 (17) 22 April 1996.

[14] D. Nesting. J. Kouvetakis. D. Smith. Appl. Phys Lett. 74 (7) 15 February 1999.

[15] M. Gazicki. H. Szymanowski. and J. Tyczkowski. J. Vac. Sci. Technol. A. 14 (5) October 1996.

[16] B. Orner and J. Kolodzey J. Appl. Phys.. 81 (10) 15 May 1997.

[17] A. A. Demkov and O. F. Sankey. Phys. Rev. B 48. (2207) 1993.

[18] L. Hall. J. Electrochem. Soc.. 119 (11) November 1972.

[19] J. A. Carlisle. T. Miller. and T. Chiang. Phys. Rev. B. 47 (7) 15 February 1993.

[21] S. Sivaram. Chemical Vapor Deposition: Thermal and Plasma Deposition of Electronic Materials, Van Nostrand Reinhold. New York. 1995.

[21] A. Sherman. Chemical Vapor Deposition for Microelectronics: Principles. Tecnology. and Applications. Noyes Publications. New York. 1987.

[22] H. Pierson. Handbook of Chemical Vapor Deposition. Park Ridge. 1992.

[23] S. DeBoer. Ph.D. Dissertation. Iowa State University. 1995.

[24] P. Atkins and J. Beran. General Chemistry. 2nd Ed.. W. H. Freeman and Company. New York. 1990.

[25] M. Kushner. J. Appl. Phys. 63. (2532) 1988.

[26] B. Deryagin. D. Fedosev. Growth of Diamond and Graphite From the Vapor Phase. IX. Nauka. Moscow. USSR (1977).

[27] S. DeBoer. Ph.D. Dissertation. Iowa State University. 1995.

[28] G. Selwyn. Optical Diagnostic Techniques for Plasma Processing. American Vacuum Society. 1993.

[29] R. Manukonda. R. Dillon. T. Furtak. JVST A. American Vacuum Society. 1995.

[30] R. Pearse and A. Gaydon. The Identification of Molecular Spectra. 4th Ed.. John Wiley & Sons. Inc.. New York. 1976.

[31] M. DeFreese. Master of Science Thesis. Iowa State University. 2000.

[32] K. Clay. S. Speakman. G. Amaratunga. S. Silva. J. Appl. Phys.. 79 (9). May 1. 1996.

[33] R. Pearse and A. Gaydon. The Identification of Molecular Spectra. 4th Ed.. John Wiley & Sons. Inc.. New York. 1976.

[34] R. and G. Amaratunga. App. Optics. 34 (34) 1 December 1995.

[35] D. Aspnes. Properties of Silicon. The Institution of Electrical Engineers. New York. 1988.

[36] R. Swanepoel. J. Phys. E: Sci. Instrum.. 1214 (16)1983.

[37] R. Swanepoel. J. Phys. E: Sci. Instrum.. 896 (17) 1984.

[38] J. Pankove. Optical Processes in Semiconductors. Dover. 1975.

[39] C. R. Brundle. C. A. Evans. S. Wilson. Encyclopedia of Materials Characterization. Butterworth-Heinemann. New York. 1992.

[40] M. Bermejo and M. Cardona. J. Non-Cryst. Solids. 32 (413) 1979.

[41] P. Fauchet and I. Campbell. "Raman Spectroscopy of Low-Dimensional Semiconductors" Critical Reviews in Solid State and Materials Sciences. Vol. 14. Supplement 1. 1988.

[42] C. R. Brundle. C. A. Evans. S. Wilson. Encyclopedia of Materials Characterization. Butterworth-Heinemann. New York. 1992.

[43] J. Moulder. Handbook of XPS. Perkin-Elmer. New York 1992.

[44] L. H. Schwartz and J. B. Cohen. Diffraction From Materials. Springer-Verlag. Berlin. 1987.

[45] D. Cullity. Elements of X-Ray Diffraction. Addison-Wesley. Reading. 1978.

[46] A. Segmüller. "Characterization of Thin Films by X-Ray Diffraction. Thin Films From Free Atoms and Particles. Academic Press. Orlando. 1985.

[47] R. Pierret. Advanced Semiconductor Fundamentals. Addison-Wesley. Reading. 1987.

[48] D. Schroder. Semiconductor Material and Device Characterization. John Wiley and Sons. New York. 1990.

[49] D. Montgomery. Design and Analysis of Experiments. 4th Ed.. John Wiley and Sons. New York. 1997.

[50] L. Stephens. Beginning Statistics. McGraw-Hill. New York. 1998.

[51] J. Heath. J. Shiang. A. Alivisatos. J. Chem. Phys.. 101 (2) 15 July 1994.

[52] W. Weber. B. Yang. M. Krishnamurthy. App. Phys. Lett.. 3 (5) 3 August 1998.

[53] R. Weast. Ed.. <u>CRC Handbook of Chemistry and Physics</u>. CRC Press. Boca Raton 1992.